FACULTY
OF MATHEMATICS
AND PHYSICS
Charles University

MASTER THESIS

Stáňa Tázlarů

Hall effects in non-magnetic systems: classical, quantum and fractional

Institute of Physics of Charles University

Supervisor of the master thesis: Dr. Karel Výborný
Study programme: Theoretical physics
Study branch: Theoretical physics

Prague 2023

I declare that I carried out this master thesis independently, and only with the cited sources, literature and other professional sources. It has not been used to obtain another or the same degree.

I understand that my work relates to the rights and obligations under the Act No. 121/2000 Sb., the Copyright Act, as amended, in particular the fact that the Charles University has the right to conclude a license agreement on the use of this work as a school work pursuant to Section 60 subsection 1 of the Copyright Act.

In .... date ....
Author's signature

I would like to thank Dr. Karel Výborný for his endless patience as he guided me through the vast and diverse landscape of Hall effect physics and my family, whose support was crucial for me to reach this milestone on my journey.

Title: Hall effects in non-magnetic systems: classical, quantum and fractional

Author: Stáňa Tázlarů

Institute: Institute of Physics of Charles University

Supervisor: Dr. Karel Výborný, Institute of Physics of the Czech Academy of Sciences

Abstract: The classical Hall effect in disordered alloys is studied within the coherent potential approximation, explicit formulas are applied to the model system of the square lattice with on-site disorder, and temperature dependence of the Hall coefficient is examined in the pure model.

An approach to describe the effect of quantizing magnetic fields is outlined (related to the integer quantum Hall effect in two-dimensional systems), and its application to a three-dimensional tight binding model of alkali metals is discussed.

Finally, within the context of the fractional quantum Hall effect with filling factor $\nu = 1/3$ are examined two specific problems, whose resolution is sought using a single mode approximation.

Keywords: Hall effects, Coherent potential approximation, Tight binding model, Single mode approximation

Contents

Introduction

It is well known that electric current in the presence of magnetic field perpendicular to that current leads to accumulation of carriers at the sides of the conductor giving rise to the transversal electric field. This mechanism, in traditional geometry depicted in the figure 1, describes the so-called ordinary Hall effect.

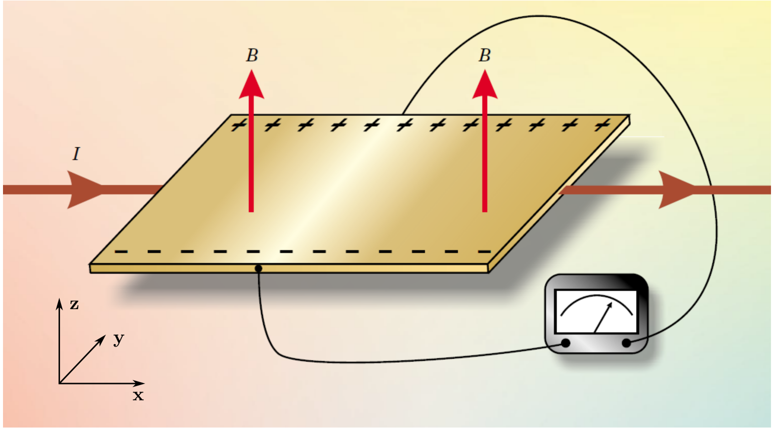

Figure 1: Ordinary HE geometry. Source [1].

Division of the induced electric field E_y by current density j_x and applied magnetic field B_z then defines Hall coefficient R_H, which provides measure of strength of response to the field or current, as it captures all relevant quantities. E.g. within the framework of the classical Drude theory one has for single charge carrier type a B field constant R_H dependent only on carrier density n and elementary charge e

$$R_H = -\frac{1}{en}, \tag{1}$$

or equivalently B field linear dependent transversal resistivity ρ_{xy}, as that is given merely by fraction of E_y field and current j_x. Note that here R_H is not dependent on dissipation and scattering, via Drude mean free time between collision τ, and is thus convenient for carrier density measurements.

Since the first observation of ordinary Hall effect by Edwin Hall in 1879 many more similar effects were discovered, leading to the present with a wide category of various Hall effects (HE). While the ordinary HE behavior may be well described within the framework of fully classical theory, these newer Hall effects often rely on additional material conditions, as, e.g. in the case of the anomalous HE, which can be observed in ferromagnetic conductors, or require more sophisticated theories for their description. Here being an integer or fractional HEs example as their description needs adoption of the fully quantum view.

For an extensive enumeration of the HEs, see e.g. [2], but in the following are presented basic descriptions of some more prominent of them.

Anomalous HE [3]: Present mainly in ferromagnetic materials and is observed as a steep increase in transversal resistivity proportional to magnetization in low magnetic fields until saturation is reached, at which point the dependency becomes that of ordinary HE. Anomalous HE may be orders of magnitude stronger than ordinary HE and crucially this increase in resistivity does not originate simply from aligning the magnetization in the direction of external field.

Spin HE [4]: Phenomenon based on relativistic spin-orbit interaction where, without the presence of the external magnetic field, electric current leads to the transversal spin-currents and accumulation of the spin of opposing orientation at the opposite sides of the samples, in which case it may be connected with anomalous HE due to the arising magnetization.

Planar HE: Known as transversal anisotropic magnetoresistance, an effect occuring in ferromagnetic metals when magnetisation is rotated in the $\mathbf{x}, \mathbf{y}$ plane [5]. The measured R_{xy} is then, unlike for other types of HE, not antisymmetric with respect to time inversion.

In the following is taken a closer look to a selection of HEs, which are purview of this work. All of them have in common that they are dependent on external B field and, in principle, do not lay further requirements on the material itself.

Classical Hall effect

In pursuit of determination of behavior of realistic materials, a semi-classical approach based on band structure of pure material is often employed. The case of calculation of R_H is the same in this regard as can be seen in, e.g., [6].

However, this approach has some obvious limitations. One of them is the inclusion of temperature dependence, which can be done in principle, but in practice brings its own difficulties. One goal of this work lies in answering the question of the importance of this contribution using the Sommerfeld expansion. Part of these results are presented in [7].

The second problem lies precisely in the fact that this approach is based on band structure, which brings difficulties with accounting for the effects of disorder. For example, limiting the scope of this problem only to substitutional disorder, one can employ a rigid band approximation [8], which consists of a simple shift of Fermi energy, while leaving the band structure of the used host material unchanged. One can easily see that such an approximation often leaves much to be desired even with small concentrations of impurities and renders it outright unusable in e.g. alloys.

Therefore, it may prove beneficial in such cases to abandon altogether the notion of band structure and approach the problem from a different angle. One such way provides a coherent potential approximation (CPA) which is analyzed and used for the calculation of R_H for the square lattice model.

Integer quantum Hall effect

As can be seen from the figure 3 the behavior of transversal and longitudinal resistivity is in a hight field much richer than predicted by classical theory. In particular, the emergence of plateaus in ρ_{xy} is purely quantum effect.

To see the origin of this behavior it is enough to consider one particle Hamiltonian (i.e. a factored Hamiltonian of one electron of non-interacting 2D electron gas).

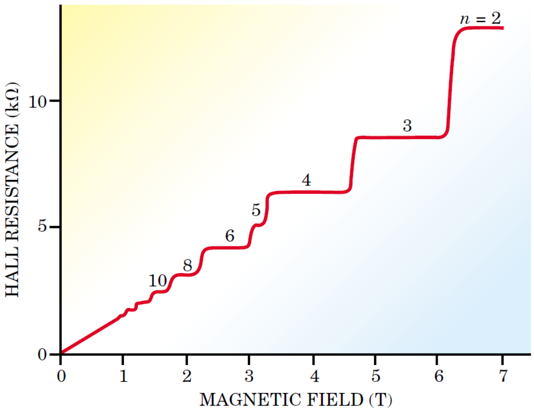

Figure 2: Integer quantum Hall effect for 2DEG. Source [1].

$$H = \frac{1}{2m} \left(\mathbf{p} - e\mathbf{A} \right)^2$$

Solving time independent Schrödinger equation then yields spectrum consisting of hugely degenerate Landau levels (LL) separated by gaps. It is then convenient to introduce so called filling factor ν which is a measure of how many LL are filled

$$\nu = \frac{hn}{eB},$$

with integer ν corresponding to the ν fully filled LLs. This discretization of energy levels is the foundation for quantization of transversal resistivity, as the conductivity becomes proportional to the number of fully filled LLs or equally resistivity to the inverse of that number.

In more realistic systems, the same principle to conductivity quantization remains, but the question of emergence of discrete highly degenerate LL is much harder to answer. Good measure to determine if one is in quantum regime, i.e. weather quantum effects can not be neglected provides magnetic length ℓ

$$\ell = \sqrt{\frac{\hbar}{eB}},$$

which is a magnetic quantum length scale. It is to be compared with the characteristic length scales of the material, i.e. lattice parameters for crystalline solids. From this it can be seen that in order to observe IQHE one has to prepare systems with artificial large length scale [9], or reach a sufficiently high field.

The study of the formation of LLs in square lattice tight binding model is performed using numerical exact diagonalization with magnetic field introduced via the Peierls substitution.

Fractional quantum Hall effect

The situation is more complicated still as plateau-like behavior can be observed even at some simple fraction of the filling factor ν. This has its origins at previously neglected electron-electron interaction, which leads to emergence of the energy gap, separating the ground state from the rest of the excitation spectrum.

While it is clear that now one has to operate fully within the many-body theory, there are still left many promising ways to tackle this problem.

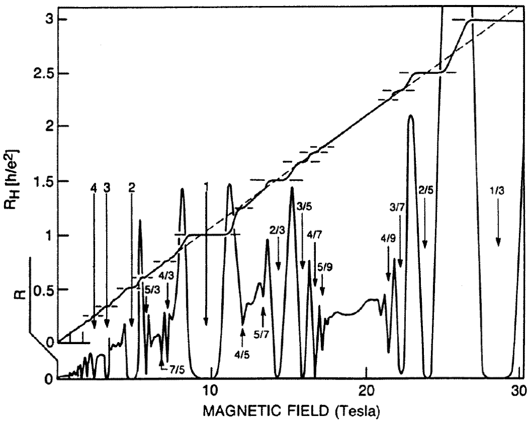

Figure 3: Transversal ρ_{xy} and longitudinal ρ_{xx} resistivity B field dependence for measurement in 2DEG system. Source [10].

Numerical methods [11]: The most direct approach is to employ an exact diagonalization or similar numerical method. The shortcoming of these methods is clear as the size of the matrices becomes with increasing number of electrons quickly unmanageable. Still, even in small but computable systems of ≈ 10 particles, one recovers a clear gap in the spectrum thus verifying the statement above. Also, with the difficulty of the measurement of the FQHE and mapping obtained results to analytical models, numerical methods provides necessary data to test various theories.

Composite fermions [12]: In the heart of this method lies the proposed flux attachment mechanism. Within this framework, one treats electrons with discrete number of magnetic flux quanta as a single particle, the composite fermion. These particles then have their own filling factor ν^* which can be mapped to the normal electron filling factor ν as

$$\nu^* = \frac{\nu}{2\nu + 1}.$$

This mapping is used as an explanation for the plateau-like behaviour as the emergence of the energy gap for integer ν is well described. [Shortcomings!]

Analytical approaches: Even besides composite fermion approach, there are available other frameworks, which seek to describe FQHE as which seek to describe FQHE as an incompressible liquid with fractionally charged excitations [13]. The main benefit of these approaches lies not only in their predictive power, but unlike numerical methods, they also bring light to the mechanism which leads to the FQHE.

As an example of the analytical approaches, a single mode approximation is further presented. It can be used to obtain the dispersion relation of the so-called magnetoroton branch and via that energy gap size. SMA results are compared with numerical data [14] and the discrepancy in the predicted and observed behavior of the magnetoroton branch in hight k is explained.

1. Classical Hall Effect

Semi-classical Boltzmann theory is usually employed for a description of the transport properties of crystalline materials. This is also the case in the first section of this chapter, Pure materials. Two classes of simple models are presented within the section: First, ideal electron gas leading to Sommerfeld theory of metals, and second, as a representative of crystalline materials, a cosine band models, i.e. depending on the dimensionality chain and square lattice models. Zero temperature Hall coefficient behaviour and then its temperature dependence are explored at the level of the magnetic field **B** linear response.

Need to describe physical systems with broken translational symmetry, such as alloys, motivates the second section, Substitutionally disordered materials. As the band structure based semi-classical description fails for disordered materials, the first part of the section is dedicated to introduction of necessary Green function formalism and to its general properties. In the later parts are on a relatively simple nearest neighbour tight binding substitutionally disordered chain model demonstrated and discussed strengths and weaknesses of various approximations for the central quantity, the so called self-energy, and especially coherent potential approximation is examined in more depth. The coherent potential approximation is then used to calculate the Hall coefficient for the square lattice model and its behaviour is examined.

Lastly Application for Hall sensors puts previous sections in a context of current Hall sensor development and specially focuses on particular requirements of ITER and DEMO fusion projects.

1.1 Pure materials

Albeit full current $\mathbf{j}$ response to driving forces as external electric $\mathbf{E}$ and magnetic $\mathbf{B}$ fields or gradients of temperature ∇T and chemical potential $\nabla\mu$ extends well beyond linear response, e.g. full non-linear and non-local second order electro-chemical driving force response as derived in [15] (equation 42, with σ denoting various conductivity tensors)

$$\mathbf{j} = \sigma\left(\mathbf{E} + \frac{1}{e}\nabla\mu\right) + \sigma^{E2}\mathbf{E}^2 + \frac{\sigma^{E2}}{e^2}\left(\nabla\mu\right)^2 + \sigma^{\nabla E}\nabla\mathbf{E} + \frac{\sigma^{\nabla E}}{e}\frac{\partial^2\mu}{\partial\mathbf{r}} + \dots,$$

for vast majority of transport phenomena is level of linear response sufficient for their description.

For the description of the classical Hall effect, it suffices to consider current response $\mathbf{j}$ linear in the electric field and bilinear in the electric and magnetic fields governed by the respective conductivity tensors σ.

$$j_i = \sigma_{ij}E_j + \sigma_{ijk}E_jB_k \tag{1.1}$$

Following the notation and derivation of Hall coefficient presented in [6], these tensors are within the Boltzmann theory given by a material band structure via its dispersion relation ε and associated group velocities $\mathbf{v}$ and effective mass tensor

M. The simplest case of a single band model is assumed here, so no band indices are present.

$$v_i = \frac{1}{\hbar}\frac{\partial \varepsilon}{\partial k_i}, \quad M^{-1}_{ij} = \frac{1}{\hbar^2}\frac{\partial^2 \varepsilon}{\partial k_i \partial k_j}$$

To obtain tensors $\sigma(\varepsilon)$ in the zero temperature limit one has to integrate **k** contributions over whole Fermi surface (FS)

$$\sigma(\varepsilon) = \int_{FS} \sigma(\mathbf{k}) dS,$$

where

$$\sigma_{ij}(\mathbf{k}) = e^2 \tau v_i v_j, \tag{1.2}$$

$$\sigma_{ijk}(\mathbf{k}) = -e^3 \tau^2 \epsilon_{k\alpha\beta} v_i v_\beta M^{-1}_{j\alpha}. \tag{1.3}$$

In $\sigma(\mathbf{k})$ expression is the positive elementary charge e, so the electron charge $q_e = -e$, ϵ represents the Levi-Civita tensor and τ denotes the relaxation time. Isotropy of τ is also assumed here. Althought τ is in general direction **k** dependent and disregarding anisotropy of τ may lead to huge errors with some materials, this approximation is still applicable for a very wide range of others [16].

Hall coefficients **R** are in low field linear response case given by

$$R_{ijk} = \frac{E^{ind}_j}{j^{app}_i B^{app}_k} = \sigma^{-1}_{\alpha j} \sigma_{\alpha\beta k} \sigma^{-1}_{i\beta},$$

and they are for anisotropic τ completely independent on relaxation time.

For a further manipulation and simplification of expressions present in this chapter is useful to introduce pure system FS integrals ϕ and ψ, which are for a system with diagonal effective mass tensor $M_{ij} = M_i \delta_{ij}$ of the form

$$\phi_{ij} = \int_{FS} v_i v_j dS, \quad \psi_{ij} = \int_{FS} v_i^2 M^{-1}_{jj} dS. \tag{1.4}$$

Conductivity tensor formulas can be then written as

$$\sigma_{ijk} = -e^3 \tau^2 \psi ij \epsilon_{kji}, \quad \sigma_{ij} = e^2 \tau \phi_{ij}. \tag{1.5}$$

Furthermore when conductivity is isotropic $\sigma_{ij} = \sigma_0 \delta_{ij}$, hall coefficients expression simplifies to

$$R_{ijk} = -\frac{\sigma_{jik}}{\sigma_0^2} = \frac{1}{e}\frac{\psi_{ji}}{\phi_{ii}^2}\epsilon_{kij}, \text{ and } R_H \equiv R_{123} = R_{xyz} = -\frac{1}{e}\frac{\psi_{yx}}{\phi_{xx}^2}, \tag{1.6}$$

where $R_H = R_{xyz}$ in particular denotes the Hall coefficient as defined in (1) and whose corresponding geometry is depicted in 1.

Ideal electron gas

Dispersion ε^{eg}, derived velocities and effective mass are in ideal electron gas (EG) case as follows

$$\varepsilon^{eg} = \frac{\hbar^2 \mathbf{k}^2}{2m}, \quad v_i = \frac{\hbar k_i}{m}, \quad M_{ij} = m\delta_{ij}.$$

Direct calculation of FS integrals (1.4) and R_H (1.6) employing isotropy with $k_i^2 = k^2/D$, D being dimension of the system, yields

$$\psi_{yx}^{eg} = \frac{1}{m}\phi_{xx}^{eg}, \quad R_H = -\frac{1}{em\phi_{xx}^{eg}}, \text{ where } \phi_{xx}^{eg} = \int \frac{d^D k}{(2\pi)^D}\frac{k}{mD}\delta\left(k - \frac{1}{\hbar}\sqrt{2m\varepsilon}\right) \tag{1.7}$$

Density of states of 2DEG and 3DEG, which are relevant for physics of Hall effect, are of the form

$$g_{2D}^{eg}(\varepsilon) = \frac{m}{2\pi\hbar^2}, \quad g_{3D}^{eg}(\varepsilon) = \frac{m^{3/2}}{2^{1/2}\pi^2\hbar^3}\varepsilon^{1/2}.$$

EG Hall coefficient expression is best written using particle density n

$$n(\varepsilon) = \int^{\varepsilon} g(\varepsilon')d\varepsilon', \tag{1.8}$$

as then in both 2DEG and 3DEG cases alike does the R_H^{eg} formula reproduce the classical Drude expression

$$R_H^{eg} = -\frac{1}{en}. \tag{1.9}$$

This result provides a simple test for more complicated crystalline systems to get a measure of the carrier behaviour. I.e. when $-n_c R_H$, with n_c being the carrier density, is $\approx 1/e$ one would expect more EG-like behaviour, whereas in regions where it differs significantly, the lattice effects play a major role.

Cosine band models

Cosine band models correspond to a tight binding nearest neighbour hopping models for 1D, 2D and 3D, chain, square lattice and cubic lattice respectively, with Hamiltonian of the form

$$\mathcal{H} = \varepsilon_0 \sum_i |i\rangle\langle i| + t \sum_{|i-j|=1} |i\rangle\langle j|, \tag{1.10}$$

where i and j are D dimensional multi-indices, ε_0 on-site energy and t a hopping parameter.

Such systems appear to be governed by two different energy variables ε_0 and t, but the time-independent Schrödinger equation is invariant with respect to energy scaling, which in (1.10) means simultaneous scaling of both ε_0 and t.

Since scaling them both simultaneously can not have any qualitative effect on static properties, with only change in trivial rescaling of $\mathcal{H}$ spectrum, it is convenient to introduce reduced energy units as

$$\tilde{a} = \frac{a}{t}, \quad \text{and specially} \quad \tilde{t} = 1, \tag{1.11}$$

which allows to eliminate hopping parameter t. In the following are all cosine band energy variables in their reduced form and the tilde is dropped.

The second symmetry of the time-independent Schrödinger equation is energy translation, rendering the remaining energy variable ε_0 trivial, also. This means that in truth there are no nontrivial system properties governed by any variable.

Lattice parameter a is taken for simplicity as $a = 1$ and thus $k_i \in \langle -\pi, \pi \rangle \ \forall\ i$. Corresponding dispersion relation is then

$$\varepsilon^{cb} = \varepsilon_0 - 2\sum_{i=1}^{D} \cos(k_i) \tag{1.12}$$

with band $\varepsilon \in \langle \varepsilon_0 - 2D, \varepsilon_0 + 2D \rangle$ and associated velocities and masses

$$v_i = -\frac{2}{\hbar}\sin(k_i), \quad M_{ii}^{-1} = -\frac{2}{\hbar^2}\cos(k_i), \quad M_{ij}^{-1} = -\frac{2}{\hbar^2}\left(\sin(k_i) + \sin(k_j)\right), i \neq j.$$

When it comes to DOS now, while the 1D chain g_{1D}^{cb} can be directly integrated, square lattice g_{2D}^{cb} results in a formula involving a complete elliptic integral of the first kind K and the cubic lattice g_{3D}^{cb} is more complicated still.

$$g_{1D}^{cb}(\varepsilon) = \frac{1}{\pi\sqrt{4 - (\varepsilon - \varepsilon_0)^2}}, \quad g_{2D}^{cb}(\varepsilon) = \frac{1}{2\pi^2} K\left[1 - \left(\frac{\varepsilon - \varepsilon_0}{4}\right)^2\right]$$

Fortunately K is easy to evaluate by means of arithmetic-geometric mean M

$$K(x) = \frac{\pi}{2M(1, \sqrt{1 - x^2})}$$

and g_{3D}^{cb} can be calculated using square lattice DOS [17] (Appendix E).

$$g_{3D}^{cb}(\varepsilon) = \frac{1}{\pi}\int_{\alpha_1}^{\alpha_2} \frac{du}{\sqrt{1 - u^2}} g_{2D}^{cb}(\varepsilon + 2u), \quad \text{with} \quad \begin{matrix} \alpha_2 = min(1, 2 - \varepsilon/2) \\ \alpha_1 = max(-1, -2 - \varepsilon/2) \end{matrix}$$

All presented cosine band DOS are normalised with one lattice point with one site per lattice cell so their corresponding particle densities $n \in \langle 0, 1 \rangle$. That is, n as defined by (1.8) with cosine band DOS g^{cb} are elementary cell electron densities.

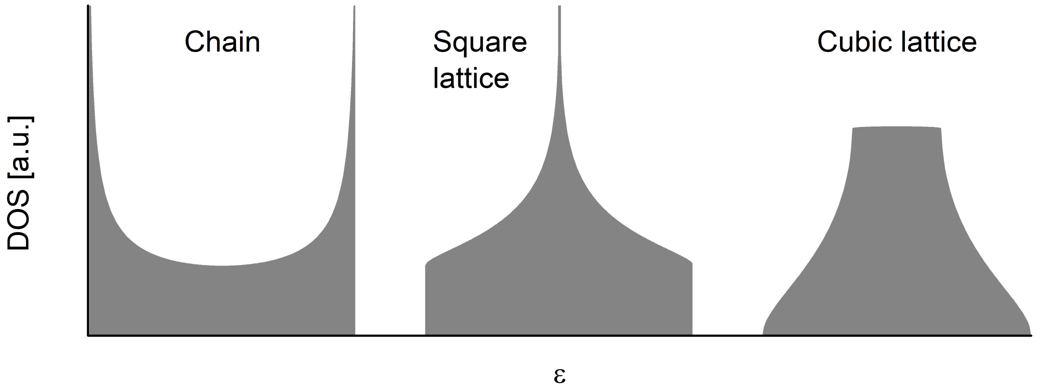

Figure 1.1: DOS of cosine band models. All shown with same bandwidth.

In 1.1 there are noticeable discontinuities and peaks, known as Van Hove singularities. These originate from extrema of the dispersion relation $\varepsilon(\mathbf{k})$. In 3D they generally lead to DOS derivative divergences, as seen in the cubic lattice case, while DOS of systems of lower dimensionality itself diverge at these points.

Also note that bounded nature of lattice bands allows to define hole density n_h in the same fashion as electron density $n_e \equiv n$ but counted from upper band edge, or more straightforwardly yet, in the present case as $n_h = 1 - n_e$.

Sign of the Hall coefficient R_H then determines majority carrier, which is better suited to description of such system, and carrier density n_c may then be defined using Heaviside function θ as

$$n_c = n_e\theta(-R_H) - n_h\theta(R_H). \tag{1.13}$$

R_H calculation for square lattice model

In the following is taken $\hbar = 1$, but note that all powers of $\hbar$ would cancel each other out in a full calculation of R_H. It can also be easily seen that $\phi_{xy} = 0$ and Hall coefficient is therefore given by the simplified expression (1.6).

FS integrals (1.4) for square lattice dispersion (1.12)

$$\begin{aligned}\phi_{xx} &= 4\int_{FS}\frac{d^2k}{(2\pi)^2}\sin(k_x)^2\delta(\varepsilon-\varepsilon(\mathbf{k})),\\ \psi_{yx} &= 8\int_{FS}\frac{d^2k}{(2\pi)^2}\sin(k_y)^2\cos(k_x)\delta(\varepsilon-\varepsilon(\mathbf{k}))\end{aligned}$$

are both invariant with respect to rotations by $\pi/4$ in $\{k_x, k_y\}$ plane. Contribution to the integral from each quadrant of the Brillouin zone is thus the same and it is possible to restrict the integrals only to one such quadrant where are present goniometric functions monotonous.

$$\begin{aligned}\phi_{xx} &= \frac{4}{\pi^2}\int_0^\pi\int_0^\pi dk_x dk_y \sin(k_x)^2\delta(\varepsilon-\varepsilon(\mathbf{k})),\\ \psi_{yx} &= \frac{8}{\pi^2}\int_0^\pi\int_0^\pi dk_x dk_y \sin(k_y)^2\cos(k_x)\delta(\varepsilon-\varepsilon(\mathbf{k})).\end{aligned}$$

This allows a change of integration variables

$$i = -\cos(k_i), \quad dk_i = \frac{di}{\sqrt{1-i^2}}, \quad \sin(k_i)dk_i = di, \quad \sin(k_i) = \sqrt{1-i^2},$$

where $i \in \{x, y\}$.

$$\begin{aligned}\phi_{xx} &= \frac{4}{\pi^2}\int_{-1}^1\int_{-1}^1 dxdy\sqrt{\frac{1-x^2}{1-y^2}}\delta(\varepsilon-\varepsilon_0-2(x+y))\\ \psi_{yx} &= -\frac{8}{\pi^2}\int_{-1}^1\int_{-1}^1 dxdyx\sqrt{\frac{1-y^2}{1-x^2}}\delta(\varepsilon-\varepsilon_0-2(x+y))\end{aligned}$$

Next introducing new variables $\{u, v\}$

$$u = x+y, \quad v = x-y, \quad x = \frac{u+v}{2}, \quad y = \frac{u-v}{2}, \quad dxdy = \frac{1}{2}dudv$$

with integration bounds

$$u \in \langle -2, 2 \rangle, \quad v \in \langle -2 + |u|, 2 - |u| \rangle$$

allows to eliminate one integration and resolve δ-function

$$\delta(\varepsilon - \varepsilon_0 - 2(x+y)) = \delta(\varepsilon - \varepsilon_0 - 2u) = \frac{1}{2}\delta\left(u - \frac{\varepsilon - \varepsilon_0}{2}\right),$$

yielding final integral expressions

$$\phi_{xx} = \frac{1}{\pi^2}\int_{-2+|u|}^{2-|u|} dv \sqrt{\frac{4-(u+v)^2}{4-(u-v)^2}}, \quad \psi_{yx} = -\frac{1}{\pi^2}\int_{-2+|u|}^{2-|u|} dv(u+v)\sqrt{\frac{1-(u-v)^2}{1-(u+v)^2}},$$

$$\text{where} \qquad u = (\varepsilon - \varepsilon_0)/2. \tag{1.14}$$

Although integrals in (1.14) have proper analytical solutions, their form is unwieldy and special attention must be paid during their evaluation as there are present terms as a fraction of two diverging quantities and the like.

A more straightforward approach is to calculate them numerically. Results of such calculation are shown in figure 1.2.

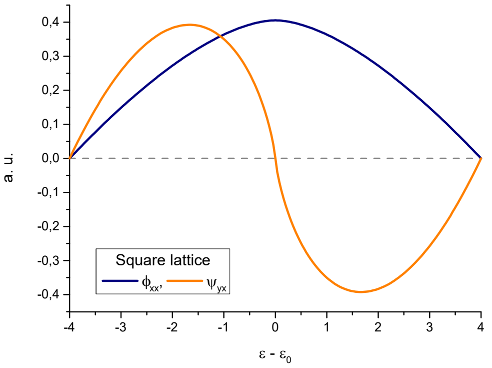

Figure 1.2: Square lattice (ε_{2D}^{cb}) FS integrals ϕ_{xx} and ψ_{yx} energy $(\varepsilon - \varepsilon_0) = 2u$ dependency.

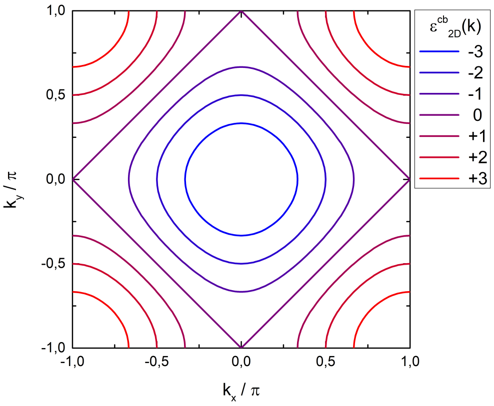

Figure 1.3: Square lattice (ε_{2D}^{cb}) FSs for various energies ε.

First, focusing solely on the ϕ_{xx} integral which is proportional to the conductivity tensor σ_{xx}: Graph 1.4 shows that σ_{xx}^{2Dcb} behaves near the band edges similarly to the EG conductivity σ_{xx}^{2Deg} (and also the classical Drude model) as it is proportional to the electron n_e or hole n_h density, whichever is smaller.

Alternatively, this can be summarised with the known R_H sign (figure 1.5 below) using carrier density n_c ($|n_c|$ for n_c defined in (1.13)) as $\sigma_{xx} \propto |n_c|$, for $|\varepsilon - \varepsilon_0| \lessapprox 2$.

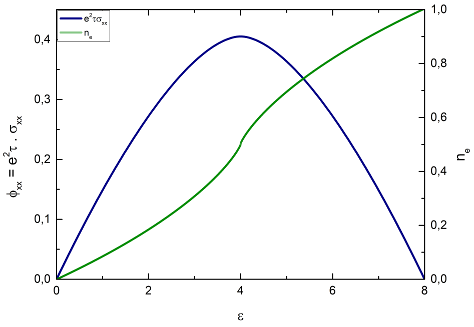

Figure 1.4: Square lattice (ε_{2D}^{cb}) conductivity σ_{xx} and electron density n_e energy dependence.

The sign of the Hall coefficient R_H is in (1.6) given by the sign of the FS integral ψ_{yx}, whose sign is in turn determined by the weighted integration of 'curvature' (effective mass tensor $\mathbf{M}$) over FS.

In the present case, the resulting sign is clear as for none ε the ψ_{yx} integration crosses an inflection equienergy line $\varepsilon = 0$ (1.3, or more detailed look in [18], fig. 2) where the character of the FS changes. It either stays within the convex region $\varepsilon < 0$, follows the inflection line, or is within the concave region $\varepsilon > 0$.

As can be expected due to the shape of the band structure, the majority carriers are for $\varepsilon < \varepsilon_0 = 0$ electrons and for $\varepsilon > \varepsilon_0$ holes.

Figure 1.5 contains the results of the calculation of R_H. Since Hall coefficient is divergent when approaching band edges where the carrier density vanishes $n_c \to 0$ one has to be careful when evaluating the band edge value of $-n_c R_H$. Here it was treated as a limit and resolved by applying the L'Hospital rule with $n_c' = \pm g_{2D}^{cb}$, and instead of derivatives of full analytical FS integrals ϕ and ψ derivatives of their interpolation functions were used instead. Yielding

$$-n_c R_H^{2Dcb} \to 1, \text{ as } \varepsilon \to \text{ band edge.} \tag{1.15}$$

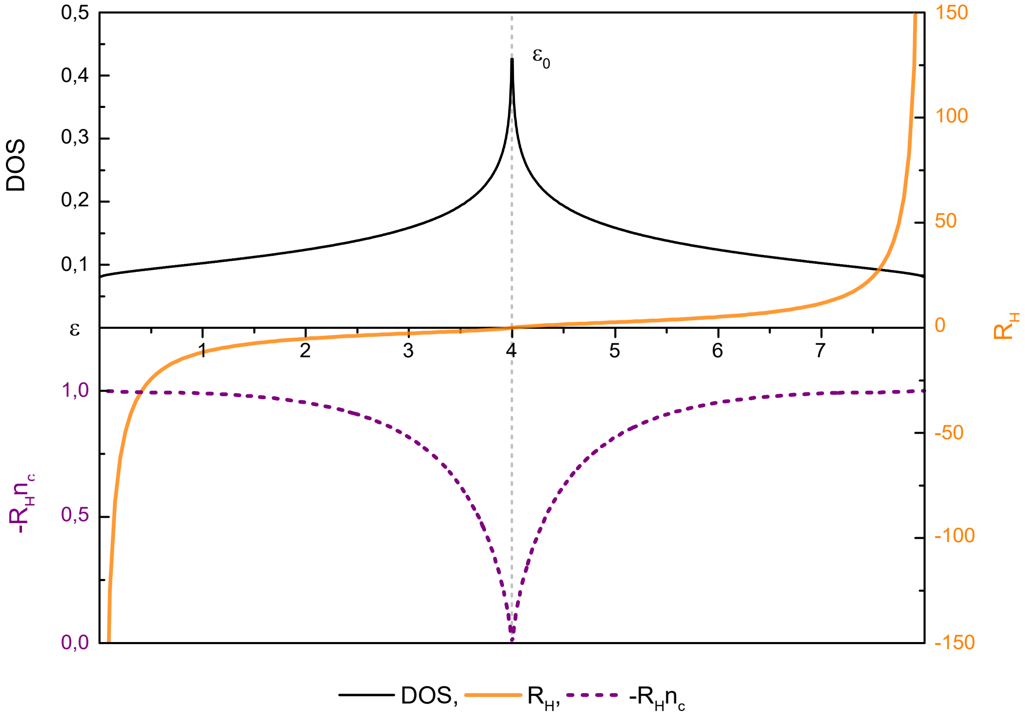

Figure 1.5: Square lattice (ε_{2D}^{cb}) R_H and $-n_c R_H$ energy ε dependence.

Square lattice conductivity and the Hall coefficient exhibit symmetry with respect to electron-hole inversion, or alternatively R_H^{2Dcb} is odd and σ_{xx}^{2Dcb} even with respect to ε_0. Their behaviour near band edges mirrors an ideal electron gas, which is to be expected as Taylor expansion of ε_{2D}^{cb} in the lowest order results in parabolic dispersion. On the other hand, the most prominent deviation from this behaviour is in the vicinity of Van Hove singularity at ε_0, where DOS diverges and R_H crosses zero.

1.1.1 Temperature dependence

Inclusion of temperature in conductivity σ calculation is relatively straightforward [6] [19] done via statistical averaging of zero temperature conductivity tensors $\sigma(\varepsilon)$ (1.2) and (1.3)

$$\sigma(T) = \int d\varepsilon \sigma(\varepsilon) \left[-\frac{\partial f_\mu(\varepsilon; T)}{\partial \varepsilon} \right], \quad f_\mu(\varepsilon; T) = \frac{1}{e^{(\varepsilon-\mu)/k_B T} + 1}, \tag{1.16}$$

with f_μ denoting Fermi-Dirac distribution for given chemical potential $\mu(T)$. Zero temperature limit yields $\mu(0) = \varepsilon_F$

$$f_\mu(T) \to \theta(\varepsilon_F - \varepsilon) \quad \text{and} \quad -\frac{\partial f_\mu(T)}{\partial \varepsilon} \to \delta(\varepsilon_F - \varepsilon) \quad \text{as} \quad T \to 0, \tag{1.17}$$

and (1.16) thus reproduces the previous $\sigma(\varepsilon)$ relations.

Instead of temperature T, it may be more convenient to introduce an inverse 'temperature' $\beta = 1/k_B T$ a measure of thermal energy with dimension of the inverse energy. Of special interest is then ratio of thermal and Fermi energies $1/\beta\varepsilon_F$ as a ratio of corresponding energy scales.

Because for most of a crystalline solid matter in standard conditions (e.g. room temperature) is [20] ε_F of order of unity in electronvolts, while $\beta \approx 0.01 \ eV$

$$\frac{1}{\beta\varepsilon_F} \ll 1, \tag{1.18}$$

it is natural to expect that inclusion of temperature within Boltzmann theory would have assuming no phase transitions only a slight effect on conductivity and Hall effect. The following part is dedicated to answering the question of how exactly does non-zero temperature manifests in R_H evaluation.

Sommerfeld expansion and electron gas

Sommerfeld expansion is a well-known low temperature expansion in the powers of the energy ratio $1/\beta\varepsilon_F$ of integrals of the type $\int \varphi(\varepsilon) f_\mu(\varepsilon) d\varepsilon$, with $\varphi(\varepsilon)$ at most polynomially diverging with $\varepsilon \to \infty$ and vanishing for $\varepsilon \to -\infty$. Its full derivation is presented in e.g. [20]. First order expansions

$$\int \varphi(\varepsilon) f_\mu(\varepsilon) d\varepsilon = \int_{-\infty}^{\mu} \varphi(\varepsilon) d\varepsilon + \frac{\pi^2}{6\beta^2} \varphi'(\mu) + O\left(\frac{1}{\beta\mu}\right)^4 \tag{1.19}$$

first term can recognized as a zero temperature contribution (recall (1.17)) and second term the first temperature dependent correction.

To apply this expansion to the EG conductivity one has to first rewrite $\sigma(\beta)$ expression to the required integral form.

$$\sigma(\beta) = \int \sigma(\varepsilon) \left[-\frac{\partial f_\mu(\varepsilon)}{\partial \varepsilon} \right] d\varepsilon \overset{p.p.}{=} [\sigma(\varepsilon) f_\mu(\varepsilon)]_{-\infty}^{\infty} + \int \frac{\partial \sigma(\varepsilon)}{\partial \varepsilon} f_\mu(\varepsilon) d\varepsilon$$

Since $\sigma(\varepsilon) \propto \varepsilon^{D/2}$ and is bounded from below, first term on the right hand side is zero. Then using (1.19)

$$\sigma(\beta) = \int \frac{\partial \sigma(\varepsilon)}{\partial \varepsilon} f_\mu(\varepsilon) d\varepsilon = \sigma(\varepsilon)\Big|_{\varepsilon=\mu} + \frac{\pi^2}{6\beta^2} \frac{d^2\sigma(\varepsilon)}{d\varepsilon^2}\Big|_{\varepsilon=\mu} + O\left(\frac{1}{\beta\mu}\right)^4. \tag{1.20}$$

To obtain the correction, one has to account for the temperature dependence of the chemical potential μ, which is given by the implicit integral equation corresponding to particle conservation. For particle density n has to hold

$$n = \int g(\varepsilon) f_\mu(\varepsilon) d\varepsilon, \tag{1.21}$$

which can be in most cases once more treated by Sommerfeld expansion to the same order of $1/\beta\mu$.

2DEG proves to be atypical in this regard. On one hand simple form of its DOS $g^{eg}_{2D}(\varepsilon) = g^{eg}_{2D}\theta(\varepsilon)$ allows to fully integrate (1.21) and obtain closed form expression for chemical potential

$$\mu^{eg}_{2D}(\beta) = \frac{1}{\beta} ln\left(e^{\beta\varepsilon_F} - 1\right), \tag{1.22}$$

but on the other hand this expression can not be expanded in β as it is not an analytical function in $T = 0$ or $\beta = \infty$.

3DEG case is straightforward in comparison. (1.21) expansion yields

$$\mu^{eg}_{3D}(\beta) \approx \varepsilon_F \left(1 - \frac{\pi^2}{12}\left(\frac{1}{\beta\varepsilon_F}\right)^2 + O\left(\frac{1}{\beta\varepsilon_F}\right)^4\right).$$

Plugging it into $\sigma(\beta)$ expansion (1.20) and conductivity tensors in turn in R_H expression returns

$$R^{3Deg}_H \approx -\frac{1}{ne}\left(1 + O\left(\frac{k_B T}{\varepsilon_F}\right)^4\right),$$

so first nontrivial term in expansion vanishes and corrections for zero temperature R^{3Deg}_H are at standard conditions $1/\beta\varepsilon_F \approx 0.01$ at least of order $\approx 10^{-8}$ or smaller.

This result was presented in [7] as a first estimate and consequently as an explanation of the relative Hall coefficient temperature independence of a chromium and, in general, all metal-based Hall sensors. More about this in Application for Hall sensors.

2DEG R_H temperature dependence

Zero temperature 2DEG Hall coefficient (1.7) is given solely by mass m charge e and FS integral ϕ_{xx}. Inclusion of temperature dependence does lead to change

$$\phi^{2Deg}_{xx} \to \int \left[-\frac{\partial f_\mu(T;\mu)}{\partial\varepsilon}\right] \phi^{2Deg}_{xx}(\varepsilon) d\varepsilon \propto \int \left[\frac{\beta e^{\beta\varepsilon}}{(e^{\beta(\varepsilon-\mu)} + 1)^2}\right] \varepsilon d\varepsilon.$$

This integral may be solved, e.g. using substitution $\tilde{\varepsilon} = e^{\beta\varepsilon}$, and using full expression for chemical potential (1.22) then leads to

$$\int_0^\infty \ldots d\varepsilon\Big|_{\mu=\mu^{eg}_{2D}} = \frac{1}{\beta} ln(e^{\beta\mu} + 1)\Big|_{\mu=\mu^{eg}_{2D}} = \varepsilon_F.$$

Therefore, thermal averaging of ϕ^{2Deg}_{xx} gives the same contribution as its zero temperature variant and 2DEGs Hall coefficient R^{2Deg}_H as well as conductivity σ^{2Deg} are in Boltzmann theory as presented here completely temperature independent.

Numerical analysis of square lattice case

Square lattice is chosen as the simplest lattice case to gain a measure of the effects of temperature on R_H in periodic systems. Despite their relative simplicity, the unwieldy forms of the FS integrals ϕ_{xx}^{2Dcb} and ψ_{yx}^{2Dcb} (1.14) and their thermal averages do not lend themselves to any straightforward general mathematical analysis.

This problem is thus approached from a numerical angle. For a set of different densities n and for various values of $k_BT = 1/\beta$ are in two step process calculated their Hall coefficients R_H^{2Dcb}. First, the chemical potential μ_{2D}^{cb} is obtained using condition (1.21) by the interval halving procedure. In the second step are for given μ and β evaluated thermal averages of FS integrals ϕ_{xx}^{2Dcb}, ψ_{yx}^{2Dcb}. Since they are continuous, smooth and slowly varying (as seen in 1.2) an interpolation functions of dense datasets $\{\varepsilon, \phi_{xx}(\varepsilon)\}$ and $\{\varepsilon, \psi_{yx}(\varepsilon)\}$ were used in this step instead.

The results of these calculations are shown in graph 1.6 in the form of a temperature correction over the absolute value of $R_{H0} \equiv R_H|_{T=0}$, $\Delta R_H(\beta) = R_H(\beta) - R_{H0}$. Results for $n = 0.5$ are excluded as both correction and R_{H0} are within the machine precision equal to zero.

Due to the energy translational and scaling invariance of the cosine band models the standard condition assumption (1.18) requires special attention. Since ε_F may be in isolation in the present model chosen completely arbitrarily, it is assumed that $\varepsilon_F \lessapprox 10$ eV and $1/\beta\varepsilon_F \approx 0.01$ in accordance with many real materials at room temperature. Thus, the condition (1.18) would roughly translate to the k_BT range of $\lessapprox$ 0.1 eV. Therefore, in the following are 'standard conditions' understood as $k_BT \lessapprox 0.1$ (a.u.).

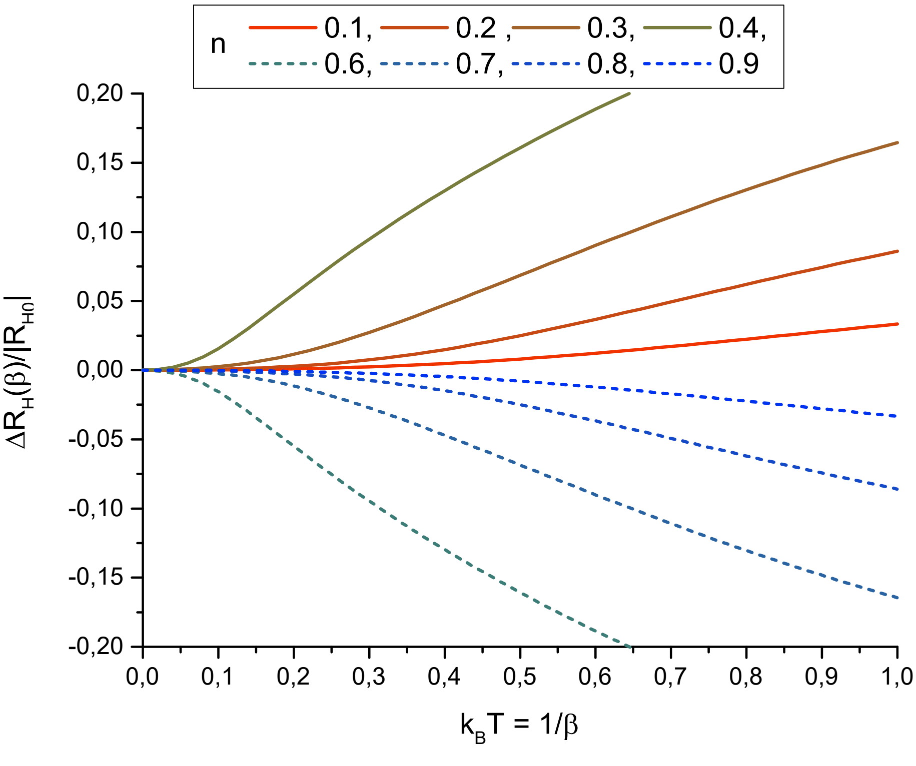

Figure 1.6: Square lattice (ε_{2D}^{cb}) $\Delta R_H(\beta)/|R_{H0}|$ temperature dependence for various densities n.

The first thing to note is that increasing temperature leads to a decrease in the absolute value of Hall coefficient in the whole band, as when are majority carriers electrons $R_H < 0$ and sign of $\Delta R_H(\beta)$ is positive and vice versa for holes.

As expected, graph 1.6 also explicitly shows preservation of the electron-hole inversion symmetry of R_H (i.e. R_H odd with respect to $n \to (1-n)$, first seen in zero temperature R_{H0}^{2Dcb}, figure 1.5) in thermal averaging (1.16).

The effect of thermal averaging is most prominent near the middle of the band, where R_H crosses zero, while lower carrier densities seem to be affected only slightly. This behaviour is in accordance with the expansion of the full dispersion ε^{cb}, which in the lowest order takes the parabolic EG form and in the same vein, the EG limit at the band edge in 1.8, (1.15). Since 2DEG Hall coefficient was proved to be completely temperature independent, so should be the band edge limit of square lattice.

The behaviour of the chemical potential $\mu_{2D}^{cb}(\beta)$ is less intuitive. At first glance, one may expect a shift in μ to be more pronounced near band edges as it has to compensate for asymmetric cut-off of the Fermi-Dirac distribution f_μ tails due to the bounded band structure. But graph 1.7 shows that the region in the vicinity of Van Hove singularity is affected more at first, until high enough temperature is reached, when it is finally overtaken by lower carrier density regions.

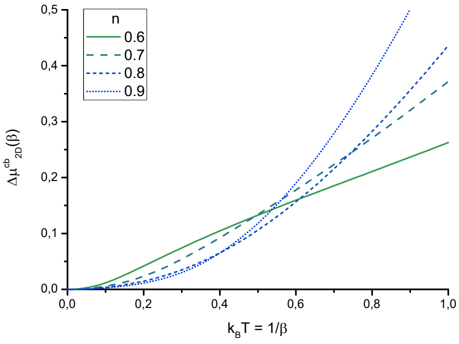

Figure 1.7: Square lattice chemical potential μ_{2D}^{cb} temperature dependence.

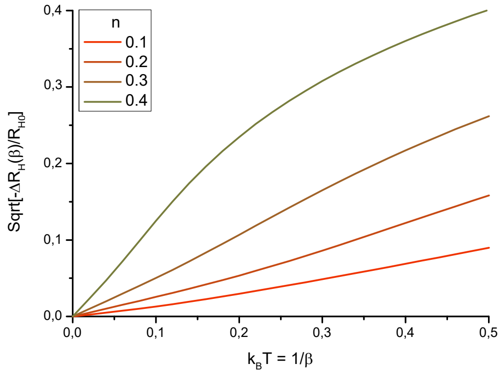

Figure 1.8: Square lattice $\sqrt{\Delta R_H / R_{H0}}$ temperature dependence.

It is clear from graph 1.8 that in standard conditions the temperature dependence of Hall coefficient is quadratic. This is to be expected in general for temperature averages of physical quantities of fermion systems, as the coefficients of the Sommerfeld expansion (1.19) with odd powers of β are due to the symmetry of $\partial_\varepsilon f_\mu$ zero.

This result is thus interesting only in that it differs from EG behaviour. While 3DEG and 2DEG may hint at only marginal dependence or complete temperature independence of R_H (at least as long as there are no phase transitions involved), this analysis of square lattice case paints a different picture.

In general, separating the temperature and density dependence, one has to expect

$$R_H(\beta) = R_{H0}\left[1 - \frac{\Delta R_H(\beta)}{R_{H0}}\right] \approx R_{H0}\left[1 - \frac{\eta(n)^2}{\beta^2}\right] \tag{1.23}$$

with $\eta(n)$ term encompassing possibly complicated density dependence of the first order correction for wide $1/\beta$ range.

Disregarding the region in the vicinity of the Van Hove singularity, where does R_H change sign, $\eta(n)$ is $\lessapprox 1$ and for $1/\beta \approx 0.1$ is the correction at least two orders of magnitude lower than zero temperature Hall coefficient R_{H0}.

1.2 Substitutionally disordered materials

Broken translational symmetry of pure crystalline solids presents main challenge in the description of disordered materials, preventing straightforward use of the band structure and notions based on it.

Still, there were such attempts, with one example being a rigid band approximation. It was used primarily for the description of metal alloys and assumes an unchanging band structure despite the substitution of a primary host element for a secondary. Only effect of alloying in this approximation is then a change of electron density n_{Alloy}

$$n_{Alloy} = (1-c)n_A + cn_B \tag{1.24}$$

for elements with different valence and subsequent shift in Fermi energy ε_F.

While there were some particular successes of this approach, it proved to be completely insufficient in vast majority of cases [8]. It seems clear that a more applicable theory has to take a step back from band structures and be built properly without the underlying assumption of translational symmetry.

A system study case used in the further section will be the simplest example of a substitutionally disordered material: a binary alloy.

Problem definition

Let substitutional binary alloy $\mathrm{A}_{(1-c)}\mathrm{B}_c$ be described analogously to pure cosine band tight-binding (1.10) by Hamiltonian $\mathcal{H}$ of the form

$$\mathcal{H} = \mathcal{W} + \mathcal{V}, \quad \mathcal{V} = \sum_i |i\rangle\, \varepsilon_i \,\langle i|\,, \quad \varepsilon_i = \langle i\,|\,\mathcal{V}\,|\,i\rangle = p(A)\varepsilon_A + p(B)\varepsilon_B, \tag{1.25}$$

where $\mathcal{W}$ is translationally invariant purely site off-diagonal part and $\mathcal{V}$ site diagonal disorder or impurity part. Furthermore, it is assumed that at each given site i there is a single localised state (orbital) $|i\rangle$ and overlap integral $\langle i\,|\,j\rangle = 0$ for $\forall i \neq j$.

The probability of a given site being occupied by an atom of type A, with on-site energy ε_A, is denoted as $p(A)$ and similarly for B. No preference in distribution of atoms (e.g. clustering of certain type) is assumed, with correlations arising solely from controlled concentration c of atoms of type B in the system. These correlations are negligible for large enough systems as they are falling off as N^{-1}, with N being the number of sites, and for each site is then independently $p(A) = (1-c)$ and $p(B) = c$.

Due to the stochastic nature of the system and its Hamiltonian (1.25) are not of interest behaviour and properties of its any particular realisation, but only corresponding configuration averages denoted as $\langle \ldots \rangle$.

Green's functions and effective medium

Properties of the system, such as the density of states g or the lifetime τ for decaying states, are easily accessible from Green's functions (GFs). Only key expressions directly connected with the problem at hand will be presented here with a more detailed discussion, e.g., in [21] or[8].

All GFs in the following are two-point (single particle) retarded GFs, which are for given Hamiltonian $\mathcal{H}$ defined as

$$G(z) = [z - \mathcal{H} + i\epsilon]^{-1} \quad \epsilon > 0, \tag{1.26}$$

with positive imaginary infinitesimal $i\epsilon$ suppressed in further expressions. Note the use of z for complex valued energy to differentiate it from real ε.

Objective of presented theory is to determine configuration averaged, so called effective medium (or shortened only to 'effective') GF $\overline{G}$

$$\langle G \rangle = \overline{G}. \tag{1.27}$$

This GF corresponds to effective medium Hamiltonian $\overline{\mathcal{H}}$

$$\overline{\mathcal{H}} = \mathcal{W} + \mathbf{\Sigma}, \tag{1.28}$$

which has restored translational symmetry due to the undertaken configuration averaging. The effective Hamiltonian of the medium $\overline{\mathcal{H}}$ consists of the original diagonal part $\mathcal{W}$ and a new self-energy operator $\mathbf{\Sigma}$ which describes a mean field arising from configuration averaged effects of original disorder potential $\mathcal{V}$.

Self-energy is thus defined by (1.27) and (1.28), or altogether as

$$\mathbf{\Sigma}(z) = z - \mathcal{W} - \overline{G}^{-1}(z), \qquad \mathbf{\Sigma}(z) = P^{-1}(z) - \overline{G}^{-1}(z),$$

where P stands for the so called unperturbed GF which is in this context related to Hamiltonian $\mathcal{H}_0 = \mathcal{W}$. P is also called propagator as opposed to locator g which involves different splitting of the full Hamiltonian $\mathcal{H}$ into an unperturbed one and a perturbation.

Self-energy operator $\mathbf{\Sigma}$ is therefore the only unknown, whose determination would be a key to the properties of the alloy via effective GF (1.27).

Analyticity and structure of Green's functions

Retarded GF owes its name to causal ordering, which translates into analyticity in the upper half-plane of complex energies. Its connection to the Schrödinger equation is also very clear in the energy representation, as its poles correspond to excitation energies of the system.

Note that due to the hermiticity of Hamiltonian (e.g. here (1.25)), retarded GF (1.26) has its poles located along real axis displaced by infinitesimal ϵ to complex lower half-plane. GF is in the case of finite dimensional Hilbert space with finite energy basis clearly meromorphic function $G : \mathbb{C} \to \mathbb{C}$ or analytical function $G : \mathbb{C} \to \mathbb{C}^*$, where $\mathbb{C}^*$ stands for extended complex numbers $\mathbb{C} \cup \{\infty\}$ (Riemann sphere), as all poles are necessarily isolated singularities.

This situation may change drastically on the infinite dimensional Hilbert space when poles of the GF accumulate forming a branch cut (formal description in e.g. [22]). In such case one has to perceive GF as a function $\mathbb{C} \to \mathbb{C}$ or $(\mathbb{C}^*)$ that is discontinuous along its branch cut, or more naturally as a meromorphic (analytical) function defined on a larger Riemann surface $\mathbf{R}$, $G : \mathbf{R} \to \mathbb{C}$ $(\mathbb{C}^*)$. Notably, GF in this view has no branch cut i.e. no poles associated with original real energies which formed it. Instead, one can find poles located in previously inaccessible sheets of larger Riemann surface with non-zero (non-infinisimal) imaginary part. The operator with which such GF is associated is no longer hermitian as no hermitian operator can have complex valued eigenvalues. This will be the case in the following with the self-energy operator $\mathbf{\Sigma}$ in effective GF (1.27).

Also note that if original GF $G : \mathbb{C} \to \mathbb{C}^*$ has no isolated poles and only a branch cut (cuts), then function $G : \mathbf{R} \to \mathbb{C}^*$ has necessarily poles on $\mathbf{R}$ as otherwise it would have to be constant or more precisely zero in current context of Hamiltonian $\mathbf{H}$ (1.25) due to its bounded spectrum which provides clear asymptotic behaviour

$$G(z) \to \frac{1}{z}, \quad \text{as} \quad z \to \infty. \tag{1.29}$$

One may also use a more general view of GF in the whole complex energy plane $G : \mathbf{R} \to \mathbb{C}$ to see the connection of time ordering in GFs and their energy representation. Since the Hamiltonian has to be bounded at lest from below there is no branch cut splitting energy plane entirely in two halves and one can continue retarded GF into lower half plane which corresponds to opposite time ordering of advanced GF. In this sense, there is then only one 'whole' GF G. Values of this GF on the real axis, which is of physical importance, are outside of the spectrum of the Hamiltonian determined uniquely as retarded and advanced GFs have the same limit $\epsilon \to 0$.

On the other hand, this whole GF becomes multivalued in the presence of poles or branch cut as a result of analytical continuation dependence on the half plane from which is pole or cut approached. Infinitesimal imaginary parts $\pm i\epsilon$ differentiating retarded and advanced GFs then ensue correct behaviour by explicitly selecting this complex half-plane from which is the real axis in the aforementioned limit of ϵ approached.

Derived properties and Bloch wave basis

Density of states at a given site g is obtained from the corresponding diagonal term of effective GF (1.27). E.g. taking site with index $i = 0$

$$g(\varepsilon) = -\frac{1}{\pi} Im[\overline{G}_{00}(\varepsilon)]. \tag{1.30}$$

The choice of the 00 component in the GF above is arbitrary due to translational invariance and this DOS relation holds for any diagonal component of $\overline{G}$.

For calculation of site diagonal terms of effective GF, as in (1.30) or in following self-consistent approximations for self-energy, one may use its translational invariance to rewrite it as a trace, which can then be evaluated on a suitable basis.

$$\overline{G}_{00}(z) = \frac{1}{N} Tr\left[\overline{G}(z)\right] = \frac{1}{N} \sum_{\mathbf{k}} \frac{1}{z - \varepsilon(\mathbf{k}) - \Sigma(z, \mathbf{k})} \tag{1.31}$$

Last expression here corresponds to a trace in Bloch wave basis, which diagonalizes (site) translationally invariant operators. One present example is $\varepsilon(\mathbf{k})$, which is the Fourier transform of $\mathcal{H}_0 = \mathcal{W}$. Similarly, translationally invariant $\mathbf{\Sigma}$ is also diagonalized in this basis and in general is also $\mathbf{k}$ dependent.

Specially when is approximate self-energy obtained from properties concerning configuration average at a single particular site immersed in effective medium, one has self-energy independent of $\mathbf{k}$. $\Sigma(z)$ is in such case for each given energy point z complex scalar. These approximations are owing to their nature known as single site approximations (SSAs), and they will be a focus of this whole section. Therefore, self-energy $\mathbf{k}$ independence is assumed in the following.

Imaginary part of the self-energy describes the scattering. In pure systems with hermitian Hamiltonians there are only states with infinite lifetimes, whereas inclusion of disorder leads to situation, where is the system best described with quasi-particles (corresponding to complex valued energies of poles) with finite lifetimes given by

$$\tau = \frac{\hbar}{2\Gamma} = \frac{\hbar}{-2Im[\Sigma]}. \tag{1.32}$$

Note that one cannot obtain this way $\mathbf{k}$ dependent lifetime τ as the single site self-energy does not contain any information on site correlations. Where does this dependence play a more vital role, one has to leave the limiting domain of the SSAs for more precise theories with intersite correlations.

Scalar retarded self-energy Σ has to have a negative imaginary part so that retarded GFs retain their analytical properties and here crucially so expressions for DOS (1.30) and lifetime τ (1.32) have only positive valued output.

Effective GFs for disordered lattices

Formulas for the effective GF site diagonal of two previously discussed cosine band models, the one dimensional chain and square lattice are shown below. In context of general Hamiltonian (1.25) it means

$$\mathcal{W} = \sum_{|i-j|=1} |i\rangle \langle j| , \tag{1.33}$$

with i, j simple indices in 1D, or multi-indexes in 2D case. Note the absence of the hopping parameter t due to the use of reduced energy units (1.11). System Hamiltonian (1.10) and corresponding dispersion relations (1.12) were shown in the previous section and for GF diagonal calculation is used relation (1.31).

$$\overline{G}_{00}^{1Dcb}(z) = \Big[(z - \varepsilon_0 - \Sigma)^2 - 4\Big]^{-1/2}. \tag{1.34}$$

Complex square root here is taken with branch cut along real axis, with its image being complex upper half-plane, so the site diagonal of effective GF retains its negative imaginary part.

This model is further used mainly for comparison of behaviour of examined approximations. The simple form of effective GF diagonal (1.34) allows one to solve self-energy equations of the examined approximations analytically and thus provides a good start for their analysis.

$$\overline{G}^{2Dcb}_{00}(z) = \frac{2}{\pi(z-\varepsilon_0-\Sigma)} K\left[\frac{4t}{z-\varepsilon_0-\Sigma}\right].$$

The end goal is to describe magnetic field-induced properties, exemplified by the Hall coefficient R_H, which cannot be realistically discussed in the 1D chain case. For this purpose, square lattice model will be employed.

Gershgorin circle theorem and DOS bound

While it may be hard to make broad statements about disordered materials, there exists a simple bound on system density of states provided by the Gershgorin circle theorem. It can be formulated as follows:

Let $\mathbf{M} \in \mathbb{C}^{n\times n}$ be a complex matrix and $D(a,r) \subset \mathbb{C}$ closed disc centred at $a \in \mathbb{C}$ with radius $r \in \mathbb{R}$. For spectrum $\sigma(\mathbf{M})$ of any such $\mathbf{M}$ is then

$$\sigma(\mathbf{M}) \subset \bigcup_{i=1}^{n} D(M_{ii}, R_i), \quad \text{where} \quad R_i = \sum_{i\neq j} |M_{ij}|.$$

This theorem takes a particularly simple form in the case of Hamiltonian $\mathcal{H}$ (1.25) in the site basis $\mathbf{H}$ as all radii $R_i = R\ \forall i$ due to translational invariance of $\mathbf{W}$, matrix site representation of $\mathcal{W}$. $\mathbf{H}$ has only two different diagonal values $\{\varepsilon_A, \varepsilon_B\}$ and its spectrum is real ($D \subset \mathbb{R}$).

$$\sigma(\mathbf{H}) \subset \bigcup_{i\in\{A,B\}} D(\varepsilon_i, R) \tag{1.35}$$

Specially in previously discussed cosine band models with $\mathcal{W}$ (1.33) is $R = 2$ for 1D chain and $R = 4$ for 2D lattice

$$\sigma(\mathbf{H}^{cd}_{1D}) \subset \langle \varepsilon_A - 2, \varepsilon_A + 2\rangle \cup \langle \varepsilon_B - 2, \varepsilon_B + 2\rangle,$$
$$\sigma(\mathbf{H}^{cd}_{2D}) \subset \langle \varepsilon_A - 4, \varepsilon_A + 4\rangle \cup \langle \varepsilon_B - 4, \varepsilon_B + 4\rangle.$$

It is reasonable to define scattering strength δ based on this bound

$$\delta = \frac{\varepsilon_B - \varepsilon_A}{R}, \tag{1.36}$$

as for δ sufficiently large ($|\delta| > 2$) there must necessarily be a region with zero density of states splitting one energy band into two separated sub-bands, the host band and impurity band.

Note that δ, or any related measure of A and B on-site energy difference $\varepsilon_B - \varepsilon_A$ is one of the only two nontrivial parameters, with concentration c, governing the cosine band models and it is its only energy parameter.

1.2.1 Single site approximations

Effective GF can be expanded into infinite series consisting of all combinations of terms of the type: free propagation (given by P), scattering (Σ), free propagation, and so on. This can be written in concise form as

$$\overline{G} = P + P\Sigma P + P\Sigma P\Sigma P + \ldots = P + P\Sigma\overline{G} = P + P\langle\mathcal{T}\rangle P. \tag{1.37}$$

The last equality shows another way to sum the series using $\mathcal{T}$, the so-called T-matrix, or transition matrix. T-matrix has its origin within the framework of scattering theory, where it separates the effects of the scattering potential in all scattering events from the free non-perturbed propagation. Both of these terms then contribute to a total transition amplitude in the scattering matrix, the S-matrix.

It plays the same role in the present case as it is the only nontrivial part of the GF in equation (1.37) encompassing effect of all scattering events in the dissordered system. Contrast this with self-energy, whose contribution to the GF is repeated in infinite series, and only its summation captures all the disorder and scattering fully.

Average T-matrix and self-energy are linked via

$$\langle \mathcal{T} \rangle = \Sigma \left(1 - P\Sigma\right)^{-1}, \quad \Sigma = \langle \mathcal{T} \rangle \left(1 + P \langle \mathcal{T} \rangle\right)^{-1}. \tag{1.38}$$

Taking a step back from self-energy, one can write the GF series for disorder potential $\mathcal{V}$

$$\overline{G} = P + P \langle \mathcal{V} \rangle P + P \langle \mathcal{V} P \mathcal{V} \rangle P + \ldots$$

and try to find approximation for the effective GF instead. The most straightforward way to do this would be (with the assumption of $|\mathcal{V}| \ll 1$) to truncate the series after finite number of terms, but closer examination shows that any such truncation covering any finite set of scattering processes would necessarily leave hand print of pure material structure in the effective GF.

For example, the first term (P) leaves pure band Van Hove singularities (recall 1.1) present in $\overline{G}$ and the case is similar with all higher terms, which would diverge at critical points too [8] making any such approximation insufficient. Divergences would also go against the underlying assumption of convergence of the series (1.37), which is in the first place enabling to perform present infinite summations.

This illustrates one of the benefits of the self-energy formalism, as any nonzero Σ leads to summation of infinite series of corresponding scattering processes in GF and, as will be seen bellow, allows to leave completely the domain of unperturbed GFs.

Full self-energy is given by

$$\Sigma = \langle \mathcal{V} + P\mathcal{V}P + P\mathcal{V}P\mathcal{V}P + \ldots \rangle = \langle \mathcal{V} \rangle + P \langle \mathcal{V} \rangle P + P \langle \mathcal{V} P \mathcal{V} \rangle P + \ldots \tag{1.39}$$

and its analytical approximations usually tend to either truncate this series resulting in e.g. Virtual crystal approximation (VCA) or Born approximation and its improved variant Self-consistent Born approximation (SCBA), or using suitable decoupling scheme to deal with hard to track correlations in averages $\langle \ldots \rangle$ allowing its summation as is the case in e.g. Average T-matrix approximation (ATA) or Coherent potential approximation (CPA). All of these approximation are SSAs as either due to the truncation or used decoupling scheme they result in expressions evaluated only on one site, neglecting any correlations with both near neighbours or any long range order.

Numerics and SSAs common behaviour

1D chain $\mathcal{H}_{1D}^{cb}$ model is used in this section for comparison of various SSAs and discussion of their strengths and shortcomings. Numerical DOS, calculated using negative eigenvalue counting algorithm, of chain of length 10^8 sites is provided as a reference to the analytical SSAs DOS.

Although these SSAs in many aspects differ as can be seen below, their common feature, the neglect of site configuration correlation, does lend them some common properties.

For one, note the correct (numerical) DOS fine structure with its many sharp peaks (1.9), while SSAs in general produce smooth DOS curves. This has its origin in short range order, which are the SSAs unable to capture, and whose effects are especially pronounced in systems of low dimensionality, where the configuration number (number of closest neighbours) is very low. Clusters of the same sites are then more prevalent, while each site in the higher dimensional systems is more likely to be surrounded by a mix of both site types, which more closely reflects the effective mean field of Σ.

On the other hand, the long range correlations have significant effect near band edges where DOS decays exponentially. This is a behaviour which SSAs consistently fail to reproduce [8], so extreme caution should be taken when they are used in these regions.

Virtual crystal approximation

The very simple but intuitive method to account for alloying is to disregard any scattering and assume that the alloy itself is again a pure crystal with only change present in a constant energy shift in the Hamiltonian with respect to the host pure material. It is natural to require correct pure material concentration limits ($c \to 0$ and $c \to 1$) and from this and the continuity in c for it to be a c interpolation scheme between these two pure crystals. Taking this dependence as a linear one has

$$\Sigma_{VCA} = \langle \mathcal{V} \rangle = (1-c)\varepsilon_A + c\varepsilon_B,$$

and virtual crystal Hamiltonian is simply

$$\mathcal{H}_{VCA} = \mathcal{W} + \Sigma_{VCA}.$$

Virtual crystal approximation (VCA) can in this regard be viewed as a spiritual successor of rigid band approximation at the self-energy level, with both having in common that they result only in a shift of Fermi energy with respect to a pure band.

Second and less arbitrary point of view is via self-energy series expression (1.39), with VCA self-energy being simply lowest order approximation

$$\Sigma_{VCA} = \langle \mathcal{V} \rangle .$$

Note that owing to even if trivial but still infinite series summation in GF related to VCA medium, there are no longer present any remnants of 'original' pure crystal structure, as discussed before.

While VCA by itself is too rough to be useful, as was the case with the RBA, virtual crystal medium is still appropriate as reference medium in the sense of

$$\mathcal{W} \quad \longrightarrow \quad \mathcal{W} + \Sigma_{VCA}, \qquad \mathcal{V} \quad \longrightarrow \quad \mathcal{V} - \Sigma_{VCA},$$

since for the disorder potential part is then

$$\langle i\,|\,\mathcal{V}-\Sigma_{VCA}\,|\,i\rangle=\begin{cases}\text{Site A: } p(A)=(1-c) \\ \qquad\qquad \varepsilon_A-(1-c)\varepsilon_A-c\varepsilon_B=c(\varepsilon_A-\varepsilon_B)=-c\Delta_\varepsilon \\ \text{Site B: } p(B)=c \\ \quad \varepsilon_B-(1-c)\varepsilon_A-c\varepsilon_B=(1-c)(\varepsilon_B-\varepsilon_A)=(1-c)\Delta_\varepsilon,\end{cases} \tag{1.40}$$

and by construction is configuration average of this new potential equal to zero.

Alternatively, using scattering strength δ (1.36) ($R=2$ for chain and $R=4$ in the case of square lattice), is

$$\langle i\,|\,\mathcal{V}-\Sigma_{VCA}\,|\,i\rangle=\begin{cases}-cR\delta & \text{Site A} \\ (1-c)R\delta & \text{Site B.}\end{cases}$$

Its first benefit is simplifications of expressions involved in the derivation of self-energy equations of various approximations, as e.g. first-order term in (1.39) vanishes in configurational average due to the $\langle\mathcal{V}\rangle=0$ property. Second and main benefit is a better and more symmetric separation of the 'unperturbed' $\mathcal{H}_0=\mathcal{W}$, which works now as a pure system concentration c interpolation scheme, from the impurity part $\mathcal{V}$, allowing to use the other SSAs themselves as an interpolation scheme and with greater accuracy [8].

More sophisticated approximations for self-energy

Both average T-matrix approximation (ATA) and self-consistent Born approximation (SCBA) belong to the class of still relatively simple but yet in some cases potentially sufficient approximations for self-energy.

Below follows their brief description and discussion of their properties. Figures 1.9 and 1.10 provide their comparison for fixed $\delta=1$ and various c ranging from $c=0.01$ up to a symmetric case $c=0.5$.

Both of these approximations are applicable in certain concentration ranges and both are in general more precise for systems of lower scattering strength δ, since for higher δ each has its own fatal failure.

An ideal approximation would have to combine strengths of these, providing a continuous and precise concentration interpolation scheme, and remedy the high δ problems encountered in ATA and SCBA, effectively spanning the whole parameter space. As will be seen below, CPA proves to be a very strong candidate for this approximation.

ATA self-energy

$$\Sigma_{ATA} = \frac{\langle t \rangle}{1 + \langle t \rangle P_0}$$

with configurational average of single site t-matrix $\langle t \rangle$

$$\langle t \rangle = (1-c)\frac{\varepsilon_A}{1 - P_0 \varepsilon_A} + c\frac{\varepsilon_B}{1 - P_0 \varepsilon_B}$$

is derived with an emphasis on consecutive scatterings on the same site, while neglecting configuration correlations for returning particles. Due to this, ATA is expected to correctly capture the behaviour of low c systems and to struggle with higher concentrations (up to $c = 0.5$, above symmetry in $c' = 1 - c$ and the switch of on-site energies ε owing to the VCA reference medium).

This is confirmed in graph A, with correct positioning of the impurity peak and host band structure. By B, problems such as somewhat sharper and shifted impurity DOS peak, or zero $Im[\Sigma_{ATA}]$ in part of the host band, are becoming visible. Graph C shows a complete failure of ATA to describe given system. The host and impurity bands are in ATA given much narrower bands, disregarding their edges completely and scattering is absent ($Im[\Sigma_{ATA}] = 0$) outside the emerging middle band located around Σ_{VCA}.

Examination of Σ_{ATA} equation reveals that this behaviour originates in a pole, which is present for all energies in the corresponding pure band of the VCA medium [8]. This is also the only source of non-zero self-energy imaginary part, leading to a limited energy range where scattering occurs. This also hints at a failure of ATA in higher δ, where, depending on the concentration, Σ_{VCA} can be positioned outside of both host and impurity bands. ATA will in such case incorrectly predict new band in the gap.

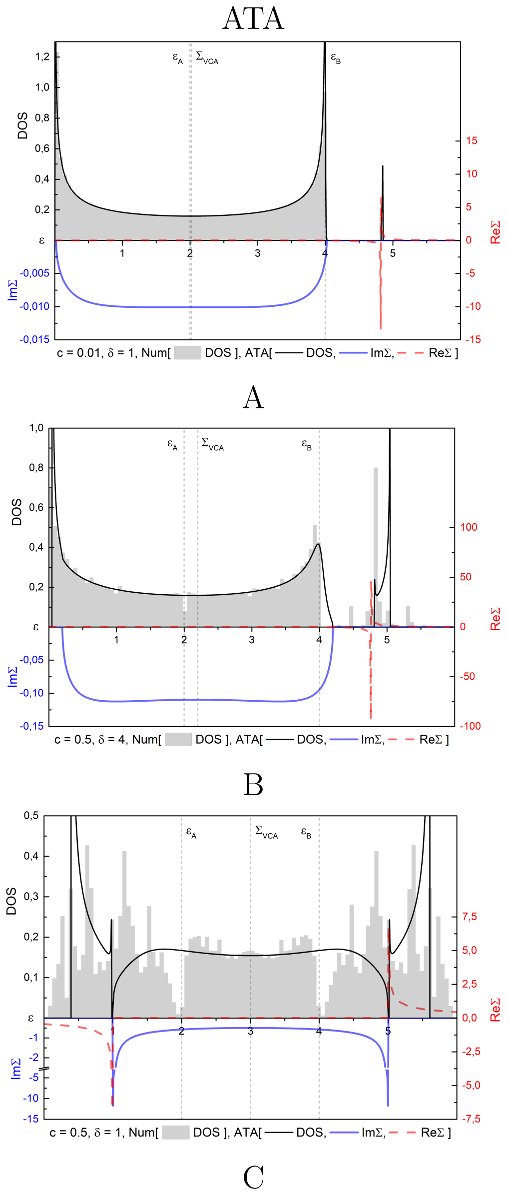

Figure 1.9: Chain $\left(\mathcal{H}^{cb}_{1D}\right)$ ATA self-energy Σ and DOS. Comparison with numerical calculation of DOS. Constant scattering strength $\delta = 1$ for increasing concentration c, A 0.01, B 0.1 and C 0.5.

SCBA given by

$$\Sigma_{SCBA} = c(1-c)\Delta_\varepsilon^2 \overline{G} \qquad (1.41)$$

is self-consistent (since $\overline{G}\,[\Sigma_{SCBA}]$) second order truncation of self-energy series (1.39). It may be hard to make predictions about its behaviour based on its origin, but examination of the SCBA self-energy equation itself reveals its most important properties.

For one, Σ_{SCBA} is proportional to the effective GF itself, with a pure real scaling parameter $c(1-c)\Delta_\varepsilon^2 \in \mathbb{R}$. Limit $\delta \to 0$ recovers pure material band structure pointing at its validity in a weak scattering regime. Taking imaginary part of self-energy equation leads to

$$\tau = \frac{\hbar\pi}{2c(1-c)\Delta_\varepsilon^2 g} \propto \frac{1}{g},$$

which guarantees scattering present in the whole energy range accompanying non-zero DOS. This relation is often used more generally as an initial rough estimate of the life-time τ (1.32).

Less welcome is the symmetry of the self-energy equation. Since Σ_{SCBA} is odd in its real and even in imaginary part with respect to Σ_{VCA}, SCBA will do well with systems of $c \approx 0.5$, but would (excluding $\delta \ll 1$ case) presumably fare worse otherwise.

Huge setback for SCBA is absence of structure, which would allow to either split band or give rise to another. This means that SCBA would necessarily fail for all systems in the split band limit (with $\delta \geq 2$).

These observations are confirmed in graphs A to C. The symmetric case C shows a good fit of SCBA to numerical DOS, but even then, there is shown hint at overflow at band edges. SCBA also proves to be applicable in very low concentrations as in A, when $\Sigma_{VCA} \approx \varepsilon_A$ and disregarding band edges and impurity peak the match of DOS is otherwise good. Graph B serves as an example in which are discussed bad traits most prominent.

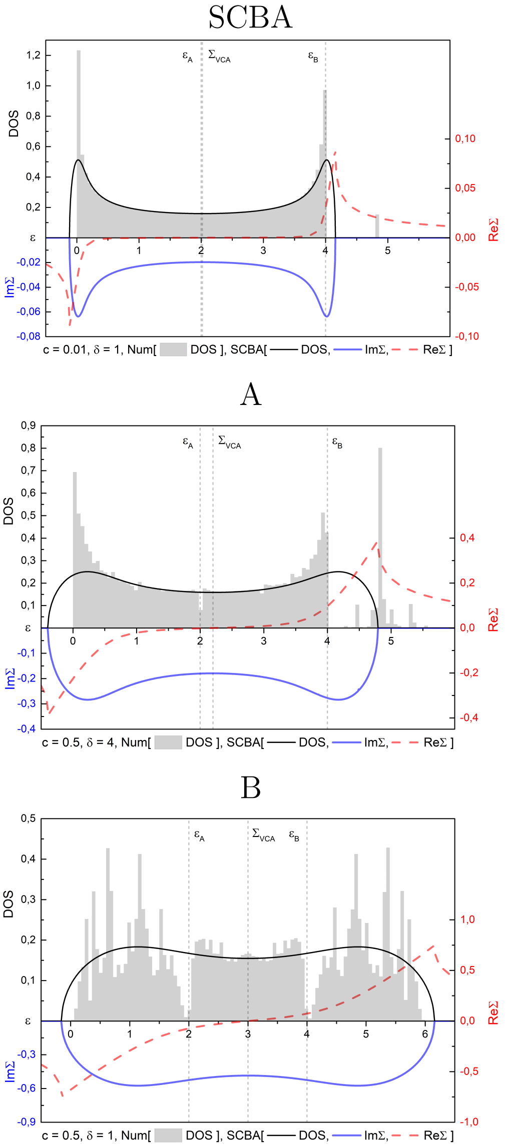

C

Figure 1.10: Chain $\left(\mathcal{H}_{1D}^{cb}\right)$ SCBA self-energy Σ and DOS. Comparison with numerical calculation of DOS. Constant scattering strength $\delta = 1$ for increasing concentration c, A 0.01, B 0.1 and C 0.5.

1.2.2 Coherent potential approximation

Outline of CPA derivation stripped of most finer points is provided in the appendix and more detailed description can be found in the original article [19] or in books concerning topic at hand, such as [8], or many others.

CPA in its simplest form presented here is known as the single site CPA (SSCPA) as opposed to various more complex CPA schemes, which seek to also incorporate cluster scattering and effects of short or long range order. As for others SSAs, self-energy Σ_{CPA} is scalar given by self-consistent (since $\overline{G}\left[\Sigma_{CPA}\right]$) equation

$$\Sigma_{CPA} = -\left(\varepsilon_A - \Sigma_{CPA}\right)\overline{G}_{00}\left(\varepsilon_B - \Sigma_{CPA}\right),$$

or writing explicitly VCA on-site potentials (1.40)

$$\Sigma_{CPA} = \Big[c(1-c)\Delta_\varepsilon^2 + (1-2c)\Delta_\varepsilon\Sigma_{CPA} - \Sigma_{CPA}^2\Big]\overline{G}_{00}. \tag{1.42}$$

Subscript CPA for self-energy Σ_{CPA} will be omitted in the following text.

Note that the CPA self-energy equation is symmetric with respect to concentration inversion and on-site energy switch. This feature is common with previously discussed ATA and SCBA and it is a necessary prerequisite for an approximation to appropriately function as a concentration interpolation scheme.

Since one of the concerns with simpler SSAs propelling search for better approximation was their inability to work properly in the entire concentration and scattering strength (1.36) parameter space $\{c, \delta\}$, it is vital to see how CPA fares in this regard. As a reminder note, hopping term t is not a nontrivial parameter due to the energy scaling invariance and, if not explicitly discussed as in the following section, the use of reduced units (1.11) is always assumed.

Exploration of the parameter space $\{c, \delta\}$ will begin with its limiting cases.

Sharp level limit

Limit of isolated sites (no hopping term) $t \to 0$, or equivalently $\mathcal{W} \to 0$ leads to site-diagonal full GF G (1.26) which in turn yields site-diagonal and translationally invariant effective GF

$$\overline{G}_{00}(z) \quad \longrightarrow \quad \frac{1}{z - \Sigma_{VCA} - \Sigma(z)}.$$

For CPA self-energy (1.42) is then

$$\Sigma = \frac{c(1-c)\Delta_\varepsilon^2}{z - \Sigma_{VCA} - (1-2c)\Delta_\varepsilon},$$

which is real valued leading to reducing density of states expression (1.30) to delta function

$$g(z) = \delta(z - \Sigma_{VCA} - \Sigma).$$

Its argument has two distinct roots

$$z_{1,2}\begin{cases}\Sigma_{VCA} - c\Delta_\varepsilon = \varepsilon_A \\ \Sigma_{VCA} + (1-c)\Delta_\varepsilon = \varepsilon_B\end{cases}$$

corresponding to energies of isolated sites ε_A and ε_B. Full expansion yields

$$g(z) = (1-c)\delta(z-\varepsilon_A) + c\delta(z-\varepsilon_B) \tag{1.43}$$

and CPA reproduces correctly both position of the energy levels and their weight.

The same result can be reached by assuming no scattering ($\tau = \infty$, $\mathrm{Im}[\Sigma] = 0$) and taking the imaginary part of the self-energy equation. Since (1.43) is the only solution, within the CPA non-zero DOS implies non-zero $Im[\Sigma]$ and vice versa.

Sharp level limit is also connected to seemingly different $\delta \to \infty$, but when taking into account the energy scaling invariance of the models, narrowing bands around the values of the on-site energies ε_A, ε_B while leaving their positions unchanged corresponds in preserved reduced energy unit representation (1.7) to the aforementioned high scattering strength limit.

It can also be seen on the Hamiltonian level in its site basis representation, where $t \to 0$ and $\delta \to \infty$ both break down the interacting system to a decoupled series of isolated sites.

Weak scattering and low concentration limits

Weak scattering limit $\Delta_\varepsilon \to 0$ (accompanied by $\Sigma_{VCA} \to \varepsilon_A$) and low concentration limit $c \to 0$ can be derived by expanding the self-energy equation (1.42) to the leading order in Δ_ε or c respectively.

$$\Sigma \overset{\Delta_\varepsilon \to 0}{=} c(1-c)\Delta_\varepsilon^2\overline{G}, \quad \Sigma \overset{c\to 0}{=} c\Delta\varepsilon^2\overline{G}_{00}\frac{1}{1-\Delta_\varepsilon\overline{G}_{00}}$$

Since effective GF is assumed to not diverge at any z (see Single site approximations), the $\Delta_\varepsilon \to 0$ limit is straightforward to perform and produces $\Sigma = 0$. Also note that in the small scattering regime, CPA yields SCBA self-energy (1.41).

Zero concentration case is more involved as the present fraction may diverge seemingly leading to a non-zero self-energy result. Closer inspection shows that such case is not possible, as for the divergence to be present, effective GF would need to be strictly real, which in turn mean zero DOS and also real self-energy. Lastly due to conserved particle number, i.e. integral DOS, there needs to be a band where $\Sigma = 0$ as a result of the present limit and due to its analyticity, that means $\Sigma = 0$ everywhere.

In conclusion, both limits correctly yield unperturbed pure system.

Solution choice

Self-consistent equations for self-energy (CPA, but also e.g. previously discussed SCBA (1.41)) are non-linear and in general have multiple solutions. In theory, one would have to solve the equations with proper restrictions and boundary conditions such that resulting Σ is not only a solution of a given self-energy equation, but also truly reflects physics of the system.

In practise, the systems of interest are usually too complex to hope for an analytical solution and self-energy equation needs to be solved numerically. In such cases, the present rules may provide a basis for a test to decide whether the calculated self-energy should be accepted or rejected as nonphysical.

The main set of conditions on solutions has its origin in general GF properties and particularly in their analyticity. For this purpose there are also very useful known limits such as (1.29).

(i) $Im\,[\Sigma] \leq 0$

(ii) Σ as a function $\mathbb{R} \to \mathbb{C}^*$ is not discontinuous (i.e. no 'finite jump' is allowed, while on the other hand pole in self-energy correspond to zero in GF and is therefore not impairing its analyticity).

(iii) $G(z) \to z^{-1}$ with $z \to \infty$

(iv) Preserving normalization of density of states (particle number or density conservation).

Another category consists of conditions emerging from properties of each given approximation. E.g. for CPA self-energy is [8]

(v) $\Sigma_{CPA} \to \langle \mathcal{V} \rangle = 0$ (VCA medium) as $z \to \infty$.

Self-energy solution selection is demonstrated in figure 1.11 for CPA self-energy in 1D cosine band case. Equation (1.42) can be expressed as a third degree polynomial equation for $\Sigma(z)$ for each energy z and in $\mathbb{C}^*$ has three distinct roots.

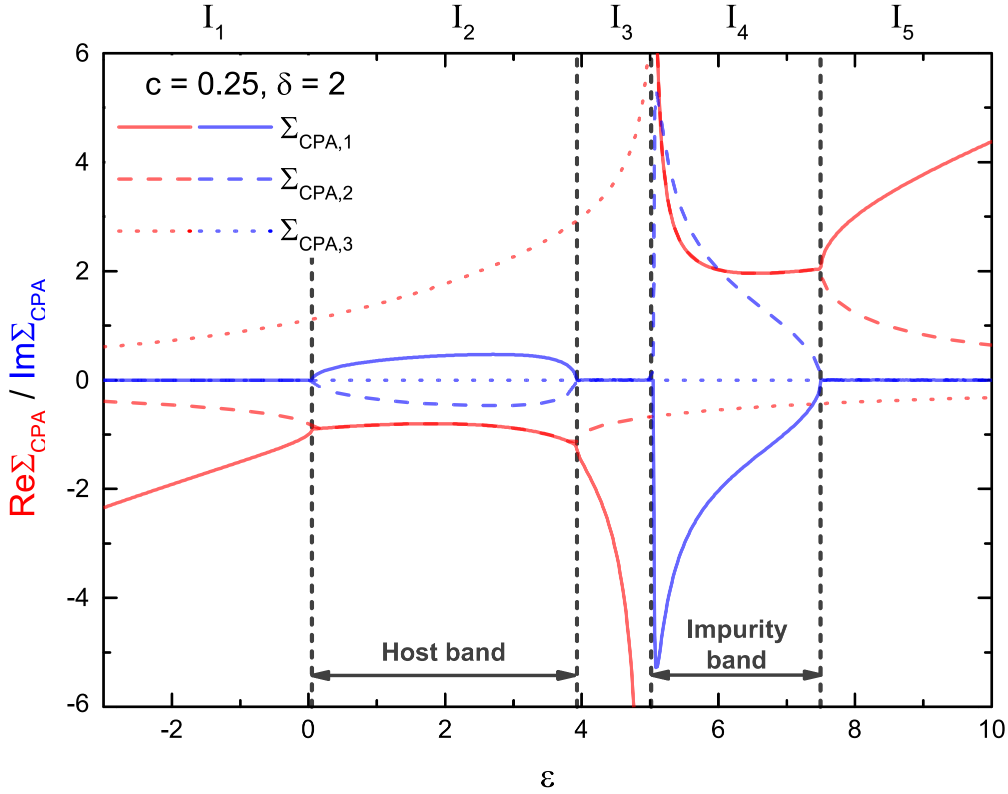

Figure 1.11: Chain $\left(\mathcal{H}_{1D}^{cb}\right)$ CPA self-energy equation root selection. Range is divided into 5 intervals $\{\mathbf{I}_1, \ldots \mathbf{I}_5\}$. On $\mathbf{I}_2$ is 3rd and on $\mathbf{I}_4$ 1st solution correct due to conditions (i) and (iv). Solutions on other intervals need to be connected continuously (ii), therefore on $\mathbf{I}_1$ and $\mathbf{I}_5$ is due to the (v) only 2nd solution correct. Similarly on $\mathbf{I}_3$ only 1st solution meets condition (ii).

Spanning the parameter space

With the question of limits answered and the border cases of the parameter space covered with CPA providing exact solutions, what remains to be seen is its applicability for the intermediate range of $\{c, \delta\}$.

1D chain model with GF (1.34) is employed for this purpose. The series of Σ and DOS for gradually increasing concentration c is shown in figure 1.12, covering near limit case $c \ll 1$ with $c = 0.01$, intermediate $c = 0.1$ and symmetric $c = 0.5$. Results are shown for two distinct scattering strengths: Albeit significant scattering with $\delta = 1$, but still far below the split band upper bound of the Gerschgorin circle theorem (1.35) ($\delta > 2$). This also provides a direct comparison with the results of ATA (1.9) and SCBA (1.10) results. As a representative of hight scattering strengths serves $\delta = 3$.

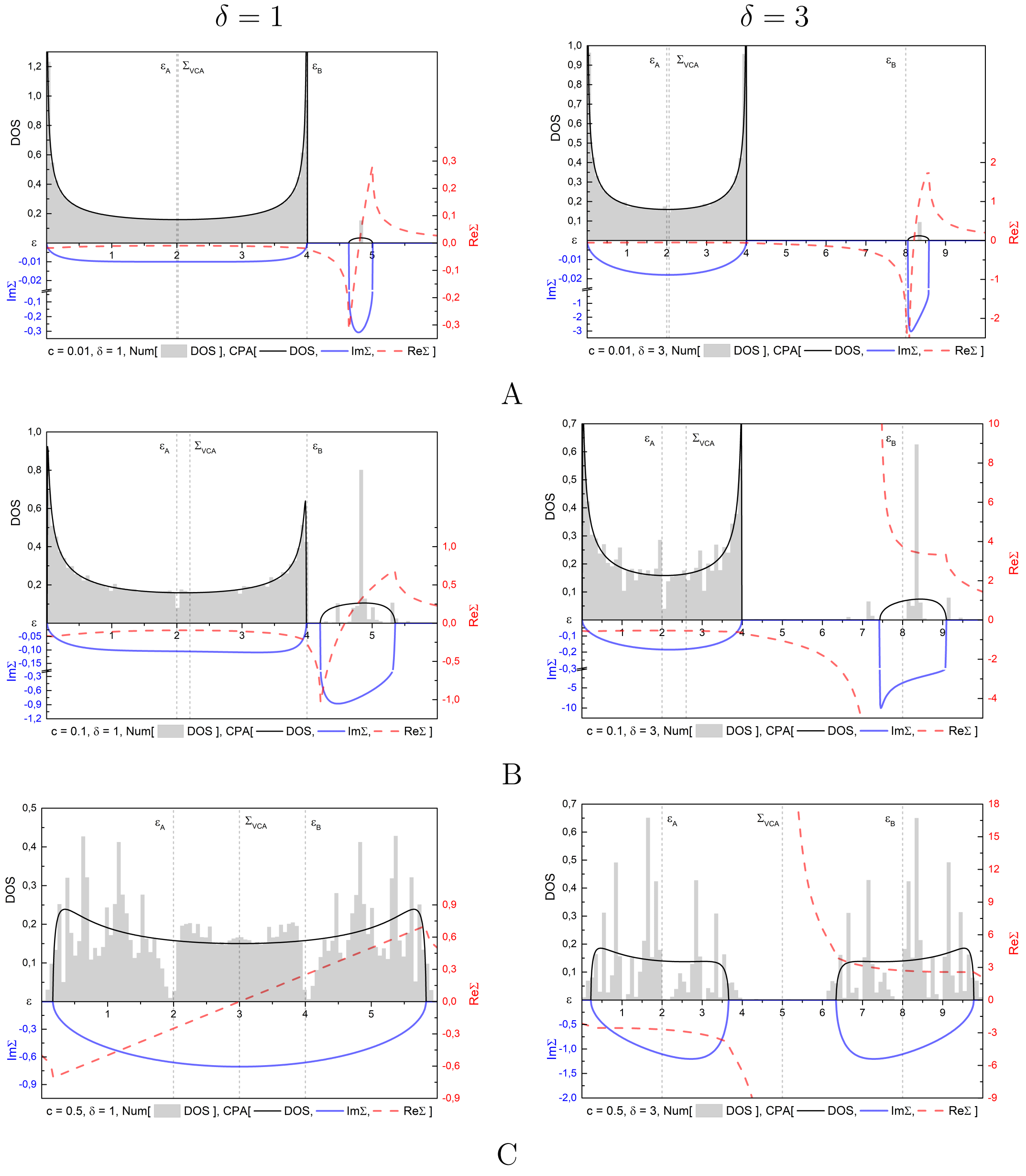

A

B

C

Figure 1.12: Chain $\left(\mathcal{H}_{1D}^{cb}\right)$ CPA self-energy Σ and DOS. Comparison with numerical calculation of DOS. Scattering strength $\delta = 1$ (left) and $\delta = 3$ (right) for increasing concentration c, from the top A $c = 0.01$, B 0.1 and C 0.5.

As was the case in the previous section, the results of numerical calculation of DOS for chain of length 10^8 sites are provided for comparison with CPA DOS.

Graphs 1.12 depict various regimes of CPA. 1C (as in $\delta = 1$, C) is a singular example of an undivided band with finite self-energy. 1A, 1B and 3A show detached impurity band with finite self-energy whose real part crosses zero within this band. Finally, self-energy in 3B and 3C has a pole and consequently GF a zero in the band gap region.

While emergence of the impurity peak or band reflects the system at hand, the self-energy pole is an inherent CPA feature. One can see that in a split band case. For a given concentration c increasing the scattering strength δ leads to a shift in energy z where $Re[\Sigma]$ changes sign from within the impurity band closer to inner band edge until sufficient strength is reached and a pole emerges at the very edge of the impurity band. More on this behaviour in [19].

As can be seen in 1.12, CPA handles rather well all present cases. It successfully avoided pitfalls of impurity band emergence, failed in one form or another in SCBA and ATA, and predicts scattering in a whole band (or bands).

Still, despite CPAs advantages and successes, presented graphs reveal one of its shortcomings. Namely, its persistent inability to properly describe band edges. It is a case especially with the impurity band for lower concentrations and albeit not so badly for both bands in a more balanced material.

This relates back to general discussion of failings of SSAs and their inability to capture band edge behaviour and finer intraband structures corresponding to long range order and local environment correlations respectively.

It was shown that CPA is usable as an interpolation scheme in the entire $\{c, \delta\}$ parameter space and comparison with some other used approximation as well as their analysis [8] proved it to be the superior approximation within the realm of SSAs.

1.2.3 Hall coefficient calculation

The form of a linear electric field **E** response conductivity tensor for the CPA decoupling scheme was first presented in 1969 [19] and the electric **E** and magnetic **B** field bilinear response conductivity tensor a year later [23].

The results of their derivations (in the later article [23]) were written in the form of effective densities, equations (63a) and (64b), and integrals, (64a) and (64b), with the CPA self-energy as a single input parameter besides pure material band structure.

In the current framework, they can be succinctly written using of FS integrals ϕ_{xx}, ψ_{yx} (1.4) as

$$\Phi(\varepsilon) = \int \kappa_\phi(\varepsilon - \Sigma - \Sigma_{VCA} - \varepsilon')\phi_{xx}(\varepsilon')d\varepsilon', \quad \kappa_\phi(x + iy) = \frac{1}{\pi}\frac{2y^3}{(x^2 + y^2)^2} \quad (1.44)$$

$$\Psi(\varepsilon) = \int \kappa_\psi(\varepsilon - \Sigma - \Sigma_{VCA} - \varepsilon')\psi_{yx}(\varepsilon')d\varepsilon', \quad \kappa_\psi(x + iy) = \frac{1}{\pi}\frac{8y^5}{3(x^2 + y^2)^3}, (1.45)$$

with κ_ϕ and κ_ψ disorder integration kernels. Disordered system Hall coefficient R_H^* is then given by formally same expression to that of pure material R_H (1.6) as

$$R_H^* = -\frac{1}{e}\frac{\Psi}{\Phi^2}. \tag{1.46}$$

Band structure dependence is therefore recovered in the low field $\mathbf{B}$ linear regime from the full quantum description utilising GFs as the conductivity tensors (1.5) ($\propto$ Φ and Ψ respectively) are given by integral transforms of their pure translationally invariant counterparts.

Note the limiting behaviour of disorder kernels

$$\kappa_\phi(x+iy) \to \delta(x), \quad \kappa_\psi(x+iy) \to \delta(x), \qquad \text{as} \qquad y \to 0,$$

applied in the zero-scattering limit

$$R_H^*(\varepsilon) \to R_H(\varepsilon - \Sigma_{VCA} - Re[\Sigma]), \qquad \text{as} \qquad Im[\Sigma] \to 0,$$

which results in simple shift in energy argument of pure R_H. This case ($Im[\Sigma] \ll Re[\Sigma]$) was studied in more detail for the cubic lattice $\mathcal{H}_{3D}^{cb}$ in [23].

Lastly limits $c \to 0$ and $\delta \to 0$ (weak scattering and low concentration limits)

$$R_H^*(\varepsilon) \to R_H(\varepsilon), \qquad \text{as} \qquad c \to 0 \text{ or } \delta \to 0,$$

yield correctly pure material R_H.

The next point concerns the disorder kernels κ, shown in graph 1.13. Since they are both real, positive and symmetric, the pure material discussion of the Hall coefficient sign is largely left unchanged. Second, inclusion of the disorder via the integral form (1.44) and (1.45) is reminiscent of the temperature averaging (1.16), since both involve a single sharply peaked function (albeit in the disorder case usually much broader). Important distinction here is the different kernel used for ϕ_{xx} and ψ_{yx} FS integrals, while thermal averaging is the same for both.

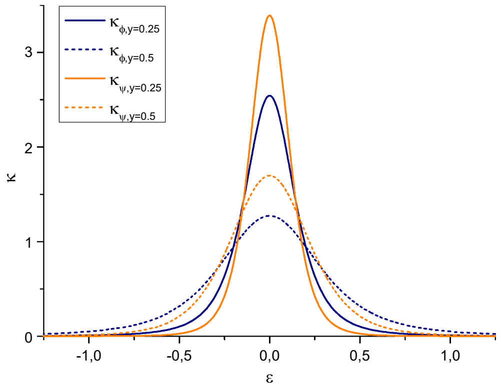

Figure 1.13: Graphs of disorder integration kernels κ_ϕ and κ_ψ centred at zero for $iy = 0.25$ and 0.5.

Lastly, the inclusion of temperature is straightforward in this point, as it consists again of thermal averaging of the form (1.16) only now with the disorder variant of the FS integrals Φ and Ψ instead of pure material ones [19].

Results for square Lattice

Self-energy was calculated via simple iteration of CPA equation (1.24) employing relaxation via parameter ω

$$\Sigma_{new} = \omega \Sigma_{CPA}[\Sigma_{old}] + (1-\omega)\Sigma_{old},$$

usually with $\omega \approx 0.1$ so that the iteration converges. Despite this, the algorithm for ε in the region of the band gap and near the inner band edges did not converge, and extrapolation from complex valued z to the real axis was unsuccessful, as the problematic region tends to extend far from the real axis. The results presented here are thus limited to lower scattering strength $\delta = 0.5$ (A) and $\delta = 1$ (B) for three concentrations, $c = 0.01$, figure 1.14, $c = 0.1$ 1.15 and lastly $c = 0.5$ 1.15.

To provide a comparison for the CPA results, DOS was calculated by means of diagonalisation of the Hamiltonian site representation sparse matrix $\mathbf{H}_{2D}^{cb}$ with a fixed lattice size of 100 × 100 sites.

Hall coefficients are obtained using (1.46), with exact FS integrals ϕ_{xx}, ϕ_{yx} (1.14) approximated with their interpolation functions to speed up the calculation (see discussion in R_H calculation for square lattice model). For a pure material DOS and R_H recall 1.5 in the same section.

Following that, the $-n_c R_H$ quantity is accompanying R_H plots, but unlike its pure counterpart without usable analytical expressions for both $R_H(\varepsilon)$ and $g(\varepsilon)$, the band edge limits could not be computed. The closest approximation would probably involve interpolation of both the CPA DOS and the Hall coefficient and using its derivative instead, but the general struggle of CPA to capture band edge behaviour renders this question meaningless, as the approximation itself is in the first place not suited for such task.

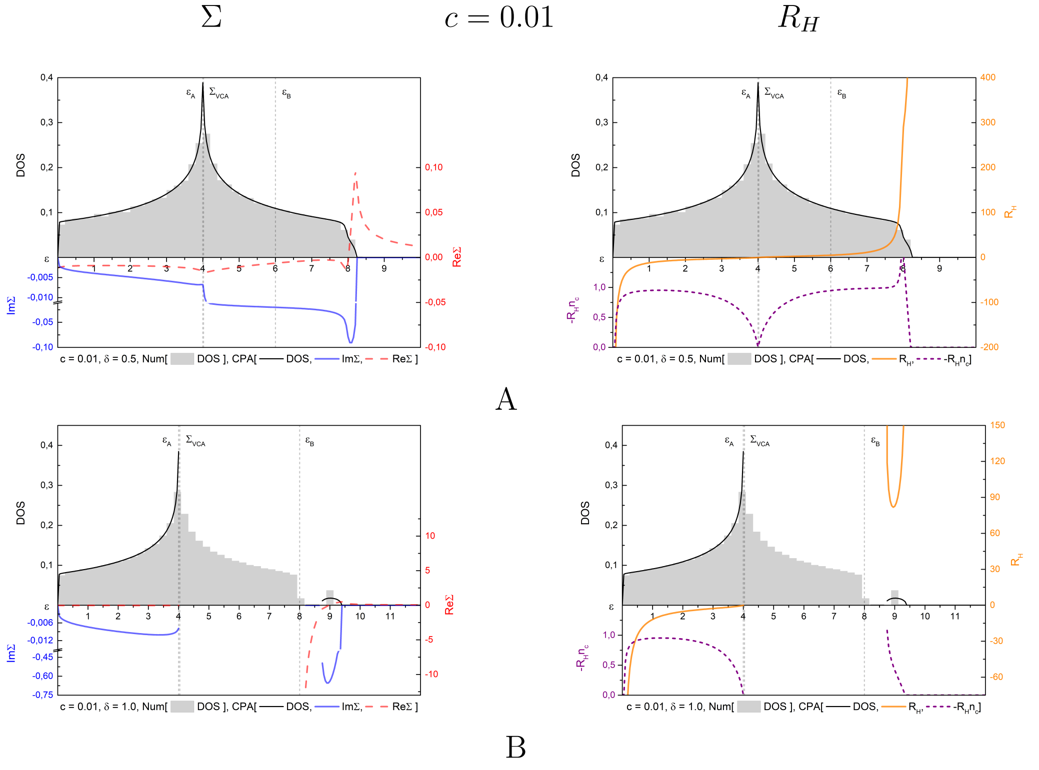

Figure 1.14: Square lattice $\left(\mathcal{H}_{2D}^{cb}\right)$ numerical and CPA DOS, self-energy Σ (left) and R_H (right). Fixed $c = 0.01$ for (A) $\delta = 0.5$ and (B) 1.

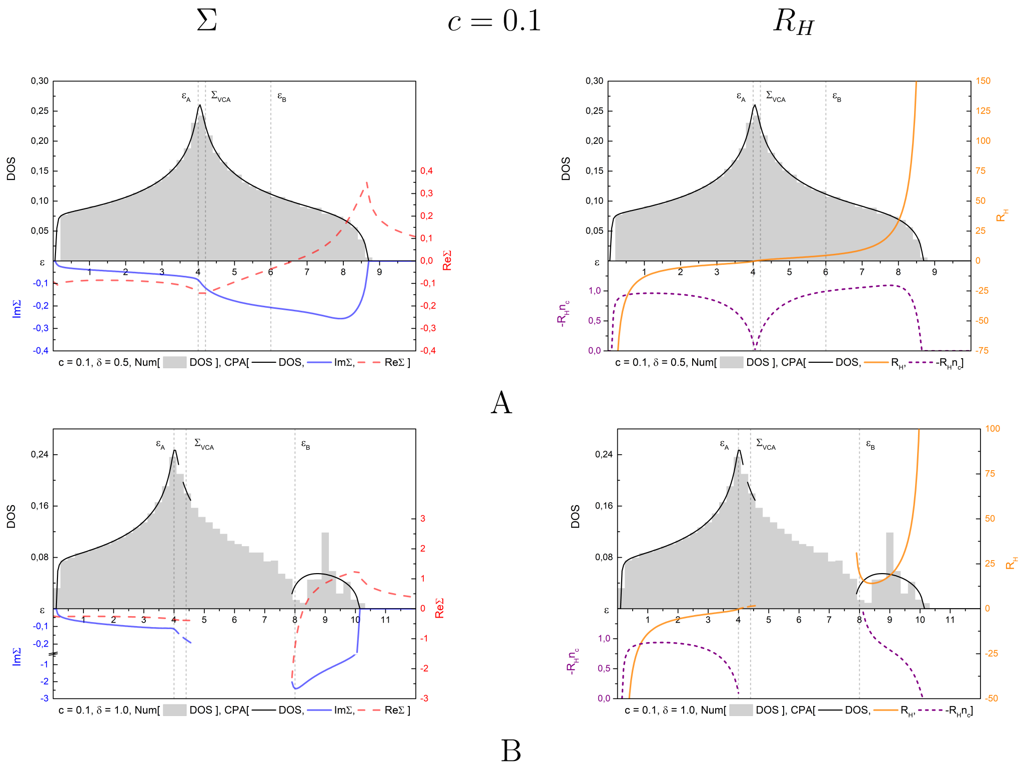

Figure 1.15: Square lattice $\left(\mathcal{H}_{2D}^{cb}\right)$ numerical and CPA DOS, self-energy Σ (left) and R_H (right). Fixed $c = 0.1$ for (A) $\delta = 0.5$ and (B) 1.

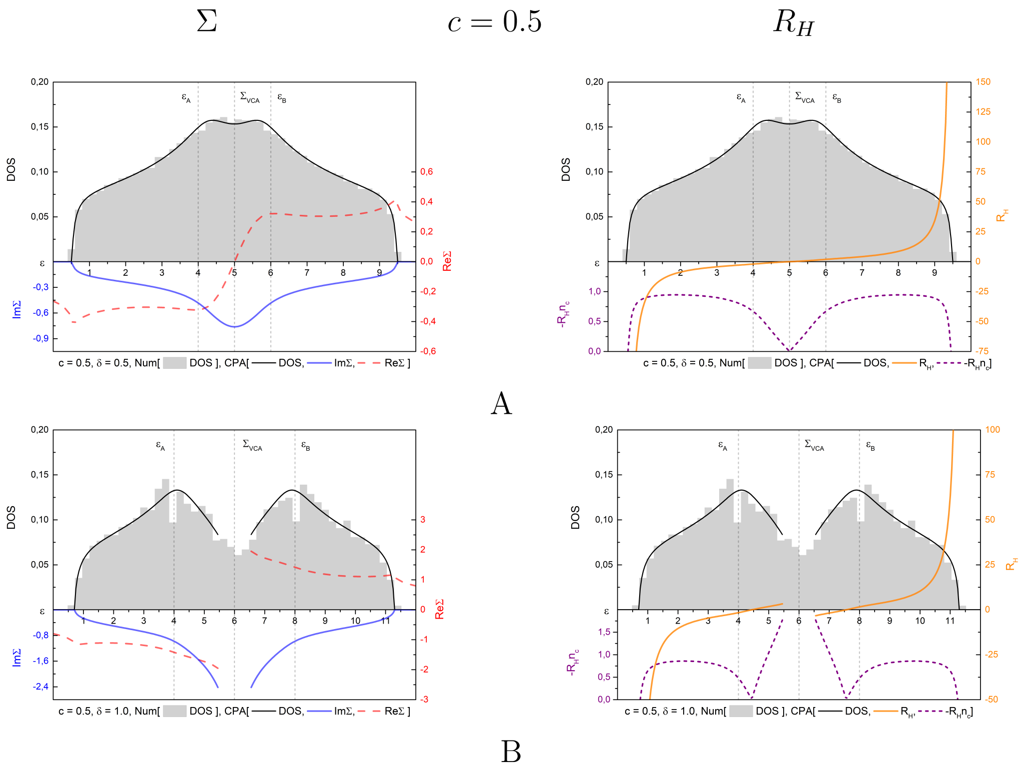

Figure 1.16: Square lattice $\left(\mathcal{H}_{2D}^{cb}\right)$ numerical and CPA DOS, self-energy Σ (left) and R_H (right). Fixed $c = 0.5$ for (A) $\delta = 0.5$ and (B) 1.

The concentration dependence of the Hall coefficient R_H absolute value for various electron densities n is shown in figure 1.17. Constant electron density is assumed, i.e., same valence of both host and impurity atoms, and therefore the alloying leads only to changing Σ profile and DOS distribution, which is in turn responsible for shift in Fermi energy ε_F. More generally, one would need to include n_{Alloy} (1.1) concentration dependence.

The first thing to note is the symmetry of R_H, as it is an odd function of c with respect to simultaneous mirroring of concentration with respect to $c = 0.5$ and the same for density n and $n = 0.5$.

This comes as no surprise, as the DOS and CPA Σ are in the process just flipped together with Fermi energy ε_F and the change of sign simply reflects different majority carriers. For the $c = 0.5$ itself (graphs 1.16) the symmetry is then reduced to all present quantities being even or odd with respect to the Σ_{VCA}, i.e., $n = 0.5$ point.

Despite nontrivial effects of disorder that can be seen in the 1.17, Hall coefficient behaviour does not qualitatively change within the presented framework and for all shown densities n full R_H curve remains in the vicinity of pure material line (i.e. VCA interpolation scheme, which leaves R_H constant).

Its influence on R_H is most pronounced at the edge of the host band, which would with a sufficiently high strength δ split off to form the impurity band, while having only marginal effect in comparison deep within the host band. This can be clearly seen e.g. from the flat profile of the low n lines for $c < 0.5$ and on the other hand from the bend of the hight n R_H curves for $c > 0.5$.

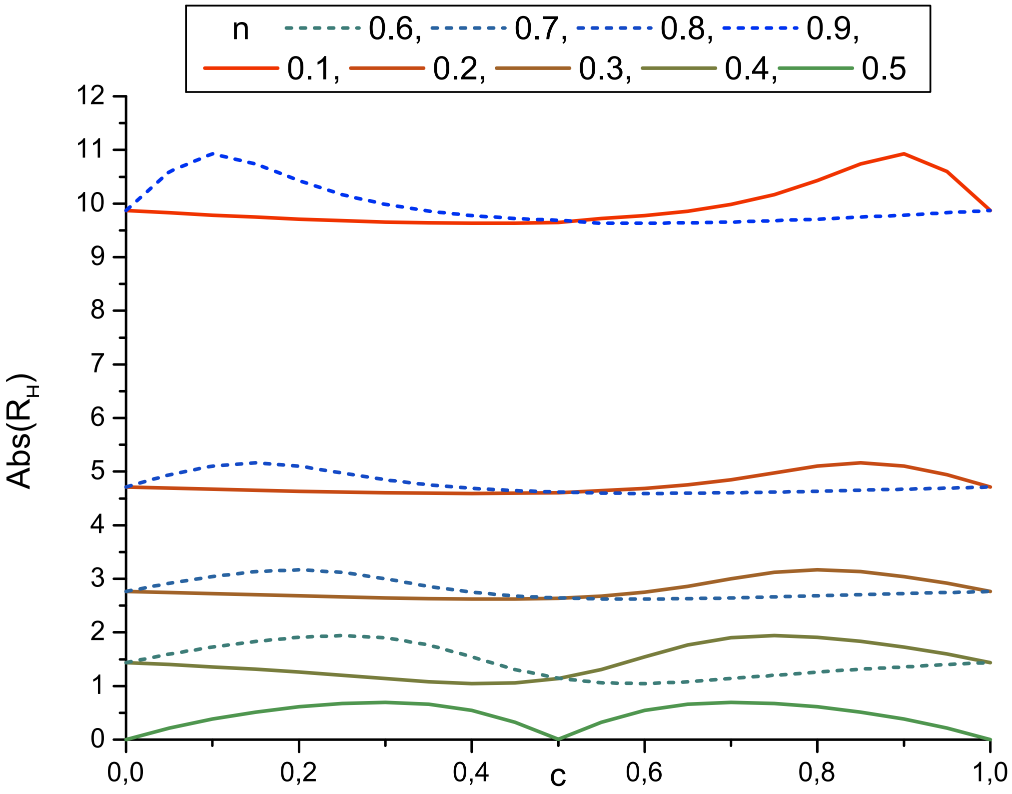

Figure 1.17: Square lattice $\left(\mathcal{H}_{2D}^{cb}\right)$ constant $\delta = 0.5$ Hall coefficient R_H dependency on concentration c for various values of fixed electron density n.

The relative change ($\Delta R_H(c)$ over pure R_{H0}) is highest near $n \approx 0.5$ where it is natural to expect a change in the majority carriers and R_H zero crossing. Figures 1.14 and 1.15 confirm such expectation for at least relatively wide c and δ range, but also note figure 1.15 whose B graph ($\delta = 1$) indicates that the position of Hall coefficient zeros may be especially at higher strengths δ much harder to predict.

Unlike previously discussed temperature dependence, the absolute change in Hall coefficient ΔR_H is for all n of the same order of magnitude. Also, unlike inclusion of temperature which tends to lower the system Hall coefficient as seen in 1.8, examined disorder leads to increase in R_H near the band edge from which would impurity band separate in higher δ and where is the effect most prominent.

The effects of disorder are when disregarding energy region deep within host band (low n) and near symmetric constitution $c \approx 0.5$ of the order $\Delta R_H \lessapprox R_{H0}/10$.

Comparison with (1.23) leads to the conclusion that it is reasonable to expect the disorder effects to be up to an order of magnitude lower than pure material Hall coefficient and any thermal effects at least and additional order smaller.

1.3 Application for Hall sensors

Central requirement for the sensing layer material of the Hall sensors is naturally hight Hall coefficient as it is the proportionality parameter of the measured Hall voltage. While it may be difficult to precisely determine R_H in complex materials, it retains its strong dependence on carrier density n_c. This was seen explicitly in the case of the classical Drude model (1), and in previous sections in semi-classical free electron R_H^{eg} (1.9), square lattice R_H^{2Dcb} 1.5 and even in square lattice based binary substitutional alloy 1.17.

It is therefore no surprise that semiconductor Hall sensors are in this regard superior, with R_H orders of magnitude higher than metal based ones. However, the picture becomes much less unambiguous when taking into account specific operational conditions.

ITER and DEMO fusion projects in particular present an interesting challenge as their sensors must be operational in relatively high temperatures and be sufficiently radiation resistant, as they are exposed to high neutron flux during the fusion, which leads to sensor degradation via neutron capture and transmutation of sensing layer atoms.

Semiconductor sensors are especially prone to this because element transmutation in their case is akin to doping of the original material, which vastly increases carrier density and thus reduces sensitivity.

Requirements for the ITER outer vessel steady state sensors (OVSS) were operation temperature range of 27 ^oC up to 127 ^oC and the need to withstand peak temperatures up to 220 ^oC in separate baking cycles and total neutron fluence of 1.3x10^{22} n/m^2.

Bismuth proved to be applicable in this case [24]. As a semimetal it is much more stable against neutron flux degradation, while it keeps high Hall coefficient, which may be depending on doping even comparable to semiconductors.

This is no surprise, as its Fermi surface (depicted in 1.18) consists of only two tiny sheaves, which mirror transport behaviour of the n-type semiconductor in the vicinity of the L point (leading to 3 electron pockets, each at one of the L points of the Brillouin zone) and the p-type near the T point (responsible for one hole pocket)[25].

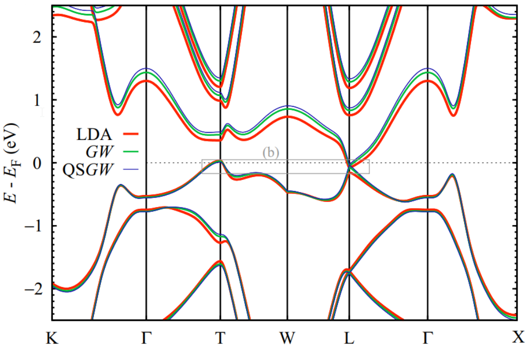

Figure 1.18: Bulk Bi band structure as calculated using various numerical methods. Source [25].

DEMO has yet harder requirements to meet, as the operational temperature here ranges from 300 ^oC up to 520 ^oC, which exceeds 271.4 ^oC the melting temperature of otherwise very promising bismuth. This strict criterion opens up a space for metal based Hall sensors with chromium as the leading candidate [7].

Temperature dependence

Sensor sensitivity S_H (proportional to the Hall coefficient of the sensing layer material R_H) temperature dependence for various sensing layer materials is shown in figure 1.19. Bismuth and antimony are semi-metals, and the rest are metals.

Semiconductors whose transport is thermally (or otherwise) activated have carrier density exponentially dependent on the operating temperature, and semiconductor sensors have therefore Hall coefficient and sensitivity inverse proportionally diminishing.

As seen in 1.19 the same holds at least in a wide temperature range in the case of semi-metals bismuth and antimony.

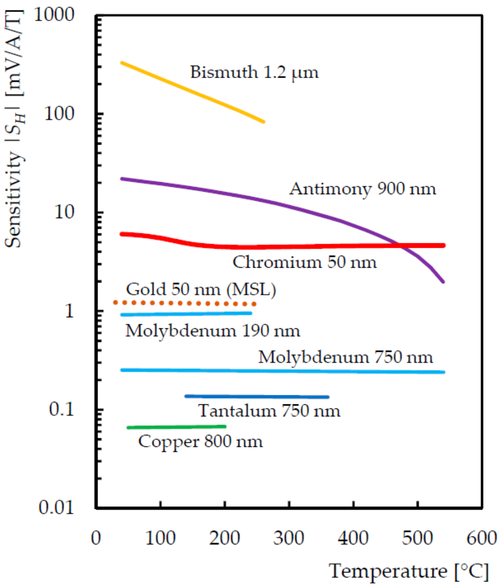

Figure 1.19: Sensitivity of semi-metal and metal Hall sensors temperature dependence. Source [7].

The behaviour of metals qualitatively differs, with in comparison negligible temperature dependence. Chromium in the temperature range below 200 ^oC is a notable exception. It is anti-ferromagnetic below 35 ^oC and it is speculated [24], that exhibited behaviour is connected with gradual disappearance of the short range magnetic order above this temperature.

As an explanation of the high temperature chromium (and for other metals more generally) Hall coefficient temperature independence was in [7] used result of semi-classical free electron gas model presented in section Sommerfeld expansion and electron gas.

Alloys, disordered materials and future outlook

Recent need of Hall sensors for specific conditions motivates the search for new materials. While pure materials have been a focus of this search so far, the question of applicability of various alloys remains open and largely unexplored.

Additionally, particular hardship even for a pure sensing layer materials presents prediction of R_H after long-term exposure to a high neutron flux.

Sensing layer content after given neutron fluence exposure can be predicted by simulating neutron-induced transmutations, but the crux of the matter lies in the determination of its Hall coefficient. Simplistic approximations based on shift in carrier density or Fermi surface of the pure material as RBA or VCA can be employed, but the true extent of the effects may be much more complex and their realistic description would require substitutionally disordered material or alloy based model.

There is thus a need for usable alloy model for Hall coefficient calculation and section Substitutionally disordered materials serves as an initial exploration of the problem.

2. Integer Quantum Hall Effect

Treatment of magnetic field and its effects on transport properties is as a rule with only few exceptions limited to semi-classical calculations which uses the band structure as an input. Even more complicated approaches and methods which strive to extend scope of its applicability usually retain connection to the unperturbed band structure or are only able to provide information about low magnetic field linear effects.

This was the case in the previous chapter with the approximations seeking to provide realistic description of the disordered systems. While they all utilised full quantum description of the tight binding lattice, magnetic field was later introduced only as the first order linear perturbation and the resulting expressions explicitly contained quantities related to pure material band structure.

While these endeavours may be sufficient for given problem at hand, the realistic high field transport model would necessarily has to be completely decoupled from the band structure description as it would have to take into account formation of the Landau levels (LL), the very defining feature of high (quantizing) magnetic field .

Section Square lattice model is dedicated to study of this gradual emergence and evolution of the LLs in the square lattice model with magnetic field introduced via Peierls substitution. Outlook for the more complex three dimensional lattices is discussed in the section, Models of realistic materials - Outlook.

2.1 Square lattice model

Standard method of introduction of homogeneous magnetic field into the lattice models is well known Peierls substitution

$$|j\rangle\langle i| \quad \longrightarrow \quad e^{-i\phi_{ij}}|j\rangle\langle i|, \quad |i-j|=1,$$

where phases ϕ_{ij}

$$\phi_{ij}=\frac{e}{\hbar}\int_{\mathbf{r_i}}^{\mathbf{r_j}}\mathbf{A}\cdot d\mathbf{r} \tag{2.1}$$

are calculated using shortest trajectory between the neighbouring sites.

Specially in the case of square lattice model (1.10), whose transport properties are examined in detail in previous chapter, is

$$\mathcal{H}^{\Delta\phi}=\varepsilon_0\sum_i|i\rangle\langle i|+t\sum_{|i-j|=1}|i\rangle\langle j|. \tag{2.2}$$

As was the case before, energy scaling and translation invariance of its time-independent Schrödinger equation are utilized allowing use of the reduced energy units (1.11). Meaning in practice here setting $t=1$ and, for simplicity, $\varepsilon_0=0$. Recall DOS of pure square lattice $\mathcal{H}^{\Delta\phi=0}$, 1.5.

Assuming $\mathbf{A}=B(0,x,0)$ gauge and the lattice vectors aligned with the axes, general (2.1) yields relation of the phases and magnetic fields in a very simple form

$$\frac{a}{\ell}=\sqrt{\Delta\phi},$$

where a is a the square lattice constant and $\Delta\phi$ stands for the spacing between phases of consecutive hopping terms in the **y** direction. Phases associated with hopping along **x** axis are all zero.

The unitless a/ℓ comparison of the characteristic scales, that of the system and the characteristic magnetic quantum scale, then serves as a natural quantity in whose terms one can express magnetic field dependencies.

Even this relatively simple model contains a very rich self-similar fractal structure with an infinite number of separate levels, or zero-temperature phases as it is, enumerated with topological Chern numbers, with corresponding quantized integral conductance [1]. In the figure 2.1 is depicted this zero temperature fractal phase diagram, which is due to its wing-like shape known as the Hofstadter butterfly.

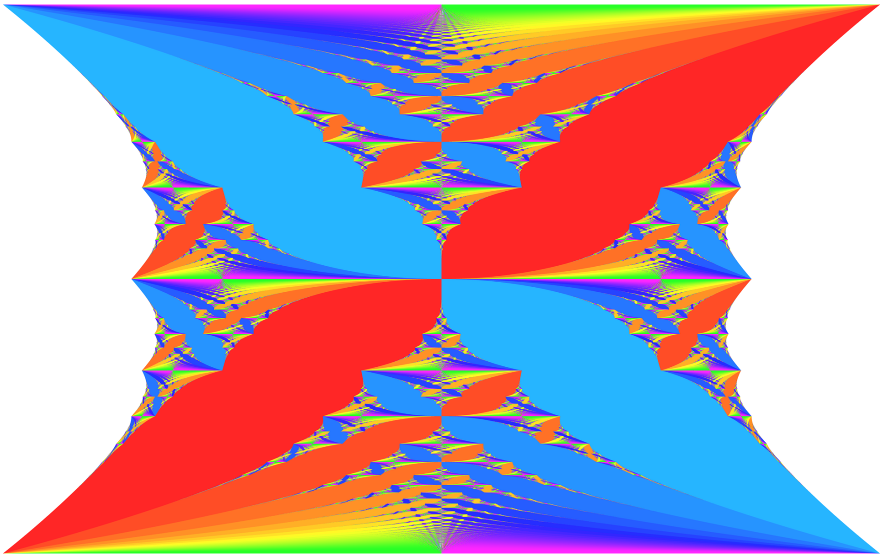

Figure 2.1: 'Hofstadter butterfly'. Energy (chemical potential) on the horizontal axis and magnetic field (flux) on the vertical. Warm colours corresponding to positive Chern numbers and cool to negative. Source [1].

The introduction of the magnetic field in the Hamiltonian (2.2) leads to breaking of the translational symmetry of the lattice as the periodicity of the phases ϕ_{ij} has to be taken into account. Only larger magnetic unit cell, in the present case given by condition

$$\Delta\phi N_y = 2\pi k_{\Delta\phi}, \quad k_{\Delta\phi} \in \mathbb{Z}.$$

remains properly translationally invariant.

In practise this means that matrix representation $\mathbf{H}^{\Delta\phi}$ of given periodic supercell $N_x \times N_y$ can describe only systems with field fulfilling the following condition.

$$\frac{a}{\ell} = \sqrt{\frac{2\pi k_{\Delta\phi}}{N_y}}, \quad k_{\Delta\varepsilon} \in \mathbb{Z}$$

2.1.1 Discretization metric

In order to quantify the LL formation in the increasing magnetic fields, it would be welcome to have some DOS clustering measure, e.g. which would be high when there are present prominent sharp LLs and low otherwise.

With this goal in mind, first adopting equienergy partition of the energy axis ε into bins, with energy spacing $\Delta\varepsilon$. Then, i-th bin contains n_i energy eigenvalues of the given matrix representation $\mathbf{H}^{\Delta\phi}$ of (2.2) and

$$N = \sum_i n_i$$

is the degree of that representation.

Then introducing partition dependent 'discretization metric'

$$\mathcal{D}_{[\Delta\varepsilon]} = \frac{1}{2N} \sum_i |n_i - n_{i-1}|, \tag{2.3}$$

which is constructed in such a way to reflect presence of the sharp peaks in the DOS histogram with $\Delta\varepsilon$ spacing.

$\mathcal{D}_{[\Delta\varepsilon]}$ is owing its name to the fact that it reaches its maximum value precisely when all energy eigenvalues within $\Delta\varepsilon$ bin are separated by at least one bin of the same length from the others. That is, when the DOS quasi-continuum of $\mathbf{H}^{\Delta\phi}$ breaks apart to discrete energy levels. On the other hand, $\mathbf{H}^{\Delta\phi}$ reaches 0 only when the DOS histogram is completely flat.

The prefactor $1/2N$ ensures that $\mathcal{D}_{[\Delta\varepsilon]} \leq 1$, which can be easily seen, e.g. by assuming single N-times degenerate level, which is then in the sum (2.3) counted twice.

Note that as long as N is finite, for all systems is $\mathcal{D}_{[\Delta\varepsilon]} \to 1$ as $\Delta\varepsilon \to 0$, since with respect to arbitrarily small bin partitioning, all energy eigenvalues are well separated.

2DEG in magnetic field and $\mathcal{D}_{[\Delta\varepsilon]}$ behaviour

Simple, well-known, ideal 2DEG model in magnetic field, with equidistant LL spacing provides a good test of applicability for the discretiazation metric $\mathcal{D}_{[\Delta\varepsilon]}$ and sheds more light on its behavior.

In the figure 2.2 it can be seen that equidistant LL spacing $\hbar\omega_c$ leads to $\mathcal{D}_{[\Delta\varepsilon]} = 1$ when $\Delta\varepsilon \leq \hbar\omega_c/2$.

Further increasing the spacing $\Delta\varepsilon$ results in a drop in $\mathcal{D}_{[\Delta\varepsilon]}$ as sequences of consecutive bins containing LL energy become more common and $\mathcal{D}_{[\Delta\varepsilon]}$ vanish completely when the spacing $\Delta\varepsilon = \Delta\varepsilon = \hbar\omega_c$ as the related histogram becomes completely flat.

More generally, the $\mathcal{D}_{[\Delta\varepsilon]}$ vanishing condition is $\Delta\varepsilon = k\hbar\omega_c$ for $k \in \mathbb{N}$, where k is the integer number of LLs contained in each bin.

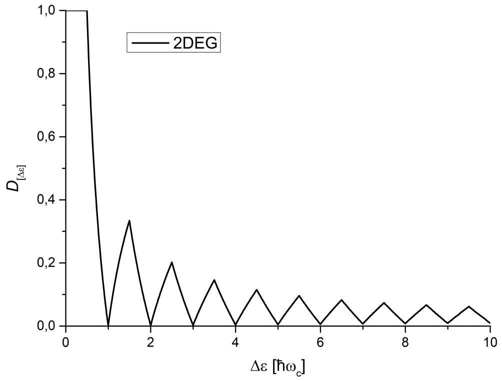

Figure 2.2: Ideal 2DEG in external magnetic field, $\mathcal{D}_{[\Delta\phi]}$ as a function of energy spacing $\Delta\varepsilon$.

Diminishing fluctuations for spacing $\Delta\varepsilon \neq k\hbar\omega_c \; k \in \mathbb{N}$, $\Delta\varepsilon > \hbar\omega_c/2$ originated from the periodic oscillatory behavior of the underlying histogram, where some bins cover one more LL than others. As $\Delta\varepsilon$ increases, these fluctuations diminish in amplitude as each bin contains more and more LLs, and eventually in the $\Delta\varepsilon \to \infty$ they vanish completely.

In general, disregarding the very limit $\mathcal{D}_{[\Delta\varepsilon]} \to 1$, $\mathcal{D}_{[\Delta\varepsilon]}$ increases with decreasing $\Delta\varepsilon$ when $\Delta\varepsilon \approx \Delta\varepsilon'_{LL'}$ (i.e., when it crosses some periodic peak spacing). On the other hand, $\mathcal{D}_{[\Delta\varepsilon]}$ falls off with decreasing $\Delta\varepsilon$ when the spacing becomes comparable with the peak width.

2.1.2 Results

All results in this subsection are obtained using Wolfram Mathematica software for the fixed Lattice size 37 × 200 sites (7400 sites in total) with the periodic boundary condition. Chosen rectangular lattice allows to reach lower fields with a minimum phase step $\Delta\phi = 2\pi/200$.

Spectra were calculated for a series of $\mathbf{H}^{k_\Phi \Delta\phi}$, $k_\phi \in \{1, 2, \dots, 30\}$, which corresponds to $a/\ell \in \{0.177245, 0.250663 \dots, 0.970813\}$. Figure 2.3 shows the values of the discretization metric with spacing $\Delta\varepsilon = 0.1$, which was chosen so that $\mathcal{D}_{[0.1]}$ can capture the formation of the LL structure both in low and high fields. That is, to be small with respect to the whole spectrum bound of $\mathbf{H}^{k_\Phi \Delta\phi}$ (8) and sufficiently big with respect to forming LLs width even in higher fields.

Since the 2DEG DOS continues periodically and indefinitely into hight energies, selection of the initial energy for the bin partitioning did not have any effect on $\mathcal{D}_{[\Delta\varepsilon]}$ values.

This is not the case here, as in the bounded systems does not have the 'benefit' of the indefinite repetition of the 2DEG DOS. As a starting point of the analysis is chosen $\varepsilon_0 = 0$ as the initial energy value for the partitioning to reflect symmetry of the problem.

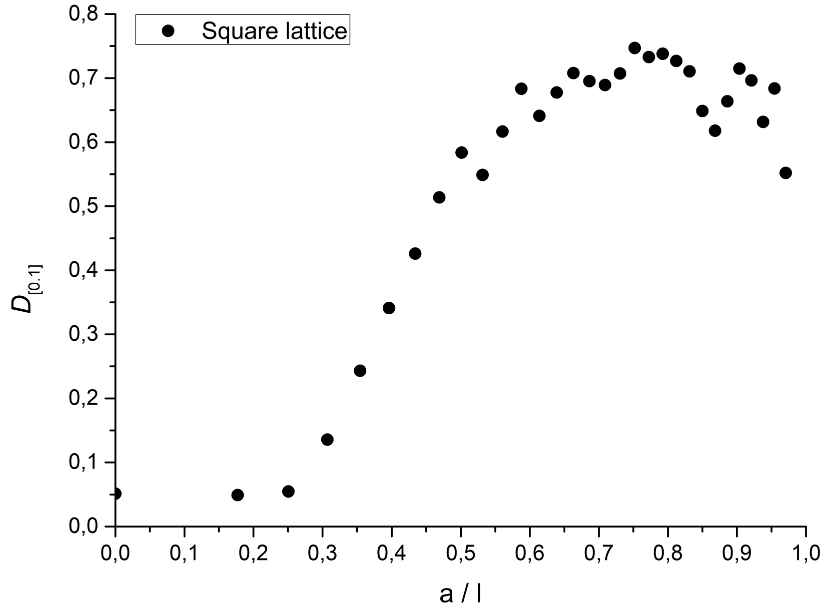

Figure 2.3: Square lattice tight binding $\mathcal{D}_{[0.1]}$ in increasing magnetic field.

The metric $\mathcal{D}_{[0.1]}$ in figure 2.3 shows four distinct regimes.

(1) ($a/\ell \lessapprox 0.3$) $\mathcal{D}_{[0.1]}$ as a function of ϕ (magnetic field) is near constant

(2) ($a/\ell \in \approx \langle 0.3, 0.6\rangle$) steep increase in $\mathcal{D}_{[0.1]}$

(3) ($a/\ell \in \approx \langle 0.6, 0.8\rangle$) $\mathcal{D}_{[0.1]}$ flattens

(4) ($a/\ell \gtrapprox 0.8$) $\mathcal{D}_{[0.1]}$ begins to fall off

To make sense of this dependence, four distinct k_ϕ, $\{3, 7, 17, 30\}$, corresponding to the turning point or characterizing a given regime were chosen for further analysis. Their DOS histograms, with $\Delta\varepsilon = 0.1$ spacing, are shown in 2.3.

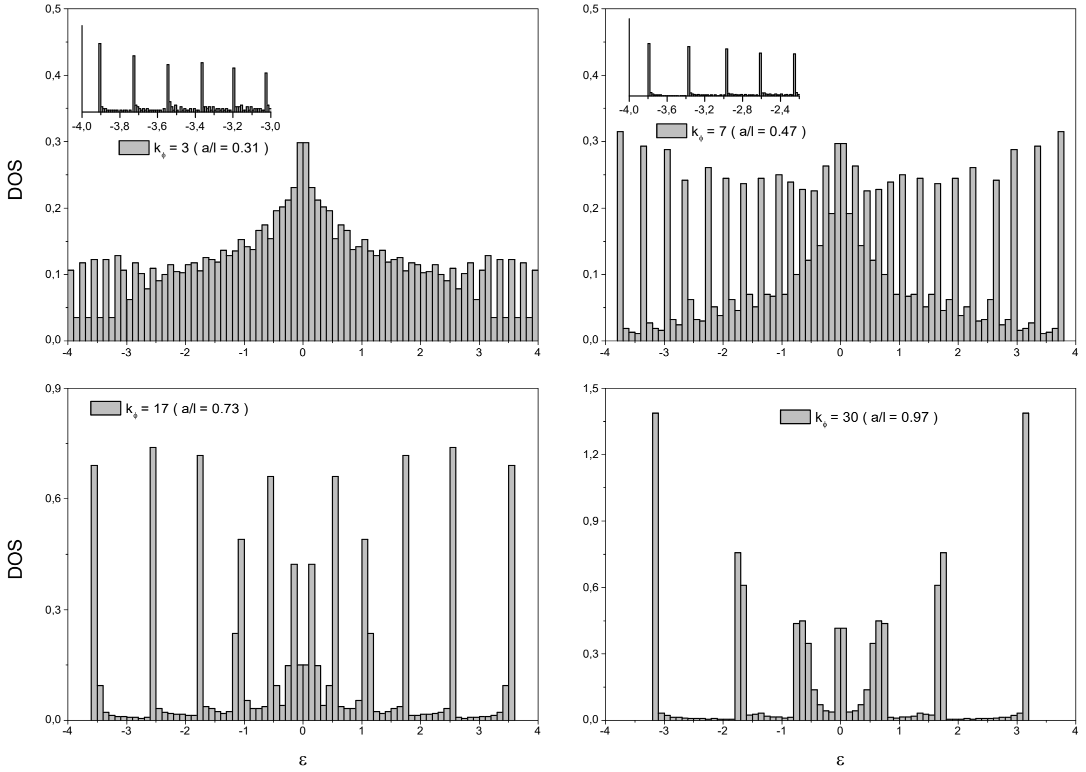

Figure 2.4: Square lattice tight binding DOS for 4 values of $k_{\Delta\phi}$.

$k_\phi = 3$, $a/\ell = 0.31$, beginning of (2)

Near the band edges are emerging sharp peaks, LLs, with spacing $\gtrapprox 2\Delta\varepsilon = 0.2$. This is the first magnetic field induced contribution to the base value of $\mathcal{D}_{[0.1]}$ due to the slowly varying profile of the original DOS.

Receding from the band edge, the small degeneracy of the newly formed Landau levels is further decreasing, until it disappears into the bulk of the original broad DOS peak.

$k_\phi = 7$, $a/\ell = 0.47$, second half of (2)

Discretization progresses further from the band edge, cutting into central DOS peak, and more than half of all eigenvalues are contained within well-separated LL. The spacing between distinct LL is highest near the band edges (≈ 0.4) and small ($\gtrapprox 0.2$) near the center.

$k_\phi = 17$, $a/\ell = 0.73$, middle part of (3)

The density of sates consists of well-formed LLs with only small remnants of the original DOS in the middle of the band. Change in magnetic field and ϕ have only marginal effect on $\mathcal{D}_{[0.1]}$ as the two competing scales become relevant and the interplay of two different effects leaves the discretization metric mostly unchanging.

On the one hand, increasing the magnetic field would lead to separation of the non-discretized remainder in the center. On the other hand, increasing the field leads to a reduction in the total number of LLs, and the remaining ones (especially near the center of the band) tend to be broad with respect to spacing $\Delta\varepsilon$, lowering $\mathcal{D}_{[0.1]}$ instead.

$k_\phi = 30$, $a/\ell = 0.97$, within (4)

No hint of the original DOS profile is present, all eigenvalues are contained within well-separated but broad LLs. Increasing the magnetic field leads only to fewer and broader LLs, resulting in a further decrease of $\mathcal{D}_{[0.1]}$

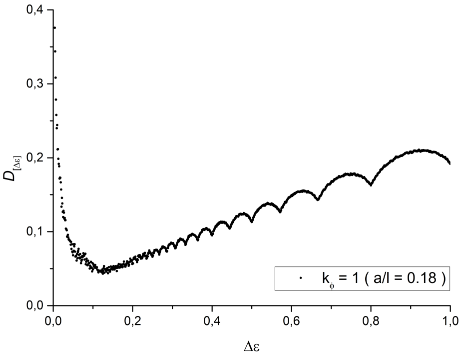

Figure 2.5: Square lattice tight binding $\mathcal{D}_{[\Delta\varepsilon]}$ for $a/\ell \approx 0.18$.

Bin spacing analysis

The discretization metric can be used as a simple peak frequency and weight analysis tool when evaluated for given $\sigma\left(\mathbf{H}^\phi\right)$ for various spacings $\Delta\varepsilon$.

The subsequent set of figures 2.5, 2.6 and 2.7 corresponding to $k_{\Delta\varepsilon} = 1$, 3 and 17 respectively depicts this dependency on the interval $\Delta\varepsilon \in \langle 0, 1\rangle$.

At first in low fields $k_{\Delta\varepsilon} = 1$ is the weight of the forming LLs too small to be captured by the discretization metric, as for low $\Delta\varepsilon$ there is apparent only the common $\mathcal{D}_{[\Delta\varepsilon]} \to 1$ limit.

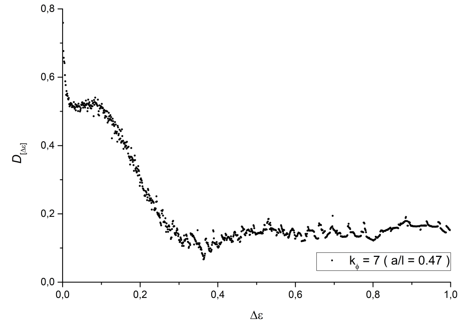

Figure 2.6: Square lattice tight binding $\mathcal{D}_{[\Delta\varepsilon]}$ for $a/\ell \approx 0.47$.

Following that, the case of $k_{\Delta\varepsilon} = 7$ shows clear and prominent jump in that region, which corresponds to the peak spacing frequency observable in 2.4.

Lastly, the $k_{\Delta\varepsilon} = 17$ case reveals a less sharp and very broad peak originating from the fact that to the $\mathcal{D}_{[\Delta\varepsilon]}$ now contribute significantly both region near the band edge with hight inter-LL spacing as well as the middle of the band, with spacing significantly lower.

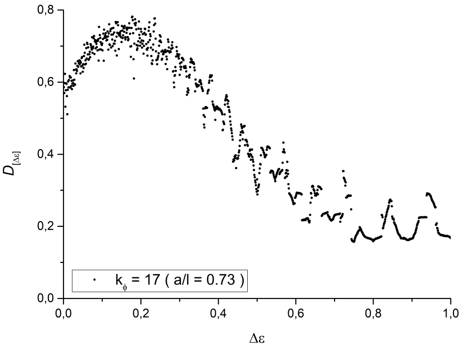

Figure 2.7: Square lattice tight binding $\mathcal{D}_{[\Delta\varepsilon]}$ for $a/\ell \approx 0.73$.

2.2 Models of realistic materials - Outlook

Starting from the analysis of simple 2D lattice model, it is in principle straightforward to extend to more complex lattices for description of realistic bulk materials, with simple alkali metals, and specifically bcc lithium being the prime example.

Lithium tight-binding model would treat electron 1s states as core levels and hence the effect of magnetic field on these states is to be ignored and remaining single electron per atom in 2s states could be treated in direct analogy to the square lattice model described earlier.

Introduction of low magnetic fields leads to the formation of the DOS modulation in the vicinity of the parabolic band edge. If in turn the energy is fixed the DOS will be oscillating function of the magnetic field giving rise to the Shubnikov-de Haas oscillations. Of particular interest would be then yet higher (quantizing) fields, when $\hbar\omega_c$ becomes comparable with the band width, and the form the electronic structure takes in such case.

Three dimensional nature of the problem prevents formation of fully separated LLs typical for the 2D models and as such no structure akin to the Hofstadter butterfly 2.1 is expected to be seen. Consequently no true quantization of conductivity will arise. Nevertheless if DOS in quantizing magnetic fields can be determined, magnetotransport properties beyond the usual scope of band structure formalism can be accessed.

Note that quantizing fields 2.3 are of order of hundreds of Tesla and experimentally hardly accessible. Whether interesting magnetotransport effects in moderate magnetic fields can occur in certain materials remains to be explored in future research.

3. Fractional Quantum Hall Effect

In the core of FQHE physics lies the question for which values of the filling factor ν there is an incompressible, gaped, ground state and what its form is. The following text approaches this question from an analytical point of view via Single mode approximation.

Section Direct SMA presents the SMA in its original form, as developed for the study of superfluid ^{4}He and its assumptions, motivation, and derivation are discussed. Direct SMA is applied to the QHE case of polarized 2 dimensional electron gas and its failure to provide meaningful information about the intra-LL excitation spectrum is examined in detail.

The necessary adjustment of the direct SMA for the FQHE, the projection of the present operators and expressions to the LLL, is the subject of the section Projected SMA. The final derived dispersion relation of the so-called magnetoroton branch is used in the subsection SMA applied to $\nu = 1/3$ problems to clarify the origin of the flat magnetoroton dispersion in hight k present in numerical calculations and efforts to apply SMA to the special WYQ ground state are discussed.

Notation

Both classical vector notation and complex notation

$$\begin{aligned} \mathbf{r} = (x, y) \quad &\leftrightarrow \quad z = x + iy, \\ \mathbf{k} = (k_x, k_y) \quad &\leftrightarrow \quad \tilde{k} = k_x - ik_y. \end{aligned} \tag{3.1}$$

is used in the following. It should be clear, where is which notation utilized as they are never used in any expression simultaneously.

3.1 Direct SMA

Assuming that ground state ϕ, which is liquid and therefore also has a homogeneous density, is known. Generally one would expect that in the case of nonzero inter-particle interaction, when degrees of freedom associated with particle positions are not completely lost due to the Pauli exclusion principle, that the low lying excitation spectrum will include density waves.

Of special interest are then systems where due to special circumstances there are no low lying single-particle excitations, leaving excited state wave function of the form of density modulation as a good variational wave function candidate.

Such was the case of superfluid ^{4}He for whose purposes SMA was originally developed by Feynman[26]. Here is of main interest 2D electron gas in magnetic field so that low-lying single particle excitation spectrum normally originating from small kinetic energy of excitations over Fermi surface is quenched into highly degenerate discrete LL.

The variational wave function which directly incorporates the ground state ϕ may preserve most of its favorable correlations and properties. SMA proposes a wave function of the form[27]

$$\phi_{\mathbf{k}(\mathbf{r_1},\ldots,\mathbf{r_n})} = N^{-1/2}\rho_{\mathbf{k}}\phi(\mathbf{r_1},\ldots,\mathbf{r_n}) \tag{3.2}$$

where $\rho_{\mathbf{k}}$ is Fourier transform of the density

$$\rho(\mathbf{R}) = \sum_{j=1}^{N}\delta^2(\mathbf{R}-\mathbf{r}_j), \quad \rho_{\mathbf{k}} = \int d\mathbf{R}^2 e^{-i\mathbf{k}.\mathbf{R}}\rho(\mathbf{R}) = \sum_{j=1}^{N} e^{-i\mathbf{k}.\mathbf{r}_j}. \tag{3.3}$$

This wave function (3.2) is for nonzero $\mathbf{k}$ orthogonal to the ground state ϕ while preserving homogeneous density distribution. This can be seen by using the general picture of two systems with the same density wave modulation (the same $\mathbf{k}$), but shifted with respect to each other, thus leading to different phase contributing in $\rho_{\mathbf{k}}$ (used translational invariance of the ground state). This phase factor does not change the probability $|\phi_{\mathbf{k}}|^2$ of such concrete realization of excited state $\phi_{\mathbf{k}}$ happening, leaving both of them equally likely to occur and therefore leaving the mean density of $\phi_{\mathbf{k}}$ uniform.

Using this wave function leads to variational excitation energy gap estimate

$$\Delta(k) = \frac{f(k)}{s(k)}, \tag{3.4}$$

where $s(k)$ denotes static structure factor, obtained from normalization of $\phi_{\mathbf{k}}$ as

$$s(k) = \langle \phi_{\mathbf{k}} \,|\, \phi_{\mathbf{k}} \rangle = N^{-1}\left\langle \phi \,\middle|\, \rho^{\dagger}_{\mathbf{k}}\rho_{\mathbf{k}} \,\middle|\, \phi \right\rangle, \tag{3.5}$$

and $f(k)$, the so called oscillator strength, is given by

$$f(k) = N^{-1}\langle \phi_{\mathbf{k}} \,|\, \mathcal{H} - E_0 \,|\, \phi_{\mathbf{k}} \rangle = N^{-1}\left\langle \phi \,\middle|\, \rho^{\dagger}_{\mathbf{k}}\,[\mathcal{H},\rho_{\mathbf{k}}] \,\middle|\, \phi \right\rangle. \tag{3.6}$$

Note that $f(k)$ stands as a right hand side of the Bethe oscillator strength sum rule [28] (with $|l\rangle$ being energy eigenstate with E_l)

$$\sum_l (E_l - E_0)N^{-1}\left|\langle \phi \,|\, \rho_{\mathbf{k}} \,|\, l \rangle\right|^2 = N^{-1}\left\langle \phi \,\middle|\, \rho^{\dagger}_{\mathbf{k}}\,[\mathcal{H},\rho_{\mathbf{k}}] \,\middle|\, \phi \right\rangle = f(k) \tag{3.7}$$

where right hand side may be due to the form of $\rho_{\mathbf{k}}$, which is given by function of position operators, rewritten as

$$f(k) = \frac{1}{2N}\left\langle \phi \,\middle|\, \left[\rho^{\dagger}_{\mathbf{k}},[\mathcal{H},\rho_{\mathbf{k}}]\right] \,\middle|\, \phi \right\rangle \overset{*}{=} \frac{\hbar^2}{2mN}\left\langle \phi \,\middle|\, \nabla\rho_{\mathbf{k}}\cdot\nabla\rho^{\dagger}_{\mathbf{k}} \,\middle|\, \phi \right\rangle = \frac{\hbar^2 k^2}{2m}. \tag{3.8}$$

The second part is only true within the current framework, where the interaction term $\mathcal{V}$ in the Hamiltonian $\mathcal{H}$ commutes with the density operator $\rho_{\mathbf{k}}$.

Yet another way to view $\Delta(k)$ is to rewrite its constituents using dynamic structure factor

$$S(k,\omega) = N^{-1}\sum_n \left\langle \phi \,\middle|\, \rho^{\dagger}_{\mathbf{k}} \,\middle|\, n \right\rangle \delta(\omega - E_n + E_0)\,\langle n \,|\, \rho_{\mathbf{k}} \,|\, \phi \rangle,$$

yielding

$$s(k) = \int_0^\infty d\omega S(k,\omega), \quad f(k) = \int_0^\infty d\omega\omega S(k,\omega).$$

From the rewritten form of the oscillator strength, it can be seen that $\Delta(k)$ is the exact first moment (mean value) of the energy of the excitation spectrum coupled with the ground state through the density operator $\rho_{\mathbf{k}}$. This statement is consistent with Δ being the variational upper bound for the minimum collective, density wave, mode energy. Also, note that saturation of the sum rule (3.7) with a single mode is equivalent to the statement that the variational wave function $\phi_{\mathbf{k}}$ corresponds to the energy eigenstate. In that case, the mean value of the excitation spectrum becomes the exact excitation energy between the ground state and this eigenstate.

In this sense, assumption that $\phi_{\mathbf{k}}$ is a good variational wave function is that the density wave $\phi_{\mathbf{k}}$ saturates the oscillator strength sum rule, leaving the acquired dispersion (3.4) exact. Note that in that case also the dynamical structure factor, which may be used to determine other properties of the system e.g. via susceptibility, is easily accessible as

$$S(k,\omega) = s(k)\delta(\omega - \Delta(k)).$$

Full saturation of the oscillator sum rule by single mode is not even remotely common and within QHE it will be shown that it actually holds only within the long wavelength limit. Still, in many cases most of the oscillator strength may be absorbed by single mode [29] and *single mode approximation* then, as one would expect, lies in the assumption that sum rule is fully saturated by single excitation mode.

g-functions and constraints

Static structure factor appearing within SMA framework can be obtained as Fourier transform of g function (particle pair radial distribution function) $g(\mathbf{r})$ of given system as [30]

$$s(\mathbf{k}) = 1 + \rho \int d^2\mathbf{R} e^{-i\mathbf{k}.\mathbf{R}} \left(g(\mathbf{R}) - 1\right) + \rho 2\pi\delta^2(\mathbf{k}), \tag{3.9}$$

where $\rho = \nu/2\pi\ell^2$ and in general $\nu = 1/M$. Specially for isotropic g function $g(\mathbf{r}) \to g(r)$ is static structure factor also isotropic and given by Hankel transform $\mathcal{F}_H$ of the form

$$\begin{aligned} s(k) &= 1 + 2\pi\rho \int_0^\infty dr J_0(kr) \left(g(r) - 1\right) + \rho 2\pi\delta(k) \\ &= 1 + \rho \int_0^\infty dr \int_{-\pi}^{\pi} e^{ikr\sin(\phi)} \left(g(r) - 1\right) + \rho 2\pi\delta(k), \end{aligned}$$

where J_0 denotes the Bessel function of the first kind.

Taking $\nu = 1$ (IQHE case) results in the well-known exact wave function with polynomial factor given by the determinant of Vandermonde matrix and the corresponding g function may be directly calculated[31]

$$g_{\nu=1}(r) = 1 - e^{-r^2/2\ell^2} \quad \longrightarrow \quad s_{\nu=1}(k) = 1 - e^{-k^2\ell^2/2}. \tag{3.10}$$

In the case of FQHE with ν given by simple fraction does usually Laughlin wave function Ψ_L describe ground state well [29]. For g function $g(r)$ then can be used formula derived assuming Laughlin ground state[14] (summation over odd values of m only)

$$g(r) = 1 - e^{-r^2/2\ell^2} + \sum_{m=1'}^{\infty} \frac{2}{m}\left(\frac{r^2}{4\ell^2}\right)^m c_m e^{-r^2/2\ell^2}. \tag{3.11}$$

Note that[32]

$$\mathcal{F}_H\left[e^{-x^2/2}\right](y) = e^{-y^2}, \text{ and } \mathcal{F}_H\left[x^m e^{-x^2/2}\right](y) = y^{1/2}\left(\frac{d}{ydy}\right)^m\left[y^{m-1/2}e^{-y^2/2}\right],$$

and therefore g functions of the form (3.11) have easily accessible analytical Hankel transform, which makes them also very suitable for SMA energy gap calculations.

This general form (3.11) is further restricted due to various conditions originating from the ground state wave function used. First constraint is given by known short-range behavior, which should be $\propto r^{-2M}$ due to the $(z_i - z_j)^M$ term in the Laughlin wave function. For this condition to hold, c_1 must be equal to -1.

$$g(r) = 1 - e^{-r^2/2\ell^2} - 2r^2 e^{-r^2/4\ell^2} + \sum_{m=3'}^{\infty} \frac{2}{m}\left(\frac{r^2}{4\ell^2}\right)^m c_m e^{-r^2/2\ell^2}. \tag{3.12}$$

Next three conditions (denoted as $\{\mathbf{n}, \mathbf{s}, \mathbf{c}\}$ for charge neutrality, perfect screening and compressibility sum rules respectively) are derived from classical 2D plasma analogy of Laughlin state[14]

$$\text{charge neutrality } (\mathbf{n}) \sum_{m=1}^{\infty} c_m = \frac{1-M}{4} \tag{3.13}$$

$$\text{perfect screening } (\mathbf{s}) \sum_{m=1}^{\infty} (m+1)c_m = \frac{(1-M)}{8} \tag{3.14}$$

$$\text{compressibility } (\mathbf{c}) \sum_{m=1}^{\infty} (m+2)(m+1)c_m = \frac{(1-M)^2}{8}. \tag{3.15}$$

In [29] it is shown that the Laughlin state charge neutrality condition corresponds to the conservation of the total number of particles and the perfect screening to the conservation of the total angular momentum. Provided that particle number and total angular momentum are constants of motion values of the first two terms are set for any reasonable liquid ground state.

As there is no closed-form expression for the RDF of Ψ_L, in the following is g_L used to denote the RDF obtained by fitting 13 terms of expansion (3.12) to Monte Carlo data (more on the method and results [27]). As it is an approximation of the full Laughlin RDF it fulfils all of conditions above.

By direct expansion it can be shown that the charge neutrality (3.13) condition fixes the first constant term of structure factor (3.9) in long wavelength expansion (Taylor expansion of $s(k)$ around $k = 0$). Similarly, the perfect screening condition (3.14) sets the numerical prefactor of k^2 term and the compressibility sum rule (3.15) third k^4 term. Thus these tree conditions straightforwardly correspond to conditions on values of the first three terms of $s(k)$ expansion.

$$s_\nu(k) \approx 0 + \frac{1}{2}(k\ell)^2 + \frac{1-2\nu}{8\nu}(k\ell)^4 + \ldots \Longrightarrow s_{\nu=1/3}(k) \approx \frac{1}{2}(k\ell)^2 + \frac{1}{8}(k\ell)^4 + \ldots$$

First two coefficients in the long wavelength expansion are also related to properties of general liquid ground state.

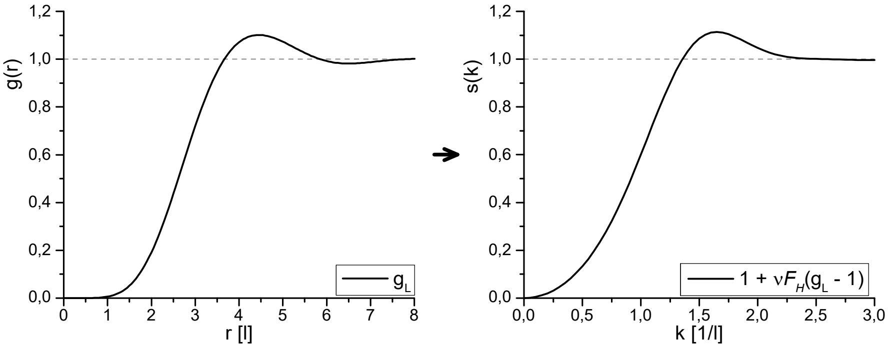

Figure 3.1: Laughlin-like g function g_L and its Hankel transform derived static structure factor.

Also note that condition $s(k) \to 0$ as k approaches 0 is via compressibility equation[30] (χ_T denoting isothermal compressibility)

$$\lim_{k\to 0} s(k) = \rho k_B T \chi_T$$

statement about (macroscopic) incompressibility of given system. As will be seen below, this condition is in SMA (both direct and projected) necessary condition for the existence of the energy gap at $k = 0$.

Direct SMA results

Used in this direct form, the excitation gap energy $\Delta(k)$ (3.4) is due to the commutation of the position and density operator $\rho_{\mathbf{k}}$ independent of the interaction part of the Hamiltonian. SMA then yields (using commutation relations of kinetic momenta π and position $\mathbf{r}$ and relation $\hbar^2/(\ell^2 m) = \hbar\omega_c$)

$$\Delta(k) = \frac{\hbar\omega_c}{2}\frac{k^2\ell^2}{s(k)}. \tag{3.16}$$

The only nontrivial part is then the filling factor ν dependent structure factor $s(k)$. Notably, the resulting SMA energy gap is not dependent on the form of interaction as it does not affect achieved result.

In the $\nu = 1$ case, employing its known g function and static structure factor (3.10), one has

$$\Delta(k) = \frac{\hbar\omega_c}{2}\frac{k^2\ell^2}{1-\exp\{-k^2\ell^2/2\}}, \text{ and } \Delta(k) \to \hbar\omega_c \text{ as } k \to 0, \tag{3.17}$$

thus obtaining cyclotron excitation energy $\hbar\omega_c$ in the long wavelength limit.

The origin of this behavior can be traced to the Pauli exclusion principle, which within fully filled LL completely removes degrees of freedom associated with particle position, with lowest possible excitations involving excitations of particles into higher LLs, thus leading to arisal of cyclotron energy in SMA.

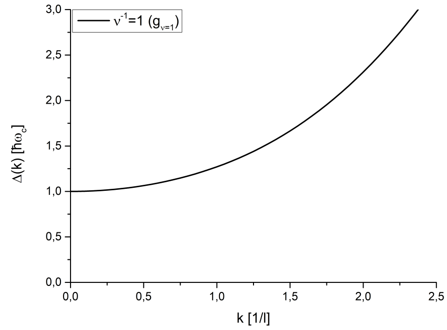

Figure 3.2: SMA excitation gap $\Delta(k)$ dependence. Case of $\nu = 1$ with corresponding $g_{\nu=1}$.

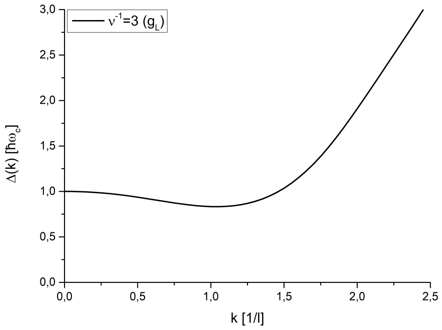

Figure 3.3: SMA excitation gap $\Delta(k)$ dependence. Case of $\nu = 1/3$ with corresponding g_L.

Further study of long wavelength asymptotic behaviour of Laughlin like states in the SMA shows, employing known long wavelength behaviour of general ν ground state static structure factor

$$s(k) = \frac{1}{2}(k\ell)^2 + o(k^4),$$

that limit in (3.17) hold more in general independently on ν.

Note that even with fractional ν, when the Pauli principle no longer excludes low lying intra-LL excitations as in the integer case, SMA still yields cyclotron excitation energy $\hbar\omega_c$ in the long wavelength limit. This can be explicitly seen in the case $\nu = 1/3$ using g_L in the figure 3.3.

Cyclotron mode and saturation of the sum rule

To explain this result, following Kohn[33], writing total kinetic momentum operator

$$\Pi = \sum_i^N \pi_i \quad \text{for which} \quad [\mathcal{H}, \Pi] = i\frac{\hbar e}{m}\Pi \times B,$$

allows to define ladder operator Π_+.

$$\Pi_+ = \Pi_x + i\Pi_y \quad \text{with} \quad [\mathcal{H}, \Pi_+] = \hbar\omega_c \Pi_+.$$

Therefore, for ground state $|\phi\rangle$ there is excited cyclotron eigenstate $\Pi_+ |\phi\rangle$ with energy $E_0 + \hbar\omega_c$. In the long wavelength limit $k \to 0$ associated cyclotron mode saturates SMA Bethe oscillator sum rule (3.7) with its right hand side (3.8)

$$\sum_l (E_l - E_0) N^{-1} |\langle \phi \,|\, \rho_{\mathbf{k}} \,|\, l \rangle|^2 = f(k) = \frac{\hbar^2 k^2}{2m}, \tag{3.18}$$

resulting in exact cyclotron energy $\Delta(0) = \hbar\omega_c$.

To see that it is true, one may recall that it is possible to choose CMS coordinates with one center-of-mass coordinate and as rest take some combination of relative coordinates to describe the system. Such choice leads to separation of the center-of-mass part of the Hamiltonian, which then corresponds to a one-particle Hamiltonian with free-particle spectrum.

This decoupling allows one to reduce this many-body problem to effectively 1-body problem. Clearly, the introduced operator Π is then proportional to the center-of-mass momentum operator, and it can be seen that Π_+ is proportional to the LL ladder operator, employing 1-body ladder operator algebra as defined in [34]

$$\Pi_+ \propto a^\dagger = \frac{\ell}{\sqrt{2}\hbar}\left(\pi_x + i\pi_y\right). \tag{3.19}$$

On the other hand, expanding density operator $\rho_{\mathbf{k}}$ and introducing center of mass coordinate $\mathbf{R}$ leads to

$$\rho_{\mathbf{k}} \overset{k\to 0}{\approx} 1 - i\mathbf{k}\cdot\sum_i \mathbf{r}_j = 1 - iN\mathbf{k}\cdot\mathbf{R} = 1 - \frac{iN\ell}{\sqrt{2}}\left(\tilde{k}(b + a^\dagger) + k(b^\dagger + a)\right),$$

where last relation is obtained using both 1-body LL quantum number ladder operators a, $a^\dagger$ and angular momentum quantum number ladder operators b, $b^\dagger$. Plugging obtained formula back into (3.18) yield, owing to orthogonality of energy eigenstates $\langle \phi \,|\, l \rangle = 0$

$$\sum_l (E_l - E_0) N\ell |\left\langle \phi \,|\, \mathbf{k}\cdot\mathbf{R} \,|\, l \right\rangle|^2 \propto \sum_l (E_l - E_0) N |\left\langle \phi \,\middle|\, \tilde{k}(b + a^\dagger) + k(b^\dagger + a) \,\middle|\, l \right\rangle|^2.$$

Next, one needs to take into account that $a^\dagger$ annihilates ground state $\langle\phi|$ and that due to the free particle spectrum of center of mass part of the wave function operators b, $b^\dagger$ do not change its energy leaving possible transition with $(E_l - E_0) = 0$ (or even more strongly in case of fully filled LL, b and $b^\dagger$ also necessary annihilate ground state due to Pauli exclusion principle).

Thus in the sum rule contributes in the lowest order of the long wavelength expansion only a part, which by (3.19) corresponds to the cyclotron energy eigenstate. Note that this contribution is proportional to k^2, with other modes vanishing with k^4 or faster, as is the right hand side of (3.18) and therefore cyclotron mode with its excitation energy $\hbar\omega_c$ saturates oscillator sum rule in long wavelength limit.

This result is in accordance with the general idea that in asymptotically long wavelengths external perturbation couples only to the CMS degree of freedom, whose energy spectrum is wholly independent of inter-particle interaction. In quantum Hall regime this coupling manifests itself with saturation of the sum rule by inter-LL excitation of the center-of-mass wave part of the wave function.

SMA of this form thus tells nothing about low-lying collective modes. To obtain a better estimate for the energy of intra-LLL excitations corresponding to collective density waves, one needs to use a modified variational wave function such that it does not have any weight in higher LL.

3.2 Projected SMA

Analytical structure of the LLL wavefunction can be effectively used to find the projection of the variational wave function $\phi_{\mathbf{k}}$ (3.2), density operator $\rho_{\mathbf{k}}$ (3.3) and the resulting SMA excitation energy gap (3.4).

LLL wave functions, when written using complex coordinate notation, are all of the form

$$\phi_\alpha(z_1,\ldots) = f_\alpha[z_1,\ldots]e^{-\frac{1}{4\ell^2}\sum_i z_i\bar{z}_i},$$

where f_α is analytical function of complex coordinates z_i. Thanks to this specific structure, all LLL states can be described as functions from Hilbert space of analytical function of complex coordinates $\Theta = \{f_\alpha\}_\alpha$ with Gaussian measure $d\mu[z]$ to absorb common exponential term

$$d\mu[z] = \prod_i^N \frac{1}{2\pi} e^{-\frac{1}{2\ell^2}z_i\bar{z}_i}dz_i$$

and appropriate inner product

$$(f_\alpha, f_\beta) = \int d\mu[z] f_\alpha[z]^* f_\beta[z], \quad (f_\alpha, f_\beta) < \infty \quad \forall\alpha\beta.$$

Hermitian conjugate (denoted with $*$) now takes these functions out of this Hilbert space Θ, because z^* is not an analytical function of z. On the other hand, the adjoint operator of z with respect to inner product is now $z^\dagger = 2\partial_z$.

Operators $z^\dagger$ and z^* have the same matrix elements within LLL [35], and therefore $z^\dagger$ is sought projection of z^* (whilst z is already analytical and thus lies entirely within LLL). Unlike pair z, z^*, operators z and $z^\dagger$ do not commute. This introduces ambiguity in the ordering of the operators, which has to be resolved by condition

$$\langle \phi_\alpha \,|\, \phi_\beta \rangle = (f_\alpha, f_\beta) \quad \forall\alpha\beta,$$

i.e. by preservation of the original full Hilbert space inner product. As a result, the correct ordering is such that all derivatives (adjoints) $z^\dagger$ are to the left with respect to the position operators z.

Within SMA is of major importance density operator, whose projection has the form (taking into account ordering)

$$\overline{\rho}_{\mathbf{k}} = \sum_{j=1}^N e^{-\frac{i\tilde{k}}{2}z_j^\dagger} e^{-\frac{i\tilde{k}^*}{2}z_j} = \sum_{j=1}^N e^{-i\tilde{k}\partial_{z_j}} e^{-\frac{i\tilde{k}^*}{2}z_j}, \quad \overline{\rho}_{\mathbf{k}}^\dagger = \overline{\rho}_{-\mathbf{k}}.$$

Due to the kinetic energy being quenched by magnetic field and staying constant within LLL, only surviving term in Hamiltonian is electrostatic interaction for which is

$$\mathcal{V} = \frac{1}{2}\int \frac{d^2q\ell}{(2\pi)^2} v(q) \sum_{i<j} e^{i\mathbf{q}\cdot(\mathbf{r_i}-\mathbf{r_j})} \quad \longrightarrow \quad \overline{\mathcal{V}} = \frac{1}{2}\int \frac{d^2q\ell}{(2\pi)^2} v(q) \left(\overline{\rho}_{\mathbf{q}}^\dagger \overline{\rho}_{\mathbf{q}} - Ne^{-\frac{q^2\ell^2}{2}}\right), \tag{3.20}$$

due definition of $\tilde{q}$ in (3.1) and

$$\begin{aligned}\sum_{i<j} e^{i\mathbf{q}.(\mathbf{r_i}-\mathbf{r_j})} \quad \longrightarrow \quad & \sum_{i<j} e^{\frac{i\tilde{q}}{2}(z_i-z_j)^\dagger} e^{\frac{iq^*}{2}(z_i-z_j)} = \\ &= \sum_{i,j} e^{\frac{i\tilde{q}}{2}z_i^\dagger} e^{\frac{i\tilde{q}^*}{2}z_i} e^{-\frac{i\tilde{q}}{2}z_j^\dagger} e^{-\frac{i\tilde{q}^*}{2}z_j} - \sum_k e^{\frac{i\tilde{q}}{2}z_k^\dagger} e^{\frac{i\tilde{q}^*}{2}z_k} e^{-\frac{i\tilde{q}}{2}z_k^\dagger} e^{-\frac{i\tilde{q}^*}{2}z_k} \\ &= \overline{\rho}_{\mathbf{q}}^\dagger \overline{\rho}_{\mathbf{q}} - Ne^{-\frac{q^2\ell^2}{2}},\end{aligned}$$

where was used BCH formula with the following commutation relation

$$\begin{gathered}\left[\frac{i\tilde{q}^*}{2}z_k, \frac{-i\tilde{q}}{2}z_k^\dagger\right] = \frac{(q\ell)^2}{4}\left[z_k, z_k^\dagger\right] = -\frac{(q\ell)^2}{2}, \\ [X,Y] = C \text{ (c-number) } \Rightarrow e^X e^Y = e^Y e^X e^C.\end{gathered}$$

In similar fashion one can derive auxiliary expressions

$$\left[\overline{\rho}_{\mathbf{k}}, \overline{\rho}_{\mathbf{q}}\right] = \left(e^{\frac{\tilde{k}^*\tilde{q}\ell^2}{2}} - e^{\frac{\tilde{k}\tilde{q}^*\ell^2}{2}}\right)\overline{\rho}_{\mathbf{k+q}}, \tag{3.21}$$

$$\overline{\rho_{\mathbf{q}}^\dagger \rho_{\mathbf{q}}} = \overline{\rho}_{\mathbf{q}}^\dagger \overline{\rho}_{\mathbf{q}} + N\left(1 - e^{-\frac{q^2\ell^2}{2}}\right), \tag{3.22}$$

first of which is repeatedly used when evaluating oscillator strength term projection $\overline{f}(k)$ (3.6) and second needed for rewriting resulting mean values, or projected structure factor terms $\overline{s}(k)$, to known (unprojected) $s(k)$ (3.5)

$$\overline{s}(k) = \left\langle \phi \middle| \overline{\rho}_{\mathbf{k}}^\dagger \overline{\rho}_{\mathbf{k}} \middle| \phi \right\rangle \longrightarrow s(k) = \left\langle \phi \middle| \rho_{\mathbf{k}}^\dagger \rho_{\mathbf{k}} \middle| \phi \right\rangle = \left\langle \phi \middle| \overline{\rho_{\mathbf{k}}^\dagger \rho_{\mathbf{k}}} \middle| \phi \right\rangle.$$

Final relation

Using previously derived auxiliary expressions (3.21), (3.22) and interaction potential projection (3.20) one derives SMA energy gap expression (corresponding to equation (4.15) in the original article [27]):

$$\begin{aligned}\Delta(k) &= \frac{\overline{f}(k)}{\overline{s}(k)}, \quad \overline{s}(k) = s(k) - (1 - e^{-k^2\ell^2/2}) \qquad (3.23) \\ \overline{f}(k) &= \frac{1}{2}\sum_{\mathbf{q}} v(q)\left(e^{\tilde{q}^*\tilde{k}\ell^2/2} - e^{\tilde{q}\tilde{k}^*\ell^2/2}\right) \quad \times \\ \times \quad & \left[\overline{s}(q)e^{-k^2\ell^2/2}\left(e^{-\tilde{k}^*\tilde{q}\ell^2/2} - e^{-\tilde{k}\tilde{q}^*\ell^2/2}\right) + \overline{s}(\mathbf{k}+\mathbf{q})\left(e^{\tilde{k}^*\tilde{q}\ell^2/2} - e^{\tilde{k}\tilde{q}^*\ell^2/2}\right)\right].\end{aligned}$$

For practical use, reciprocal complex vectors in $\overline{f}(k)$ need to be rewritten into standard vector form instead of their complex analogues with

$$\begin{aligned}\tilde{q}^*\tilde{k} &= (q_x + iq_y)(k_x - ik_y) = (q_x k_x + q_y k_y) + i(q_x k_y - q_y k_x) \\ &= \mathbf{q}.\mathbf{k} + i\mathbf{q}\times\mathbf{k}|_z,\end{aligned}$$

$$\left(e^{\tilde{q}^*\tilde{k}\ell^2/2} - e^{\tilde{q}\tilde{k}^*\ell^2/2}\right) = 2i\sin\left(\mathbf{q}\times\mathbf{k}|_z\ell^2\right)e^{\mathbf{q}.\mathbf{k}\ell^2/2}.$$

Using these identities allows to write (3.23) in concise form

$$\Delta(k) = \frac{1}{s(k) - 1 + e^{-k^2/2}} \quad \times \tag{3.24}$$
$$\times \quad \int \frac{d^2q}{(2\pi)^2} v(q) \left(1 - \cos\left(\mathbf{q} \times \mathbf{k}|_z\right)\right) \left[e^{\mathbf{q}.\mathbf{k}} \left\{s(\mathbf{q}+\mathbf{k}) - 1\right\} - e^{-k^2/2} \left\{s(\mathbf{q}) - 1\right\}\right].$$

The energy gap in SMA is then fully determined by the static structure factor $s(k)$ and the choice of potential $v(q)$.

General behaviour and properties

Direct expansion of projected oscillator strength in (3.23) shows that

$$\overline{f}(k) \propto k^4 + o(k^6) \text{ as } k \to 0.$$

This is to be expected as k^2 asymptotic behaviour of original $f(k)$ is wholly saturated by cyclotron mode. By projection to the LLL, the inter-LL modes were removed leaving faster diminishing intra-LLL contributions.

The condition for excitation gap emergence in the long wavelength limit of projected SMA is then $\overline{s}(k) \propto k^4$ for small k.

Recalling discussion of asymptotic behavior of Laughlin-like liquid state static structure factor one has that within LLL projected SMA is particle number and total angular momentum preservation (condition (3.13) and (3.14) respectively, fixing two lowest orders of long wavelength expansion) sufficient condition for gap emergence. Specially in case of Laughlin wave function (fulfilling constraint (3.15)) is

$$\overline{s}_\nu(k) \approx \frac{1-\nu}{8\nu}(kl)^4 + \ldots \quad \Longrightarrow \quad \overline{s}_{\nu=1/3}(k) \approx \frac{1}{4}(kl)^4 + \ldots.$$

Previously discussed case $\nu = 1$ has by comparison of its structure factor (3.10) and projection (3.23) $\overline{s}(k) = 0$. This has to be understood as

$$\overline{\rho}_\mathbf{k} \left|\phi_{\nu=1}\right\rangle = 0 \quad \longrightarrow \quad \overline{s}_{\nu=1}(k) = 0,$$

i.e. statement about vanishing of intra-LL density waves in fully filled LL due to the Pauli exclusion principle.

While energy scale of direct SMA (3.16), (figures 3.2, 3.3) was set by dominant cyclotron mode, in the projected SMA its scale is given entirely by interaction potential $v(q)$ in (3.24).

This can be traced back to the fact that in the direct SMA case the position-dependent interaction potential commutes with the density operator $\rho_\mathbf{k}$ with only contribution originating from commutator with kinetic energy part of the Hamiltonian, which is responsible for the LL quantization and therefore also for the cyclotron mode. By projection to the LLL the kinetic energy part becomes trivial constant and previously commuting interaction potential now fails to commute with $\overline{\rho}_\mathbf{k}$ due to the non-trivial behavior of z and $z^\dagger$ operators.

Interaction potential

The interaction potential $v(q)$ is the second and last input required for the calculation of the projected energy gap of SMA (3.24). In case of exact 2D Coulomb interaction this potential is of the well known form

$$v(q) = k\frac{2\pi}{q}.$$

In the context of FQHE are also commonly used the so called Haldane pseudopotentials V_m, i.e. the relative angular momentum representation of the interaction $\mathcal{V}$.

For example full Coulomb interaction in terms of pseudopotentials leads to

$$V_m = \frac{e^2 k}{\ell}\frac{\Gamma\left(m+\frac{1}{2}\right)}{2\Gamma\left(m+1\right)}.$$

Since relative angular momentum quantum numbers are related to the relative interparticle distance, with increasing m corresponding to larger distances, one may define the 'cropped' Coulomb potential V_k^{cr} as consisting of exact Coulomb pseudopotentials V_m for $m \leq k$ and rest zero.

$$V_k^{cr}: \quad V_m = \begin{cases} V_m^{Coulomb} & m \leq k \\ 0 & m > k \end{cases}$$

Haldane pseudopotentials can be also used for the definition of new typically short-range interactions, which are completely divorced from the electron-electron Coulomb interaction. Two such examples are hard-core and hollow-core interactions

$$V_{Hard-Core}: \quad \{V_0, V_1, V_2, \ldots\} = \{\infty, 1, 0, \ldots\} \tag{3.25}$$

$$V_{Hollow-Core}: \quad \{V_0, V_1, V_2, V_3, V_4, \ldots\} = \{0, 0, 0, 1, 0 \ldots\} \tag{3.26}$$

To obtain potential in terms of q, $V(q)[V_m]$, one can write [34]

$$\begin{aligned} V_m \equiv \langle \phi_m \,|\, \mathcal{V} \,|\, \phi_m \rangle &= \int \frac{d^2\mathbf{q}}{(2\pi)^2} V(q) \left\langle \phi_m \middle| e^{i\mathbf{q}\cdot\mathbf{r}} \middle| \phi_m \right\rangle \\ &= \int \frac{d^2\mathbf{q}}{(2\pi)^2} V(q) e^{-\ell^2 q^2} L_m\left(q^2\right) \end{aligned}$$

where ϕ_m are relative angular momenta eigenfunctions and L_m denotes Lagguere polynomials. Inversion of this expression yields the sought $V(q)[V_m]$ relation.

$$V(q) = 4\pi \sum_m V_m L_m\left(q^2\right)$$

3.2.1 SMA applied to $\nu = 1/3$ problems

The results provided in this section are obtained by numerical evaluation of $\Delta(k)$ (3.24) in Wolfram Mathematica software, where the integration is carried out using the Monte Carlo method.

Hard-core interaction and flat magnetoroton dispersion

Numerical calculations (notably here exact diagonalization) in the context of FQH systems often employ hard-core interaction (3.25), which for the predicted Laughlin ground state Ψ_L corresponds to the (trivially scaled) cropped Coulomb interaction V_1^{cr}, or even V_2^{cr} as for the fully polarized ground state is Ψ_L antisymmetric, which in turn means that no V_m with even m contribute.

Although the results may sufficiently capture many features of the many-body excitation spectrum, e.g. with the characteristic magnetoroton branch emerging from the excitation continuum above 3.4, there still remain discrepancies, caused either by the nature of the numerical approximation itself, limited sample size, its geometry, or by the used short-range interaction.

One such disparity is the consistently reproduced flat short-range behavior [36] $k \gg 1$.

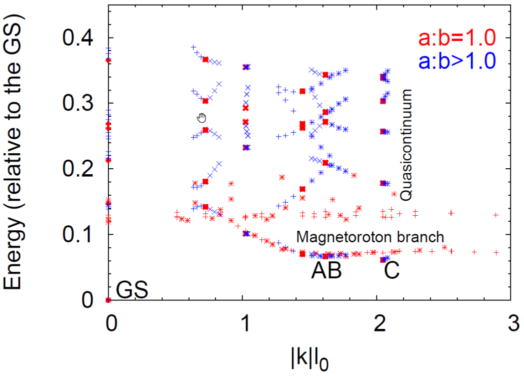

Figure 3.4: Results of exact diagonalization for 4-10 electrons with hard-core interaction in torus geometry. Source [37].

To resolve the question of the origin of this behavior, the Laughlin ground state and a series of potentials are examined using SMA. The resulting $\Delta(k)$ are presented in 3.5. For easier comparison are their energy scales (given either by various combinations of V_m or by e^2/ε_0 in the case of Coulomb interaction) assumed such that all $\Delta(k)$ have same $k \to 0$ limit.

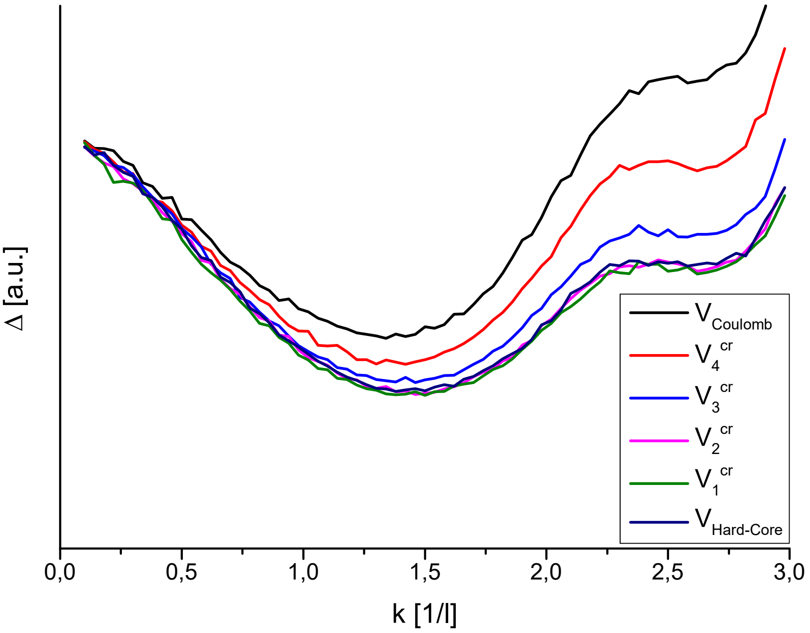

Figure 3.5: Energy gap $\Delta(k)$ dependence calculated using g_L radial distribution function and various interaction potential.

First, as expected, dispersions $\Delta(k)$ for V_1^{cr}, V_2^{cr} and $V_{Hard-Core}$ fully align as all these potentials are for the polarized ground state, disregarding scaling, the same.

Second, $\Delta(k)$ for potentials V_3^{cr}, V_4^{cr} and their comparison to full Coulomb $V_{Coulomb}$ shows that incorporating higher terms in V_k^{cr} progressively leads to bending the more flat dispersion upward as it approaches the full Coulomb interaction. Therefore, the potential choice has a significant effect on the $k \gg 1$ magnetoroton branch behavior and observed flat dispersion is at least in the main part caused by the chosen potential.

Non-Laughlin WYQ state thermodynamic limit

Wójs, Yi and Quin (WYQ) in a series of articles [38], [39] and [40] propose existence of a $\nu = 1/3$ liquid ground state with non-Laughlin correlations, emerging due to the condensation of quasi-electrons or quasi-holes with their interaction described via hollow-core potential (3.26). By means of exact diagonalization in sphere geometry, they argue that such a state is gapped.

Their conclusion is contended by Misguich, Jolicoeur and Mizusaki [41], who argue that their numerical results with limited number of electrons N_e do not necessarily lead to an incompressible state in the thermodynamic limit $N_e \to \infty$. Analysis of the $\Delta(N_e)$ behavior is conducted and is argued that in the thermodynamic limit the observed gap collapses.

Data from [41] are shown in 3.6: under the phenomenological assumption that the many-body energies scale linearly with $1/N_e$, as common in literature [42], [43] or [44], the extrapolated gap in an infinite system would be negative. Such phenomenology has, however, never been explained by fundamental arguments and should, therefore, be only accepted with due care.

SMA, which operates implicitly in the $N_e \to \infty$ limit, would be suitable to provide further evidence to this claim.

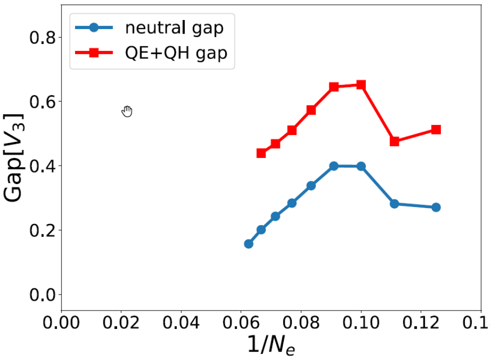

Figure 3.6: Exact diagonalisation $1/\Delta(N_e)$ dependence of WYQ state. Source [41]

Since the WYQ ground state is explicitly non-Laughlin, the RDF ansatz (3.11) cannot be used. Instead is introduced more general

$$g(r) = 1 - e^{-r^2/2\ell^2} + \sum_{m=1}^{\infty} c_m \left(\frac{r^2}{\ell^2}\right)^{2m} e^{-r^2/2\ell^2}, \tag{3.27}$$

and $g_{WYG-fit10}(r)$ is obtained by fitting first 10 nonzero coefficients c_m to exact diagonalisation RDF data provided in [41](Fig. 2). Table 3.1 contains values of fitted coefficients and the $g_{WYQ-fit10}$ itself is shown in 3.7

Although $g_{WYQ-fit10}$ matches the numerical data very well, its continuation to higher r with nontrivial structure proves to be problematic. As can be seen in figure 3.8, related projected structure factor $\bar{s}(k)$ (3.23) has zeros outside the limit $k \to 0$, which would lead to non-physical divergencies of $\Delta(k)$ (3.24).

Since SMA breaks in such a way for constructed RDF $g_{WYQ-fit10}$, calculation of the energy gap in this framework would require further work on the form of the g function and its long-range behavior. See Addendum for WYQ g-function and SMA.

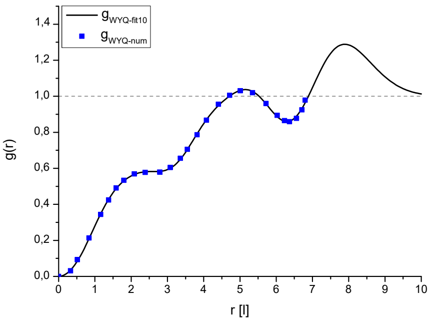

Figure 3.7: Exact diagonalisation RDF WYQ data (source [41]) and their fit $g_{WYQ-fit10}$ using first 10 coefficients.

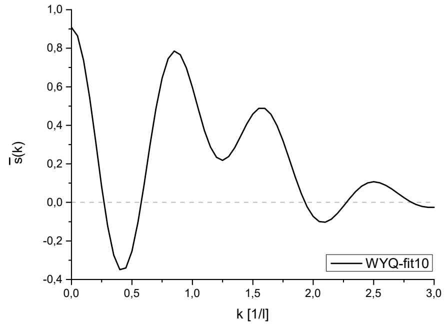

Figure 3.8: WYQ projected structure factor calculated using $g_{WYQ-fit10}$.

$c_m(g_{WYQ-fit10})$			
c_1	-0.169304	c_6	0.000242965
c_2	0.05772	c_7	-0.0000139233
c_3	-0.0462336	c_8	$4.54618.10^{-7}$
c_4	0.0140173	c_9	$-7.78369.10^{-9}$
c_5	-0.00244608	c_{10}	$5.35449.10^{-11}$

Table 3.1: $g_{WYQ-fit10}$ coefficients.

Conclusion

Within the vast field of Hall effect, three selected topics pertaining to non-magnetic materials were explored. In order of gradually increasing magnetic field it was: The ordinary Hall effect, integer quantum hall effect, and lastly fractional quantum hall effect. Each part of the work concerning different topic, was then dedicated to a selected problem with only a vague connection to the others.

Classical Hall effect

The temperature dependence of the semiclassical Hall coefficient was determined by means of the Sommerfeld expansion for the ideal electron gas and square lattice tight binding model.

Different single site approximations for description of substitutionally disordered materials were examined, and effects of introduced on-site disorder in square lattice model on the Hall coefficient were determined using coherent potential approximation.

Integer quantum Hall effect

The study of formation of Landau levels in the square lattice model with magnetic fields introduced via the Peierls substitution was conducted using the introduced descretization metric.

An approach to describe the effect of quantizing magnetic fields in realistic three-dimensional material is outlined.

Fractional quantum Hall effect

The single mode approximation is examined in detail and applied to two distinct problems concerning two-dimensional electron gas with filling factor $\nu = 1/3$.

The short range hollow core potential used in the exact diagonalization calculation of the excitation spectrum was identified as the main contributor to the flat large k dispersion of the magnetoroton branch. An attempt was made to apply single mode approximation to determine the excitation energy gap of the WYQ ground state.

Bibliography

[1] J. E. Avron, D. Osadchy, and R. Seiler. Topological quantum numbers in the hall effect, 2003.

[2] C. Hurd. *The Hall Effect in Metals and Alloys*. The International Cryogenics Monograph Series. Springer US, 2012.

[3] Naoto Nagaosa, Jairo Sinova, Shigeki Onoda, A. H. MacDonald, and N. P. Ong. Anomalous hall effect. *Rev. Mod. Phys.*, 82:1539–1592, May 2010.

[4] Jairo Sinova, Sergio O. Valenzuela, J. Wunderlich, C. H. Back, and T. Jungwirth. Spin hall effect. 2014.

[5] Philipp Ritzinger and Karel Vyborny. Anisotropic magnetoresistance: materials, models and applications, 2022.

[6] Georg Madsen and David Singh. Boltztrap. a code for calculating band-structure dependent quantities. *Computer Physics Communications*, 175:67–71, 07 2006.

[7] Slavomir Entler, Zbynek Soban, Ivan Duran, Karel Kovarik, Karel Vyborny, Josef Sebek, Stana Tazlaru, Jan Strelecek, and Petr Sladek. Ceramic-chromium hall sensors for environments with high temperatures and neutron radiation. *Sensors*, 21(3), 2021.

[8] A. Gonis. *Green Functions for Ordered and Disordered Systems*. Studies in mathematical physics. North-Holland, 1992.

[9] C. Albrecht, J. H. Smet, K. von Klitzing, D. Weiss, V. Umansky, and H. Schweizer. Evidence of hofstadter's fractal energy spectrum in the quantized hall conductance. *Phys. Rev. Lett.*, 86:147–150, Jan 2001.

[10] J. P. Eisenstein and H. L. Stormer. The fractional quantum hall effect. *Science*, 248(4962):1510–1516, 1990.

[11] Daijiro Yoshioka. Ground state of the two-dimensional charged particles in a strong magnetic field and the fractional quantum hall effect. *Phys. Rev. B*, 29:6833–6839, Jun 1984.

[12] J. K. Jain. Composite-fermion approach for the fractional quantum hall effect. *Phys. Rev. Lett.*, 63:199–202, Jul 1989.

[13] R. B. Laughlin. Anomalous quantum hall effect: An incompressible quantum fluid with fractionally charged excitations. *Phys. Rev. Lett.*, 50:1395–1398, May 1983.

[14] S. M. Girvin. Anomalous quantum hall effect and two-dimensional classical plasmas: Analytic approximations for correlation functions and ground-state energies. *Phys. Rev. B*, 30:558–560, Jul 1984.

[15] M. Battiato, V. Zlatic, and K. Held. Boltzmann approach to high-order transport: The nonlinear and nonlocal responses. *Physical Review B*, 95(23), jun 2017.

[16] Werner W. Schulz, Philip B. Allen, and Nandini Trivedi. Hall coefficient of cubic metals. *Phys. Rev. B*, 45:10886–10890, May 1992.

[17] Thoralf Hanisch, Götz S. Uhrig, and Erwin Müller-Hartmann. Lattice dependence of saturated ferromagnetism in the hubbard model. *Physical Review B*, 56(21):13960–13982, dec 1997.

[18] Pavel Středa and Jan Kučera. Orbital momentum and topological phase transformation. *Phys. Rev. B*, 92:235152, Dec 2015.

[19] B. Velický. Theory of electronic transport in disordered binary alloys: Coherent-potential approximation. *Phys. Rev.*, 184:614–627, Aug 1969.

[20] N. W. Ashcroft and N. D. Mermin. *Solid State Physics.* Holt-Saunders, 1976.

[21] G. D. Mahan. *Many Particle Physics, Third Edition.* Plenum, New York, 2000.

[22] V. I. Kukulin, V. M. Krasnopolsky, and Jiří Horáček. Theory of resonances: Principles and applications. 2010.

[23] K. Levin, B. Velický, and H. Ehrenreich. Electronic transport in alloys: Coherent-potential approximation. *Phys. Rev. B*, 2:1771–1788, Sep 1970.

[24] S. Entler, J. Sebek, I. Duran, K. Vyborny, O. Grover, M. Kocan, and G. Vayakis. High magnetic field test of the ITER outer vessel steady-state magnetic field Hall sensors at ITER relevant temperature. *Review of Scientific Instruments*, 89(10), 08 2018. 10J112.

[25] Irene Aguilera, Christoph Friedrich, and Stefan Blügel. Electronic phase transitions of bismuth under strain from relativistic self-consistent *gw* calculations. *Phys. Rev. B*, 91:125129, Mar 2015.

[26] Richard Phillips. Feynman and Jacob. Shaham. *Statistical mechanics : a set of lectures / R.P. Feynman ; notes taken by R. Kikuchi and H.A. Feiveson, edited by Jacob Shaham.* W.A. Benjamin Reading, Mass, 1972.

[27] S. M. Girvin, A. H. MacDonald, and P. M. Platzman. Magneto-roton theory of collective excitations in the fractional quantum hall effect. *Phys. Rev. B*, 33:2481–2494, Feb 1986.

[28] Sanwu Wang. Generalization of the thomas-reiche-kuhn and the bethe sum rules. *Phys. Rev. A*, 60:262–266, Jul 1999.

[29] Tapash Chakraborty and Pekka Pietiläinen. The quantum hall effects: Integral and fractional. 1995.

[30] Jean-Pierre Hansen and Ian R. McDonald. Chapter 3 - static properties of liquids: Thermodynamics and structure. In Jean-Pierre Hansen and Ian R. McDonald, editors, *Theory of Simple Liquids (Third Edition)*, pages 46–77. Academic Press, Burlington, third edition edition, 2006.

[31] B. Jancovici. Exact results for the two-dimensional one-component plasma. *Phys. Rev. Lett.*, 46:386–388, Feb 1981.

[32] Harry Bateman. Tables of integral transforms [volumes i & ii]. 1954.

[33] Walter Kohn. Cyclotron resonance and de haas-van alphen oscillations of an interacting electron gas. *Phys. Rev.*, 123:1242–1244, Aug 1961.

[34] A. H. MacDonald. Introduction to the physics of the quantum hall regime, 1994.

[35] S. M. Girvin and Terrence Jach. Formalism for the quantum hall effect: Hilbert space of analytic functions. *Phys. Rev. B*, 29:5617–5625, May 1984.

[36] Thierry Jolicoeur. Shape of the magnetoroton at $\nu = 1/3$ and $\nu = 7/3$ in real samples. *Phys. Rev. B*, 95:075201, Feb 2017.

[37] K. Výborný. *Spin in fractional quantum Hall systems*. PhD thesis, niversität Hamburg, 2005.

[38] Arkadiusz Wójs, Kyung-Soo Yi, and John J. Quinn. Fractional quantum hall states of clustered composite fermions. *Phys. Rev. B*, 69:205322, May 2004.

[39] Arkadiusz Wójs, Daniel Wodziński, and John J. Quinn. Pair-distribution functions of correlated composite fermions. *Phys. Rev. B*, 71:245331, Jun 2005.

[40] John J. Quinn, Arkadiusz Wójs, Kyung-Soo Yi, and George Simion. The hierarchy of incompressible fractional quantum hall states. *Physics Reports*, 481(3):29–81, 2009.

[41] Grégoire Misguich, Thierry Jolicoeur, and Takahiro Mizusaki. Bubble phase at $\nu = 1/3$ for spinless hollow-core interaction. *Physical Review B*, 102(24), dec 2020.

[42] K. Niemelä, P. Pietiläinen, and T. Chakraborty. Spin transitions in the fractional quantum hall systems. *Physica B: Condensed Matter*, 284-288:1716–1717, 2000.

[43] R. H. Morf, N. d'Ambrumenil, and S. Das Sarma. Excitation gaps in fractional quantum hall states: An exact diagonalization study. *Phys. Rev. B*, 66:075408, Aug 2002.

[44] Annelene F. Dethlefsen, Rolf J. Haug, Karel Výborný, Ond řej Čertík, and Arkadiusz Wójs. Transport gap in a $\nu = 1/3$ quantum hall system: A probe for skyrmions. *Phys. Rev. B*, 74:195324, Nov 2006.

[45] Steven M. Girvin. *Introduction to the Fractional Quantum Hall Effect*, pages 133–162. Birkhäuser Basel, Basel, 2005.

List of Figures

A. Appendices

A.1 Numerical calculation of 1D chain DOS

Negative eigenvalue counting algorithm [8] is used to obtain the DOS of the 1D chain numerically. Let $\mathbf{H} \in \mathbb{C}^{n\times n}$ be a complex matrix site representation of Hamiltonian (1.25), $\mathbf{I}$ unit matrix and define new matrix

$$\mathbf{A}(z) \equiv \mathbf{H} - z\mathbf{I}.$$

The spectrum $\sigma(\mathbf{A})$ of matrix $\mathbf{A}$ is for given z only the spectrum $\sigma(\mathbf{H})$ shifted by z. Therefore, the total number of negative eigenvalues of $\mathbf{A}$ is equal to the total number of energy eigenstates with energy less than z. Or, yet in other words, it is equal to the cumulative density of states $N(z)$.

Sylvester's law of inertia can be utilised for symmetric forms as $N(z)$ is precisely negative index of inertia in $\mathbf{A}$s signature. Denoting $a_0 = 1$ and a_k $k \times k$ principal upper left minor of $\mathbf{A}$ (determinant of $k \times k$ upper left submatrix), $N(z)$ is equal to the number of sign changes in sequence $a_0, a_1, a_2, \ldots$.

In particular in the 1D chain case, $\mathbf{H}$ is a tridiagonal matrix with stochastic main diagonal consisting of terms ε_k and both lower and upper diagonals filled with constant hopping parameters t. Direct expansion of determinant of associated matrix $\mathbf{A}(z)$ shows

$$a_k = (\varepsilon_k - z)\, a_{k-1} - t^2 a_{k-2} \quad \Longrightarrow \quad \frac{a_k}{a_{k-1}} = \varepsilon_k - z - t^2 \frac{a_{k-2}}{a_{k-1}}$$

and this formula is further simplified by introduction of $h_i = a_i/a_{i-1}$. Denoting θ Heaviside step function then allows to summarize this algorithm as

$$N(z) = \sum_{i=1}^{n} \theta(-h_i), \qquad \text{with} \qquad h_1 = \varepsilon_1 - z, \quad h_k = \varepsilon_k - z - t^2 h_{k-1}^{-1}.$$

Since the original Hamiltonian matrix $\mathbf{H} \in \mathbb{C}^{n\times n}$ does not appear in this algorithm, one can choose to simply continue this iteration indefinitely. This can be used to obtain the configuration average instead of generating multiple replicas of the same system. The comparison of convergence of these two approaches is presented in the following two figures A.1 and A.2, where the resulting DOS are shown for two different values of defining parameters c, δ and for different sizes of the system and for one large system as opposed to many smaller replicas.

Note that the chosen method calculates the cumulative density of states for each energy point again (with a new generated distribution of site types), which may result in a negative DOS. This behaviour becomes negligible with a large enough system (or total number of sites counted) as the algorithm converges to the right physical values. Alternatively, one has to perform this algorithm for every energy point simultaneously using same sequence of potentials ϵ_k.

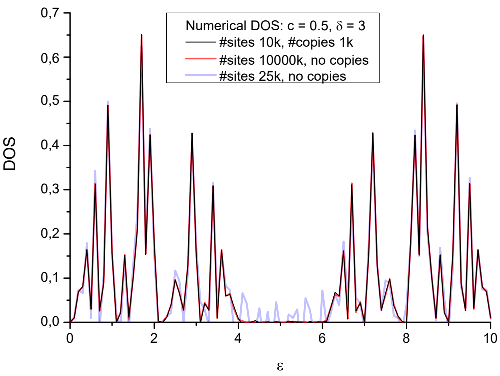

Figure A.1: Numerical g_{1D}^{cb} results, $c = 0.5$, $\delta = 3$.

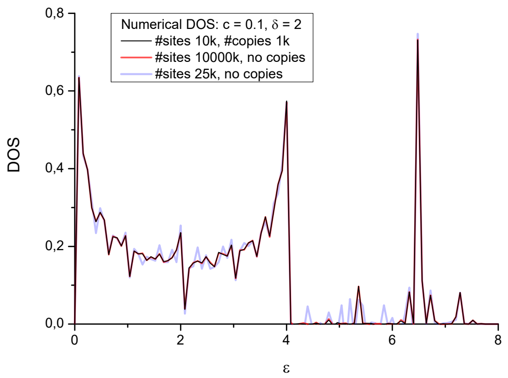

Figure A.2: Numerical g_{1D}^{cb} results, $c = 0.1$, $\delta = 2$.

A.2 Single site approximations

ATA derivation

Denote P_0 diagonal part of propagator P, and $P' = P - P_0$ off-diagonal. Define the single side t-matrix t as a sum of all repeated scattering processes on the same site.

$$t = \mathcal{V} + \mathcal{V} P_0 \mathcal{V} + \mathcal{V} P_0 \mathcal{V} P_0 \mathcal{V} + \dots$$

Since it is by its construction single site dependent, its configurational average is given by sum of two contributions, one corresponding to contribution of site A, with energy ε_A, and second to site B, with ε_B.

$$\langle t \rangle = (1-c)\frac{\varepsilon_A}{1 - P_0 \varepsilon_A} + c\frac{\varepsilon_B}{1 - P_0 \varepsilon_B}$$

Full T-matrix $\mathcal{T}$ is then

$$\mathcal{T} = \mathcal{V} + \mathcal{V} P \mathcal{V} + \mathcal{V} P \mathcal{V} P \mathcal{V} + \dots = t + tP't + tP'tP't + \dots .$$

Note the use of the off diagonal P', which prevents immediate return to the same site, as that contribution is already included in t. Of interest is only configurational average of T-matrix

$$\langle \mathcal{T} \rangle = \langle t \rangle + \langle tP't \rangle + \langle tP'tP't \rangle \dots ,$$

which is the most problematic part. The derivation is so far exact, but there is no easy way to correctly account for all correlations in $\langle \dots \rangle$. A simple decoupling scheme $\langle tP' \dots t \rangle = \langle t \rangle P' \dots \langle t \rangle$ is chosen, so all processes without returns are correctly accounted for in this approximation. I.e. in the $\mathcal{T}$ series, the first two terms would be treated correctly and from the third term up the correlation of returning particles would be neglected.

Now the T-matrix series can be summed

$$\langle \mathcal{T} \rangle = \langle t \rangle \left(1 - P' \langle t \rangle\right)^{-1}$$

and substituting it into $\langle \mathcal{T} \rangle (\Sigma)$ equation (1.38) and using $P - P' = P_0$ then leads to final Σ_{ATA} expression, with $\langle t \rangle$ given above.

$$\Sigma_{ATA} = \frac{\langle t \rangle}{1 + \langle t \rangle P_0}.$$

SCBA derivation

Born approximation consists of taking only first two terms in self-energy expansion series (1.39).

$$\Sigma_{BA} = \langle \mathcal{V} \rangle + \langle \mathcal{V} P \mathcal{V} \rangle + \dots$$

Assuming VCA medium the first term vanishes as $\langle \mathcal{V} \rangle = 0$. Sigma is here necessarily scalar as the off-diagonal part would indicate that the present on-site potentials would belong to different sites and consequently the term would also vanish in configurational average. Since they are related to the same site, the average gives

$$\Sigma_{BA} = \langle \mathcal{V} P \mathcal{V} \rangle = (1-c)\varepsilon_A^2 P_0 + c\varepsilon_B^2 P_0 = c(1-c)\Delta_\varepsilon^2 P_0,$$

where the last equality is written using VCA on site potentials (1.40).

This approximation is clearly rather weak as it is correctly accounting for only simple (once repeated) scattering on the same site, without any returns or more complicated processes. Vast improvement then provides its self-consistent variant (SCBA), which assumes that the propagation in self-energy expression is through the effective medium itself, replacing $P \to \overline{G}$.

In mathematical sense, this substitution significantly broadens the set of scattering processes included in the self-energy, improving the accuracy of the approximation.

$$\Sigma_{SCBA} = c(1-c)\Delta_\varepsilon^2 \overline{G}_{00}$$

CPA derivation

Assuming known effective medium Σ full GF G can be written as a series expansion with respect to effective GF $\overline{G}$ as

$$G = \overline{G} + \overline{G}(\mathcal{V} - \Sigma)\overline{G} + \dots = \overline{G} + \overline{G}\mathcal{T}\overline{G}.$$

Since by its definition is GF and its effective variant related via configurational average

$$\langle G \rangle = \overline{G}, \quad \langle G \rangle = \overline{G} + \overline{G}\,\langle \mathcal{T} \rangle\,\overline{G} \quad \longrightarrow \quad \langle \mathcal{T} \rangle = 0,$$

effective medium Σ should be now such that in average all scattering effects cancel each other out.

Following formalism used in **??**, namely $\overline{G}'$ to denote off diagonal part, $\overline{G}_{00} = \overline{G} - \overline{G}'$ and t single site scattering t-matrix, which is in current context of the form

$$t = \left(1 - (\mathcal{V} - \Sigma)P_0\right)^{-1}(\mathcal{V} - \Sigma),$$

leads to concise expression

$$\mathcal{T} = (\mathcal{V} - \Sigma)\left(1 + \overline{G}\mathcal{T}\right) = t\left(1 + \overline{G}'\mathcal{T}\right).$$

Again, the second equality corresponds to different summation, now counting all repeated scattering events on same site in t and continuing expansion with explicitly forbidden immediate returns via $\overline{G}'$.

In configurational average is

$$\langle \mathcal{T} \rangle = 0 = \left\langle t \left(1 + \overline{G}'\mathcal{T}\right)\right\rangle = \langle t \rangle + \left\langle t\overline{G}'\mathcal{T}\right\rangle .$$

So far were all expression exact and at this point comes into play the CPA decoupling scheme, where is assumed

$$\left\langle t\overline{G}'\mathcal{T}\right\rangle = \langle t \rangle \, \overline{G}' \, \langle \mathcal{T} \rangle = 0.$$

This corresponds to neglect of the correlation of the 'main' on site scattering t, which is treated exactly, and all other contributions of the surrounding effective medium governed by the $\overline{G}'\mathcal{T}$ term. This interpretation can be seen from the following. Since t is diagonal, for each given site i does the surrounding medium contribution

$$t\overline{G}'\mathcal{T} \quad \longrightarrow \quad t_i \sum_{j \neq i} \overline{G}'_{ij} \mathcal{T}_{ji}$$

span all scattering processes starting at site i, ending at j and then returns back to i.

CPA self-energy condition then simplifies to

$$\langle t \rangle = 0 = (1 - c)\frac{\varepsilon_A - \Sigma}{1 - (\varepsilon_A - \Sigma)\overline{G}_{00}} + c\frac{\varepsilon_B - \Sigma}{1 - (\varepsilon_B - \Sigma)\overline{G}_{00}},$$

which (taking into account VCA medium $\langle \mathcal{V} \rangle = 0$) yields

$$\Sigma_{CPA} = -\left(\varepsilon_A - \Sigma_{CPA}\right)\overline{G}_{00}\left(\varepsilon_B - \Sigma_{CPA}\right).$$

A.3 Planar 1-body problem in magnetic field

Hamiltonian corresponding to a planar problem $\{x, y\}$ of particle in external out of plane magnetic field ($\mathbf{B} = -B\mathbf{e}_z$) is in the symmetric gauge of the form

$$\mathcal{H}_1 = \frac{1}{2m}\pi^2 = \frac{1}{2m}\left(\mathbf{p} - e\mathbf{A}\right)^2, \mathbf{A} = \frac{B}{2}\left(y; -x\right)^T,$$

where $\mathbf{A}$ stands for vector potential. π denotes vector kinetic momentum, and $\mathbf{p}$ canonical momentum operators.

The radial coordinates $\{r, \phi\}$ are due to the chosen gauge more suitable for the description of the problem at hand. Introducing angular momentum operator $L_z = -i\hbar\partial_\phi$ leads to

$$\mathcal{H}_1 = \frac{1}{2m}\left[-\hbar^2\frac{1}{r}\partial_r\left(r\partial_r\right) + \frac{L_z^2}{r^2} + \frac{e^2B^2}{4}r^2 - eBL_z\right].$$

Since $[\mathcal{H}_1, L_z] = 0$, the eigenstates $\phi_{n,m}$ of $\mathcal{H}_1$ are determined by two separate quantum numbers: n corresponding to the energy or Landau level (LL) and m to angular momentum.

The complete solution of the problem is elegantly captured using the ladder operator algebra presented in full in [34] with its derivation and motivation. In the following are provided only final expressions adapted to current formalism (note assumed opposite orientation of external magnetic field) and bare bone hints of their derivation.

First, introducing energy-level ladder operators

$$a^\dagger \equiv \frac{\ell/\hbar}{\sqrt{2}}\left(\pi_x + i\pi_y\right), \quad [a^\dagger, a] = 1,$$

with $\ell = \sqrt{\hbar/eB}$ magnetic length, leads to harmonic oscillator Hamiltonian with cyclotron frequency $\omega_c = eB/m$

$$\mathcal{H}_1 = \hbar\omega_c\left(a^\dagger a + \frac{1}{2}\right) \quad \text{and energy} \quad \varepsilon_n = \hbar\omega_c\left(n + \frac{1}{2}\right).$$

The second set of ladder operators $b^\dagger$ and b corresponding to angular momentum quantization have to fulfill

$$[b^\dagger, b] = 1, \quad [b^\dagger, \mathcal{H}_1] = [b, \mathcal{H}_1] = 0$$

and all ladder operators from different sets have to commute.

Defining expression for $a^\dagger$ hints at the usefulness of complex notation of 2D vectors. Notably for the position is

$$\mathbf{r} = (x, y) \to z = x + iy.$$

and using such notation allows one to write all ladder operators in a symmetric form

$$\begin{aligned} b^\dagger &= \frac{1}{\sqrt{2}}\left(\frac{z}{2\ell} - 2\ell\frac{\partial}{\partial\bar{z}}\right), \quad b = \frac{1}{\sqrt{2}}\left(\frac{\bar{z}}{2\ell} + 2\ell\frac{\partial}{\partial z}\right) \\ a^\dagger &= \frac{1}{\sqrt{2}}\left(\frac{\bar{z}}{2\ell} - 2\ell\frac{\partial}{\partial z}\right), \quad a = \frac{1}{\sqrt{2}}\left(\frac{z}{2\ell} + 2\ell\frac{\partial}{\partial\bar{z}}\right). \end{aligned}$$

All $\mathcal{H}_1$ eigenstates can be then written in the form

$$|\phi_{n,m}\rangle = \frac{\left(a^\dagger\right)^n\left(b^\dagger\right)^m}{\sqrt{n!m!}}|\phi_{0,0}\rangle, \quad \phi_{0,0} = \frac{1}{\sqrt{2\pi\ell^2}}e^{-z\bar{z}/4\ell^2}.$$

Especially in the LLL

$$\phi_{0,m} = \frac{z^m e^{-z\bar{z}/4\ell^2}}{\sqrt{2\pi\ell^2 2^m m!}}$$

is the polynomial part of the eigenfunction reduced to a monomial with the power equal to the quantum number m. The orthogonality of the eigenfunctions is within the LLL same as the orthogonality of monomials of different power. Also, all LLL wavefunctions consist of Gaussian term and prefactor analytical in z.

The eigenfunction $\phi_{0,m}$ is localized in the vicinity of the ring $r = \sqrt{2m\ell^2}$, where its probability amplitude peaks and then falls sharply. In the ring of the radius R are thus enclosed $2\pi\ell^2 m$ eigenfunctions. This means that the degeneracy of the LL increases proportionally with the increasing magnetic field B.

A.4 Lowest Landau level polarized 2DEG

The many-body wavefunction can be constructed from the 1-particle wavefunction. In the LLL, they can be written in the form

$$\Psi(z_1, z_2, \dots z_N) \propto P[z_1, z_2, \dots z_N] e^{-\frac{1}{4\ell^2}\sum_i z_i \bar{z}_i}$$

consisting of common exponential term and general polynomial prefactor P (or generally infinite series f), which is analytical function of its variables. Assuming complete polarization P has to be antisymmetric.

The most simple case is that of fully filled LLL (filling factor $\nu = 1$), where any interaction would lead only to a shift of energy and leaves the wavefunction unchanged. In such case is the exact wavefunction constructed as antisymmetrisation of all 1-particle eigenfunctions $\phi_{0,m}$, $m \in \{1, 2, \dots\}$

$$\Psi_{\nu=1} \propto \begin{vmatrix} z_1^0 & z_1^1 & \dots \\ z_2^0 & z_2^1 & \dots \\ \vdots & \vdots & \ddots \end{vmatrix} e^{-\frac{1}{4\ell^2}\sum_i z_i \bar{z}_i} = \prod_{i<j}(z_i - z_j) e^{-\frac{1}{4\ell^2}\sum_i z_i \bar{z}_i}$$

and the polynomial prefactor is in this case a Vandermonde determinant.

When $\nu < 1$ one has to take into account interparticle interaction V. Starting with 2-body problem, wavefunctions are of the form (disregarding common exponential term)

$$\Psi_2(z_1, z_2) \propto P(z_1, z_2).$$

It is natural to employ center of mass (CMS) coordinates

$$z_r = z_1 - z_2, \quad Z = \frac{z_1 + z_2}{2}$$

and view Ψ_2 as constructed using CMS and relative motion eigenfunctions ϕ^c_M, ϕ^r_m with their angular momenta quantum numbers M and m. Their form is clear from the following:

2-body Hamiltonian

$$\mathcal{H}_2 = \frac{1}{2m}\pi_1^2 + \frac{1}{2m}\pi_2^2$$

can be expressed in CMS coordinates as

$$\mathcal{H}_2 = \frac{\Pi_c^2}{2M_c} + \frac{\pi^2}{2\mu}, \qquad \text{with} \qquad M_c = 2m, \quad \mu = \frac{1}{2}m$$

with

$$\Pi_c^2 = (\pi_1 + \pi_2)^2 = (\mathbf{p}_1 + \mathbf{p}_2 - e(\mathbf{A}_1 + \mathbf{A}_2))^2 = (\mathbf{P}_c - 2e\mathbf{A}_c)^2$$
$$\pi^2 = \left(\frac{\pi_1 - \pi_2}{2}\right)^2 = \left(\frac{\mathbf{p}_1 - \mathbf{p}_2}{2} - \frac{e(\mathbf{A}_1 - \mathbf{A}_2)}{2}\right)^2 = \left(\mathbf{p} - \frac{e}{2}\mathbf{A}\right)^2.$$

CMS and relative motion variables are fully separated allowing to write eigenfunction in the form

$$\Psi_{Mm} = \phi^c_M \phi^r_m,$$

with known 1-body eigenfunctions ϕ^c_M, with magnetic length $\ell_c = \ell/\sqrt{2}$, and ϕ^r_m, with $\ell_r = \ell\sqrt{2}$. The cyclon frequency in both cases remains unchanged.

Of interest is mainly the relative motion part of the wavefunction ϕ^r_m since the interparticle interaction does not couple to the CMS DOF.

Expressing the 2-body interaction $\mathcal{V}$ in $\{\,\Psi_{Mm}\,\}^{\infty}_{M,m=0}$ basis leads to the definition of the so-called Haldane pseudopotentials $V_{mm'}$. Additionally, interaction given by the potential independent of relative angular coordinate (i.e. purely radial) leads to owing to the orthogonality relations of $\{\,z^m\,\}^{\infty}_{m=0}$ non-zero only diagonal terms of its matrix representation $V_{m'm}$.

$$V_m = \langle \Psi_{Mm} \,|\, \mathcal{V} \,|\, \Psi_{M'm'} \rangle \, \delta_{MM'} \delta_{mm'}$$

Interaction are thus fully given by a set of pseudopotentials $\{V_m\}^{\infty}_{m=0}$, where in the present case of fully polarised system contribute only terms with odd m due to the antisymmetry of the polynomial part $P(z_1, z_2, \ldots)$ of the wavefunctions.

Specially for Coulomb interaction $V(r) = ke^2/r$ is in CMS coordinates

$$V_m = \langle \Psi_{Mm} \,|\, V \,|\, \Psi_{Mm} \rangle = \frac{e^2 k}{2\ell^{2(m+1)} 4^m m!} \int r^{2m} e^{-\frac{r^2}{4\ell^2}} dr.$$

For integrals of this form is

$$\int dx x^n e^{-ax^b} = \frac{\Gamma\left(\frac{n+1}{b}\right)}{b a^{\frac{n+1}{b}}}, \qquad \text{where } a = \frac{1}{4\ell^2} \quad b = 2,$$

yielding

$$V_m = \frac{e^2 k}{\ell^{2(m+1)} 4^m m!} \frac{1}{4} \Gamma\left(m + \frac{1}{2}\right) \left(4\ell^2\right)^{m+\frac{1}{2}} = \frac{ke^2}{2\ell} \frac{\Gamma\left(m + \frac{1}{2}\right)}{\Gamma\left(m+1\right)}.$$

As can be seen in figure A.3 in LLL Coulomb V_m monotonically decreases with m and asymptotically is $V_m \approx m^{-1/2}$.

The pseudopotential representation is also suitable for the definition of new interaction potentials. For example, since the relative angular momentum quantum number m corresponds to a relative distance [45], V_m are suitable for the definition of short-range interaction potentials.

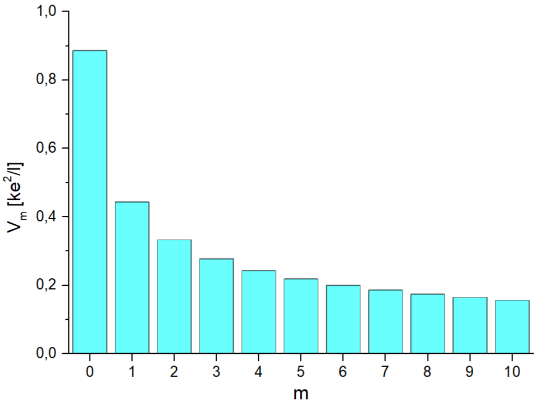

Figure A.3: Haldane pseudopotential representation of LLL Coulomb interaction potential.

Of particular interest is the Hard-core interaction

$$V_{Hard-Core}: \quad \{V_0, V_1, V_2, \ldots\} = \{\infty, 1, 0, \ldots\}.$$

With such a potential, only terms with relative angular momentum $m = 1$ contribute to energy, and it is easy to construct the exact many-body ground state wave function corresponding to the filling factor $\nu = 1/3$.

$$\Psi_L \propto \prod_{i<j}(z_i - z_j)^3 e^{-\frac{1}{4\ell^2}\sum_i z_i \bar{z}_i}$$

Φ_L is $\nu = 1/3$ realization of wider ansatz, the so called Laughlin wavefunction [29].

A.5 Addendum for WYQ g-function and SMA

Straightforward application of the SMA energy gap function (3.24) in section Non-Laughlin WYQ state thermodynamic limit, shown in figure A.4, clearly reveals the problems of the RDF used $g_{WYQ-fit10}$ 3.7. There are not only expected divergences present due to the zeros of the projected structure factor 3.8, but also a negative gap $\Delta(k)$ going against the very assumption that $g_{WYQ-fit10}$ describes a ground state.

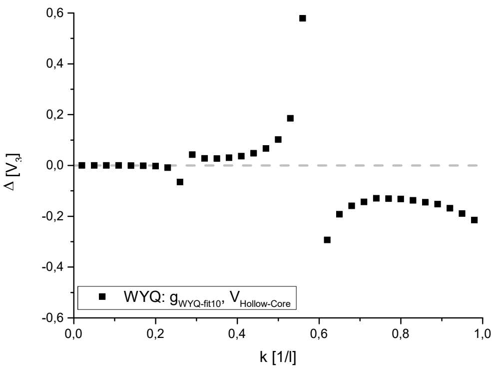

Figure A.4: $\Delta(k)$ dependence calculated using $g_{WYQ-fit10}$ RDF and hollow core interaction potential.

Another g-function $g_{WYQ-fit5}$, with only five nonzero coefficients A.1 of the expansion (3.27) was fitted to the numerical data. As can be seen in A.5, $g_{WYQ-fit5}$ is again a good fitting function for most of the data, but the few very last points.

As is common in general for the small system numerical calculations, obtained long-range results may not reflect realistic macroscopic systems as well as short-range ones. In this sense, less emphasis on them in $g_{WYQ-fit5}$ may even prove beneficial, as it allows elimination of the additional structure present in 3.7.

The related projected static structure factor A.6 now paints a very different picture than that of $g_{WYQ-fit10}$, figure 3.7. Elimination of $g_{WYQ-fit10}$ long-range correlations drastically alters structure factor dependence for small k, removing one of the two problematic zeros.

$c_m(g_{WYQ-5})$	
c_1	-0.141474
c_3	-0.00427787
c_5	0.000010427
c_7	$6.02757.10^{-9}$
c_9	$-1.53175.10^{-11}$

Table A.1: $g_{WYQ-fit5}$ coefficients, for even m $c_m = 0$.

Although $g_{WYQ-fit5}$ could still not be used for a meaningful application of the SMA to the problem, it reveals that the core of the issue lies in the long-range behavior of the assumed g-function, for which no data are currently available.

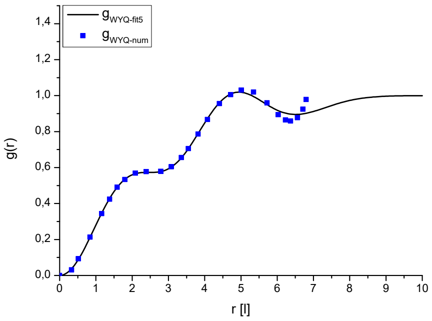

Figure A.5: Exact diagonalization RDF WYQ data (source [41]) and their fit $g_{WYQ-fit5}$ using the first five odd coefficients.

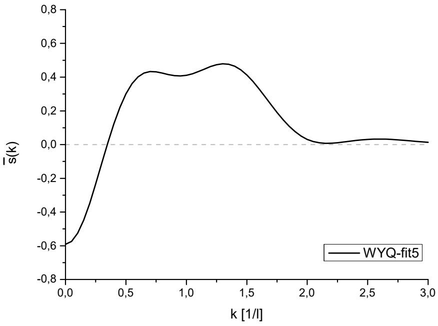

Figure A.6: WYQ projected structure factor calculated using $g_{WYQ-fit5}$.